

Switchability Induced by Mechanical Instability in Bioinspired Adhesives

Dissertation

zur Erlangung des Grades

des Doktors der Naturwissenschaften

der Naturwissenschaftlich-Technischen Fakultät III

Chemie, Pharmazie, Bio- und Werkstoffwissenschaften

der Universität des Saarlandes

von

Dadhichi R. Paretkar

Angefertigt am INM - Leibniz-Institut für Neue Materialien

Programmbereich Funktionelle Oberflächen

Universität des Saarlandes

Saarbrücken

März 2012

Tag des Kolloquiums: 13.07.2012
Dekan: Prof. Dr. W. F. Maier
Vorsitzender: Prof. Dr. G. Wenz
Berichterstatter: Prof. Dr. E. Arzt
Prof. Dr. W. Possart
Akad. Beisitzer: Dr.-Ing. F. Aubertin



*This work is dedicated to my mother,
who instilled in me an urge to learn.
And to my father, who supported it;
quoting at times from
H. W. Longfellow's 'A Psalm of Life',*

"Lives of great men all remind us
We can make our lives sublime,
And, departing, leave behind us
Footprints on the sands of time;"

Abstract

Non-covalent adhesion produced by the gecko is attributed to the structured surface of its toes. The synthetic adhesives mimicking this principle have now been around for a decade. However, the characteristic features of reversibility and self-cleaning ability of the gecko adhesive system have not yet been successfully integrated. The present work focuses on developing a switchable adhesive system responsive to an external stimulus. Elastomeric polydimethylsiloxane surfaces are structured with fibrillar arrays. Mechanical instability of the fibrils is recognized and utilized to produce a reversible switch between adhesion and non-adhesion. Normal compression caused the fibrils to buckle inducing a contact transition from their tips to the sides. When the contact transition occurred under moderate compressive loads, tip contact re-formed upon reversal of buckling and adhesion was reversible. However, when reversible buckling occurred under large compressive loads or when fibril side peeled without unbuckling, contact re-formation was impaired. Drastic change in contact area in the re-formed state resulted in a low adhesion state. The role of fibril contact shape, radius, aspect ratio, orientation and the applied compressive load in the adhesion switchability was examined. *In situ* visualization was employed to study the contact mechanisms. Contact shape, fibril orientation and preload were identified as the key parameters for controlling switchable adhesion.

Zusammenfassung

Die nicht-kovalente Adhäsion von Geckos beruht auf der Oberflächenstruktur ihrer Zehen. Während der letzten zehn Jahre wurden künstliche Haftsysteme hergestellt, die auf diesem Prinzip beruhen. Die charakteristischen Eigenschaften des Gecko-Haftsystems, Reversibilität und Selbstreinigung, konnten jedoch bisher nicht integriert werden. Ziel dieser Arbeit ist die Entwicklung und Untersuchung eines reversiblen Haftsystems, das durch einen externen Stimulus geschaltet werden kann. Dazu wurden fibilläre Oberflächen aus Polydimethylsiloxan hergestellt. Die mechanische Instabilität der Fibrillen wurde zur reversiblen Schaltung zwischen haftendem und nicht-haftendem Zustand verwendet. Senkrechter Druck auf die Fibrillen führte zu Knickung, wobei ein Übergang von Spitzen- zu Seiten-Kontakt der Strukturen beobachtet wurde. Bei moderatem Druck konnte sich nach Entlasten und dem Wiederaufrichten der Fibrillen der Spitzen-Kontakt wiederherstellen, was zu hoher Adhäsion führte. Bei starkem Druck wurde der Spitzenkontakt nach der Knickung nicht wieder hergestellt. Die starke Änderung der Kontaktfläche führte dann zu einer niedrigen Adhäsion. Der Einfluss von Druck, Kontaktform, Radius und Aspektverhältnis sowie Ausrichtung der Fibrillen auf die Schaltbarkeit der Adhäsion wurde untersucht. Die Kontaktbildungsmechanismen wurden mittels *in situ* Visualisierung beobachtet. Kontaktform, Fibrillenausrichtung und Druck wurden als Schlüsselparameter zur Kontrolle der schaltbaren Adhäsion identifiziert.

Acknowledgment

The following research work was carried out from January 2009 to December 2011 at the INM-Leibniz Institute for New Materials, Saarbrücken.

Looking at these past three years in the Functional Surfaces Group of Prof. Eduard Arzt makes me realize the immense enrichment, which the opportunity to work as his doctoral student provided me. I am deeply indebted to him for giving me a smart research topic, providing an excellent support team and research tools, extending insightful guidance when sought, opening doors to the best research groups in the field and above all being supportive of my aspirations by challenging my own limits. For a good reason apparently, the German speaking community uses the term *Doktorvater* for a thesis advisor.

The freedom to ask questions and debate on sticky issues encountered in routine research was granted to me by Dr. Marleen Kamperman, who supervised major part of the work. I am grateful to her for her patient and persistent approach to problem solving; right from understanding fundamentals, to overcoming experimental hurdles, to fine tuning the art of presenting research.

Joachim Blau has greatly helped in this work by being there for me every time I was challenged with technical issues related to my experiments. I wish to sincerely acknowledge his help and that of the INM Mechanical Workshop on test devices and tools used in the course of this work. Additionally, I thank him for extending his photography and video shooting expertise to further this work.

Prof. Robert McMeeking offered a smooth slide into the intricate world of the contact mechanics of adhesion. I am thankful to him for being patient with me through the long, insightful discussions on experimental results.

Dr. Andreas S. Schneider motivated me with new ideas that helped further the work with *adhesion testing* at the Environmental Scanning Electron Microscope and on the temperature controlled shape memory polymers. I am thankful to him for many useful discussions.

Dr. Elmar Kroner introduced me to his adhesion test apparatus used in this work. I wish to thank him for being approachable on issues related to adhesion testing and his active participation in group discussions.

Prof. Wulff Possart's course on *Adhesives and Adhesion Technology* was very helpful to guide me into the new topic. He is the scientific co-advisor for this work and has provided timely insights on my research during our regular progress meetings. Most sincere thanks to him.

I wish to greatly thank Prof. Costantino Creton for new insights on adhesion mechanisms, Dr. David Martina for help with adhesion testing and Prof. Anke Lindner for her support and encouragement in the course of the fruitful collaboration on the topic of *Preload Responsive Switchable Adhesion* carried out at the Physico-chimie des Polymères et Milieux Dispersés Sciences et Ingénierie de la Matière Molle (PPMD), École Supérieure de Physique et de Chimie Industrielles de la Ville de Paris (ESPCI ParisTech), Paris.

The single fibril buckling and adhesion studies were carried out in collaboration with the Crosby research group, Polymer Science and Engineering, University of Massachusetts Amherst, USA. Help on adhesion testing and discussion of experimental results from Mike Bartlett is gratefully acknowledged. I also wish to sincerely thank Prof. Alfred J. Crosby for guiding new experiments and insightful discussions during my visit.

Dipl. Ing. Günter Marchand, in charge of *Mitranz*, clean room facilities at the Saarland University, is most kindly thanked for the introduction of the equipments and support for the fabrication processes.

Prof. Anand Jagota and Prof. Animangsu Ghatak, both visiting scientists at the INM are sincerely thanked for stimulating discussions and inspiring new research ideas.

Prof. Roland Bennewitz and Dr. Tobias Kraus took time to read parts of my thesis and offered me valuable input. I thank them for their time. Dr. Marcus Koch has been very helpful with microscopy training on the Environmental Scanning Electron Microscope (ESEM) in house and helping at times in imaging tricky samples. I thank him for his support. I thank Birgit Heiland for help with metallography on adhesion test probes.

I wish to thank my colleagues in the Functional Surfaces Group, my office-mates Eva Weber and Sarah Schmidt and the INM administrative staff for their support throughout this work.

Without the routine nourishment provided by the company of good friends this research work could not have been accomplished. My heartfelt thanks to them all with the most special mention of Anja Kasten, Magdalena Eder, Philip Born, Timothy Brooks, Harald Tlatlik, Alex Bracza and the Buschhorn family. Finally, I thank my family for the tremendous support over the distance of thousands of miles they continually extend.

Contents

1	Introduction	1
2	Literature review	7
2.1	State of the art: switchable synthetic adhesive systems	7
2.1.1	Temperature switch	7
2.1.1.1	Structured shape memory polymer	7
2.1.1.2	Non-structured shape memory polymer	9
2.1.1.3	Adhesive-film terminated shape memory polymer	11
2.1.1.4	Metal-polymer hybrid system	12
2.1.2	Magnetic switch: polymer-Ni	14
2.1.3	Mechanical switch: PDMS	15
2.1.4	Pneumatic/mechanical pressure switch: PDMS	16
2.1.5	Compressive/shear displacement switch: PDMS	17
2.2	Gecko adhesive system: lessons from nature	18
2.2.1	The gecko adhesive structure	18
2.2.2	The gecko adhesive dynamics	20
2.3	Contact mechanics: structured surfaces	22
2.3.1	Johnson-Kendall-Roberts- JKR theory	22
2.3.2	Limitations of JKR theory	23
2.3.3	Contact adaptability	25
2.3.3.1	Geometry of a sub-contact	25
2.3.3.2	End-shape of a sub-contact	26
2.4	Contact mechanics: switchability in adhesion	28
2.4.1	Interface contact length: macroscopic view	28
2.4.2	Interface contact length: microscopic view	30
2.5	Summary	32
3	Experimental: sample fabrication and test methodology	34
3.1	Structuring of polymers	34
3.1.1	Polydimethylsiloxane, PDMS	34
3.1.2	Photolithography	36
3.1.2.1	Spin coating	37
3.1.2.2	Thin film processing	37
3.1.3	Silanization procedure	38
3.1.4	Soft molding	39

3.2	Adhesion test methodology	40
3.2.1	Adhesion test devices	40
3.2.1.1	<i>Macroscopic Adhesion testing Device</i>	41
3.2.1.2	<i>Microtack</i>	42
3.2.1.3	<i>Contact Adhesion Testing device</i>	42
3.2.1.4	<i>ESEM in situ</i> test device	44
3.3	Typical results	45
4	Bioinspired pressure actuated adhesive system	47
4.1	Introduction	48
4.2	Experimental methods	50
4.2.1	Fabrication of SU-8 lithographic templates	50
4.2.2	Soft molding	50
4.2.3	Sample Characterization	51
4.2.4	Adhesion measurements	53
4.3	Results	55
4.3.1	Adhesion states and repeatability	55
4.3.2	<i>In situ</i> video and SEM results	56
4.4	Discussion	59
4.4.1	Effect of preload change	60
4.4.2	Inferences from the <i>in situ</i> tests: low preload	60
4.4.3	Inferences from the <i>in situ</i> tests: high preload	61
4.4.4	Insights from theory	62
4.5	Conclusions and outlook	63
5	<i>In situ</i> observation of contact mechanisms in bioinspired adhesives at high magnification	65
5.1	Introduction	65
5.2	Experimental methods	66
5.3	Results and discussion	67
5.3.1	Influence of pillar tip shape on adhesion	67
5.3.2	Bending and buckling of pillars (pressure switching behaviour)	69
5.3.3	Backing layer response to applied pressure	70
5.4	Conclusions	71
6	Preload responsive adhesion: effects of aspect ratio, tip shape, and alignment	72
6.1	Introduction	73
6.2	Experimental methods	74
6.2.1	Fabrication of micropillars with end-flaps: Type 1 adhesives	74
6.2.2	Fabrication of micropillars having tips with round edges: Type 2 adhesives	76
6.2.3	Adhesion Testing	78
6.2.3.1	Test method	78
6.2.3.2	Sample alignment	79

6.3	Results	80
6.3.1	Aspect ratio	80
6.3.2	Evolution of stress	82
6.3.3	Video results	84
6.3.4	End-flap orientation	88
6.4	Discussion	89
6.4.0.1	Point 1: Fibril buckling	89
6.4.1	Point 2: Stresses for adhesion loss	92
6.4.1.1	Stress regime 1	92
6.4.1.2	Stress regime 3	95
6.4.1.3	Stress regime 2	96
6.4.2	Point 3: Adhesion Strengths and aspect ratio	96
6.4.3	Point 4: Sample alignment	97
6.5	Summary	98
6.6	Conclusions	100
7	Buckling of an adhesive micropillar	101
7.1	Introduction	102
7.2	Experimental methods	103
7.2.1	Photolithography	103
7.2.2	Soft molding of single micropillars	103
7.2.3	Characterization of single micropillars	104
7.2.4	Adhesion testing	105
7.3	Results	107
7.3.1	Pull-off strength as a function of preload stress	107
7.3.2	Buckling as a function of preload stress	107
7.3.2.1	Low preload: No buckling	107
7.3.2.2	High preload: Reversible buckling	109
7.3.2.3	Micropillar slippage: Irreversible buckling	111
7.4	Discussion	113
7.4.1	Aspect ratio	113
7.4.2	Preload	115
7.4.2.1	Slippage of a micropillar	116
7.4.3	Comparison to Euler buckling theory	117
7.5	Conclusions	120
8	Summary and Outlook	122
	Literature	134
	Appendices	135

List of symbols, abbreviations and definitions

Symbols

α	Coefficient of thermal expansion (ppm/°C)
d	Micropillar diameter (m)
E	Young's modulus of material (Pa)
E^*	Plain strain Young's modulus of material (Pa)
F_c	measured maximum tensile force i.e. pull-off force for an adhesive detachment
F_{crit}	critical force for Euler-Bernoulli buckling of a vertical pillar
h	Micropillar length (m)
k	Spring constant (N/m)
ν	Poisson's ratio
σ_{crit}	critical stress for Euler-Bernoulli buckling of a vertical pillar
T	Temperature in °C
T_g	Glass transition temperature in °C

Abbreviations

AR	Aspect Ratio: micropillar length divided by its diameter, (h/d)
CTE	Coefficient of thermal expansion
DMA	Dynamic mechanical analysis

ESEM	Environmental Scanning Electron Microscope
PDMS	Polydimethylsiloxane
RMS	Root mean square
SEM	Scanning Electron Microscope
SMP	Shape memory polymer
UVO	Ultra Violet Ozone

Definitions

Preload stress:	Applied maximum compressive force divided by the test probe area for micropillar arrays or undeformed micropillar cross section area for single micropillars, (Pa).
Pull-off strength:	Measured maximum tensile force divided by the test probe area for micropillar arrays or undeformed micropillar cross section area for single micropillars, (Pa).

Chapter 1

Introduction

Imagine the experience of a long and peaceful bath. A longish contact with water which is absorbed by the tiny capillary pores has made the skin very soft. The soft gel-like skin surface deforms easily under its surface tension forming undulations [Mora2010]. During drying the skin slowly hardens as the water leaves the tiny pores returning to its normal shape. Everyday experience teaches us to smear moisturizers on our bodies preferably before the skin completely dries and stiffens. A softer skin enables easy spread of the moisturizer covering a larger surface area, possibly maximizing the health benefits. Such an interplay of *elasticity* of any given soft solid and the *surface tension forces* is difficult to observe experimentally.

Arzt and co-workers, by judicious experimentation, were able to demonstrate that the surface *capillary forces* positively influence the adhesion of the gecko spatulae at a nanoscopic level [Huber2005]. Monolayers of water condensed from atmospheric humidity contributed to capillarity. This was previously thought *not* to be the case. Gecko adhesion was attributed solely to *van der Waals forces* [Autumn2002]. The debate took an interesting turn at the **International Gecko Workshop** organized by the INM-Leibniz Institute for New Materials, Saarbrücken in July 2010. During the discussions new results presented by H. Gao [Chen2010] made it clear that the elasticity changes in the material of the gecko adhesive system itself, further enhanced adhesion in the presence of humidity; reconfirmed experimentally by Autumn and co-workers [Puthoff2010]. Thus van der Waals forces, cap-

illary forces and the elasticity changes in material due to surface tension effects have now been acknowledged as contributing together to the adhesion in geckos. Yet, there are still uncertainties as to the exact nature of their combined influence.

In conclusion, the combined effect of different short range forces such as capillary forces and van der Waals forces on the material properties of the adhesive and the resulting contact mechanics of adhesion is so intricate that its full understanding has easily evaded scientists for over a decade.

The above story presents but an introductory snapshot of a much broader research area of **bioinspired adhesion**. It suggests that our present understanding of the natural adhesive systems is still mostly at a preliminary stage and perhaps therefore our ability to mimic them limited. Importantly, it hints at the availability of enough room to explore the field further, especially given the non-availability of an optimized synthetic mimic to date. Present Chapter introduces the different natural animal adhesive systems, most of which depend on hairy attachments. The emphasis will be on their untapped potential.

Geckos, sea-stars, spiders, flies, cockroaches, beetles and ants are some examples from nature which have been the focus of research in the field of *bioinspired adhesion* for their unique adhesion capabilities. The natural adhesive systems seem to function on almost any surface present in an animal's environment, be it rough, dirty or even slippery and inclined at an angle to the horizontal or even over-hanging. Further, these animals use their attachment systems for locomotion as well. Such locomotion poses the apparently contradictory requirements of repeated attachment and detachment. Generally the animal's physiological material system itself is able to independently address such contradictory demands [Federle2006]. The natural adhesive is *inherently capable to switch* repeatedly between the states of attachment and detachment. This is the most noteworthy functionality from the point of view of a material scientist. The main focus of this work is to understand and develop ways to incorporate such a unique switchability in synthetic bioinspired adhesive systems.

Early on in the area of bioinspired adhesion, biologists showed that animals have *structured adhesive surfaces* (Autumn *et al.* [Autumn2000] and Gorb and co-workers [Gorb2000], [Jiao2000]). Further, the structural sophistication of these attachment devices was shown to

be consequent to the animal's body weight [Arzt2003]. Heavier animals such as geckos possess hierarchically patterned structuring in contrast to single level micrometer structuring found in lighter animals such as ants or beetles. Arzt *et al.* elucidated that such a subdivision of the locomotive toe pads resulted in a drastic change in mechanics of contact formation. In spite of a wide diversity in animals that are able to produce adhesion, all have either smooth- or hairy-subdivisions of toe pads as adhesive organs. Of these two basic designs, evolution has opted for the hairy one in most animal groups [Federle2006]. Figure 1.1 shows the microscopic hairy attachment systems (SEM images) for different animals (insets). The

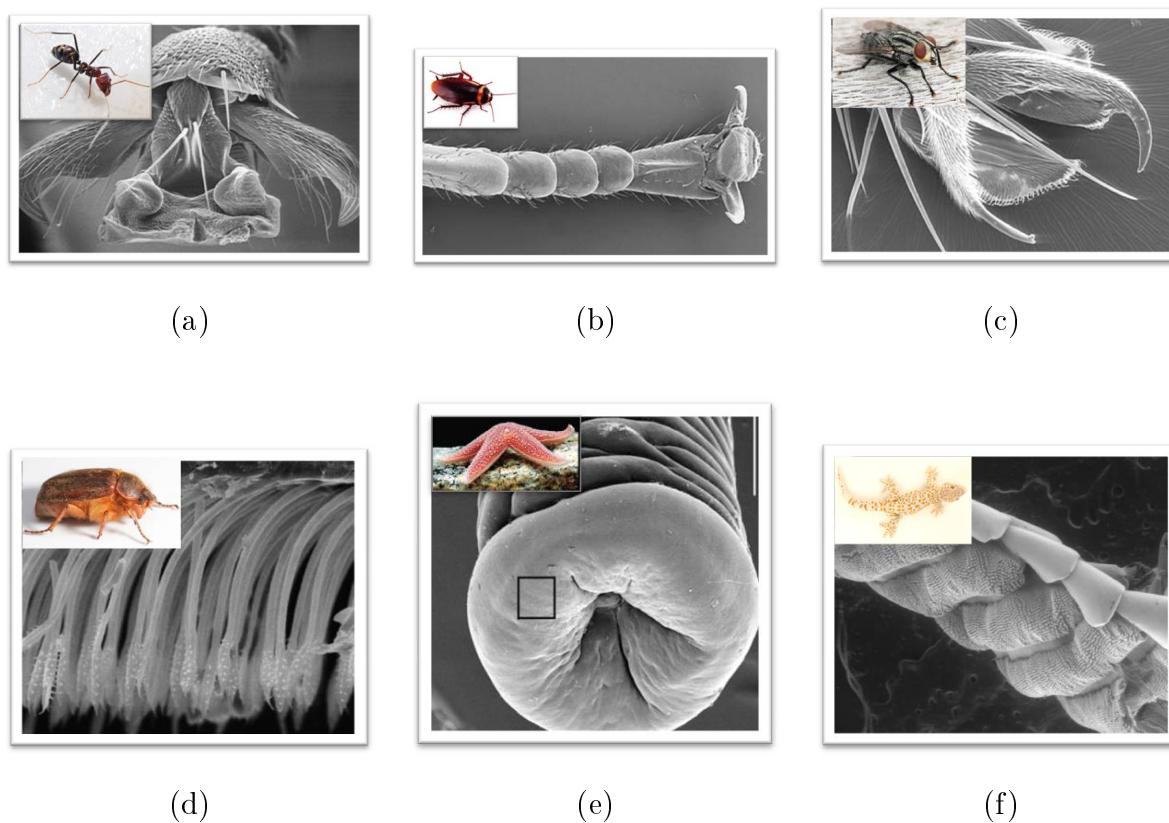


Figure 1.1: Natural adhesive systems. Animal-attachment system of : (a) Ant, (b) Cockroach, (c) Fly, (d) Beetle, (e) Sea-star and (f) Gecko. All show arrays of hair-like endings on the toe-pads. Inset image sources: (a), (b) and (c) personal communication from Henry Firus (<http://www.flagstaffotos.com.au>) dated 20.01.2012, (f) courtesy J. Blau. Sources for micrographs: (a) [Federle2000], (b), (c) and (d) [Peattie2009], (e) [Santos2005] and (f) taken at ESEM, FEI Quanta 400 F with M. Koch.

dominating feature among all these animal attachment systems are the hairs, seen at high magnification in the micrographs in Figure 1.1.

The particularities of an adhesive system such as the arrangement of pads, orientation of hairs, presence or absence of claws etc., however, are refined by evolution to suit the specific demands of the different animals. For example, all insects that rely on hairy attachment systems are known to secrete adhesive fluids. The nature of such secretions in hairy attachment systems is not fully known and the understanding of their role in adhesion remains limited as discussed in the work of Gorb and co-workers [Jiao2000] and Federle and co-workers [Dirks2011]. Beetles, for example, secrete an adhesive fluid in addition to using their hair for attaching to a surface. By secreting the fluid beetles are able to fill in the crevices which have length scales smaller than the hair-tip itself, thereby maximizing contact on rough surfaces [Bullock2008]. Similarly, at roughness scales larger than those of the beetle hair ($>50 \mu\text{m}$), the hairs buckle and are ineffective for attachment, thus requiring claws for adhesion. Thus, the beetle hairy system (Figure 1.1 (d)) appears to maximize the capillary forces for attachment to rough surfaces. This has opened new avenues for designing bioinspired adhesives which stick to rough and wet surfaces as shown in the recent work by Varenberg and Gorb [Varenberg2008a]. Overall, however, it appears that the research area of adhesion in presence of fluids remains largely unexplored.

Adhesion appendages similar to the claws in beetles are also common in other insects. The attachment systems of ants and bees, for example, consists of a flexible pad, the arolium, between the claws (Figure 1.1 (a)) [Federle2001a]. Whereas the beetles use their claws to aid attachment on rough surfaces, ants use their soft flexible pad for attachment to smooth surfaces. These appendages, specific to a roughness scale, are noteworthy. There are no synthetic devices known to successfully assimilate this knowledge.

Yet another feature of many hairy attachment systems is the disc shaped terminal ending of the hairs. Underwater attachment systems in animals such as sea urchins and sea stars have tube shaped feet which end in a relatively softer disc shape (Figure 1.1 (e)) [Santos2005]. Gorb and co-workers [Santos2005] studied the elastic nature of the soft discs, crediting them with uniform stress distribution at the contact. This might preclude the undesired peel off

due to wave-generated forces in water. We do not know of any under-water synthetic adhesives that have successfully employed these principles to accomplish reversible attachment to rough surfaces.

Most animals can also walk on level surfaces, climb upward and downward so that the direction of forces acting may easily detach the adhesive hairy pad. However, the natural adhesive systems seem to deal with these complex force changes without a problem. In cockroaches, for example, two different types of pads give the direction dependent frictional force needed to provide traction during locomotion (Figure 1.1 (b)) [Clemente2008]. Directionality of adhesion pads is also observed in geckos. In fact, the gecko hierarchical attachment system is special in many different ways. It produces adhesion that is clean and dry [Hansen2005] as well as rapidly and repeatedly tunable by simple orientation change [Autumn2006] on most existing surfaces. Climbing robots would benefit hugely from such attachment systems [Sitti2003]. In conclusion, an adhesive like that of the gecko, which produces clean and dry adhesion to almost any surface reversibly and repeatedly, is all but ready. The present thesis focuses mainly on the aspect of *reversibility* in bioinspired adhesives.

This thesis is organized as follows: Chapter 2 reviews the state of the art reversible bioinspired adhesive systems. The gecko adhesive system is also studied and the basic contact mechanics are understood with the help of theory. Chapter 3 presents the experimental approach to fabrication and testing of bioinspired adhesives. Mechanical instability induced adhesion switching is presented in Chapter 4. Chapter 5 presents the high magnification visualization of the contact phenomena during adhesion processes. Preload responsive adhesion is investigated further by studying the effects of aspect ratio, contact shape and orientation of the fibrils on adhesion in Chapter 6. Adhesion and buckling of a single micropillar is investigated in Chapter 7. The thesis concludes with a summary of the presented work and an outlook on switchable adhesion in Chapter 8.

Note

- Chapter 4 published: D. Paretkar, M. Kamperman, A. S. Schneider, D. Martina, C. Creton and E. Arzt, *Mat. Sci. Eng. C-Bio. S.*, 6(31), 1152, **2011**.

- Chapter 5 published: D. Paretkar, A. S. Schneider, E. Kroner, and E. Arzt, *MRS Comm.*, Oct, 1, **2011**.
- Chapter 6: D. Paretkar, M. Kamperman, R. McMeeking, Anke Lindner, C. Creton, Anand Jagota and E. Arzt, *Preload responsive adhesion: effects of aspect ratio, tip shape, and alignment*, in preparation.
- Chapter 7: D. Paretkar, M. Bartlett, R. McMeeking, A. Crosby and E. Arzt, *Buckling of an adhesive micropillar*, in preparation.

Chapter 2

Literature review

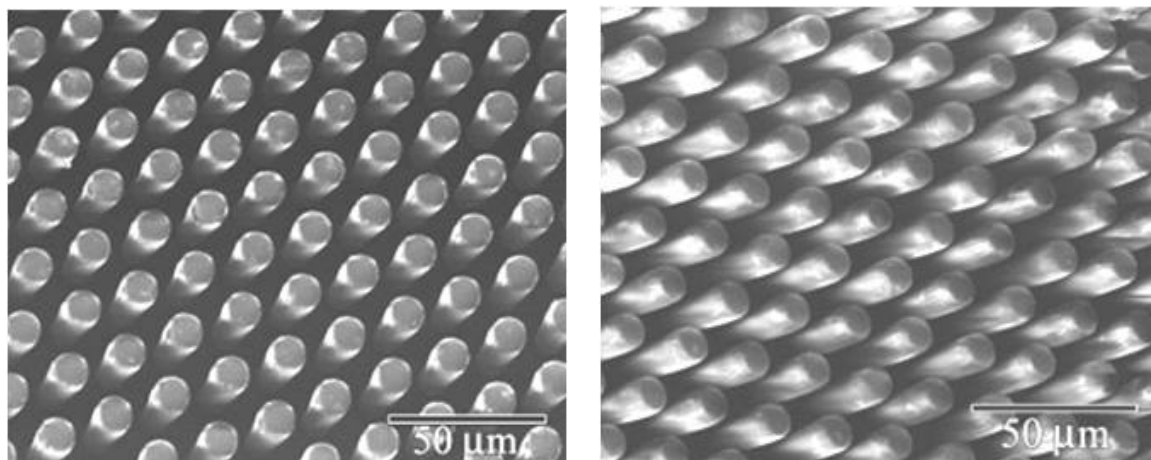
2.1 State of the art: switchable synthetic adhesive systems

Bioinspired synthetic adhesive systems have used temperature, magnetic field, mechanical stretching and pneumatic or mechanical pressure as external stimuli to generate reversible/switchable adhesion. The working principles, advantages and limitations of switchable adhesive systems, known to date, are presented here.

2.1.1 Temperature switch

2.1.1.1 Structured shape memory polymer

Arzt and co-workers developed a bioinspired switchable adhesive based on thermally responsive shape memory polymer (SMP) [Reddy2007]. Generally an SMP is a block co-polymer having two different glass transition temperatures (T_g) corresponding to the two constituent blocks. The lower T_g of the softer polymer segment serves as a transition temperature above which the polymer stiffness drops by an order of magnitude. However, in the softened state its physical form is preserved by the stiffer polymer segment with a much higher T_g . The polymer's overall softness above the transition temperature makes it easily deformable. Reddy *et*



(a)

(b)

Figure 2.1: SEM images of (a) vertical fibril configuration (adhesive state) and (b) tilted fibril configuration (non-adhesive state) of a structured shape memory polymer [Reddy2007].

al. [Reddy2007] combined the deformability of the SMP with the surface structuring based adhesion enhancement in their system.

The enhanced contact area was generated by a structured vertical array of fibrils in the SMP, Tecoflex (Figure 2.1). In their room-temperature default state, the vertical arrays gave rise to a high adhesion state (Figure 2.1 (a)). When the sample was heated above the transition temperature ($\geq T_g$ of softer segment), the softened fibrils were controllably sheared to orientate away from the contact surface. Cooling to room temperature while retaining the shear, created tilted polymer fibrils. This resulted in a drastic reduction of the interface contact area in the frozen-in low adhesion state (Figure 2.1 (b)). Upon reheating above the transition temperature, the fibrils "remembered" their original vertical configuration. Heat cleaved the physical cross-links in the soft segment returning them in their default adhesion state.

The presented adhesion switch based on a structured SMP was the first switchable bio-inspired adhesive. It successfully demonstrated that a change of contact area by orientation change of fibrils, similar to that of the geckos, can also be achieved for synthetic adhesives. However, the fibrils failed to recover completely from their sheared non-adhesive state to their original adhesive state. This resulted in somewhat lower adhesion in the recovered

state. Also, as the shape memory polymer can only be switched once, the adhesive cannot be used repeatedly.

2.1.1.2 Non-structured shape memory polymer

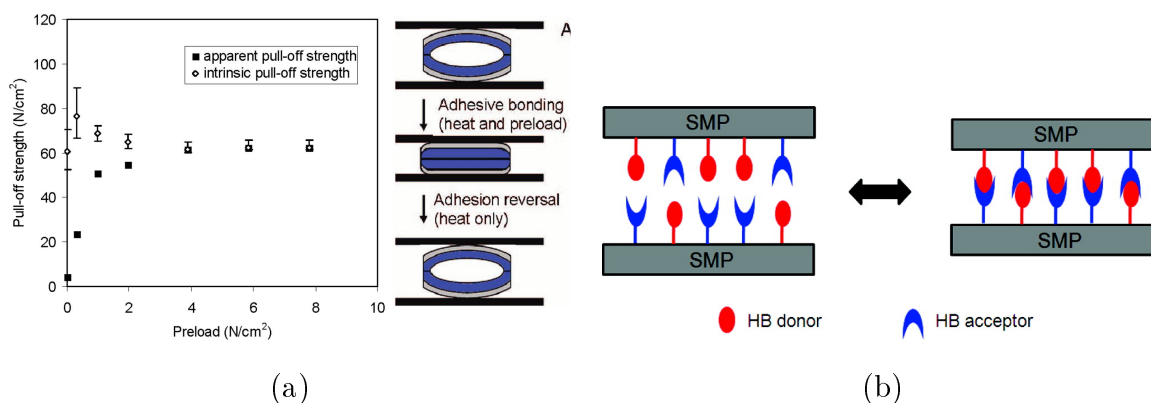


Figure 2.2: Reversible adhesion by (a) softening of a layered polymer network system [Xie2008] and (b) SMP induced enhanced hydrogen bonding [Wang2010].

SMPs can be used as reversible adhesives, even without the surface structuring to enhance adhesion. The adhesion, in this case, was achieved by the improved contact adaptability of the SMP in its soft heated state. Xie and Xiao developed a layered polymer network composed of an elastomeric adhesive polymer and a SMP [Xie2008]. The network polymer formed a curved stripe shape at room temperature. When the stiff thermoset polymer was heated to well above above T_g ($\approx 40^\circ\text{C}$), its modulus dropped, making it more compliant. In the compliant state compressive preload (5 N/m^2) was employed to form an adhesive contact between the softened SMP and the test surface (Figure 2.2 (a)). When cooled to room temperature, the adhesion was retained and the interface strengths were as high as 60 N/m^2 . Upon reheating above T_g , the SMP "remembered" its initial curvature thereby peeling off and releasing the adhesion.

Xie and co-workers have also used the shape memory effect to enhance hydrogen bonding interactions between two rigid polymers [Wang2010]. Although non-covalent in nature, similar to van der Waals bonding, hydrogen bonding is not universal and relies on specialized donor-acceptor interactions, *e.g.* H-bond (HB) donor and acceptor interaction at the surfaces of polymers (Figure 2.2 (b)). Difficulties to this approach can arise if the HB interactions

become stronger compared to the bulk strength of the polymers. Also, surfaces of polymers almost always have unsaturated bonds. This may, additionally, cause problems by interfacial chain entanglement between the two polymers. Reversibility in this case was not achieved solely on the basis of temperature induced shape memory effect. Instead, solvents were used to break the HB interactions, which further complicate the use of such an adhesion switch.

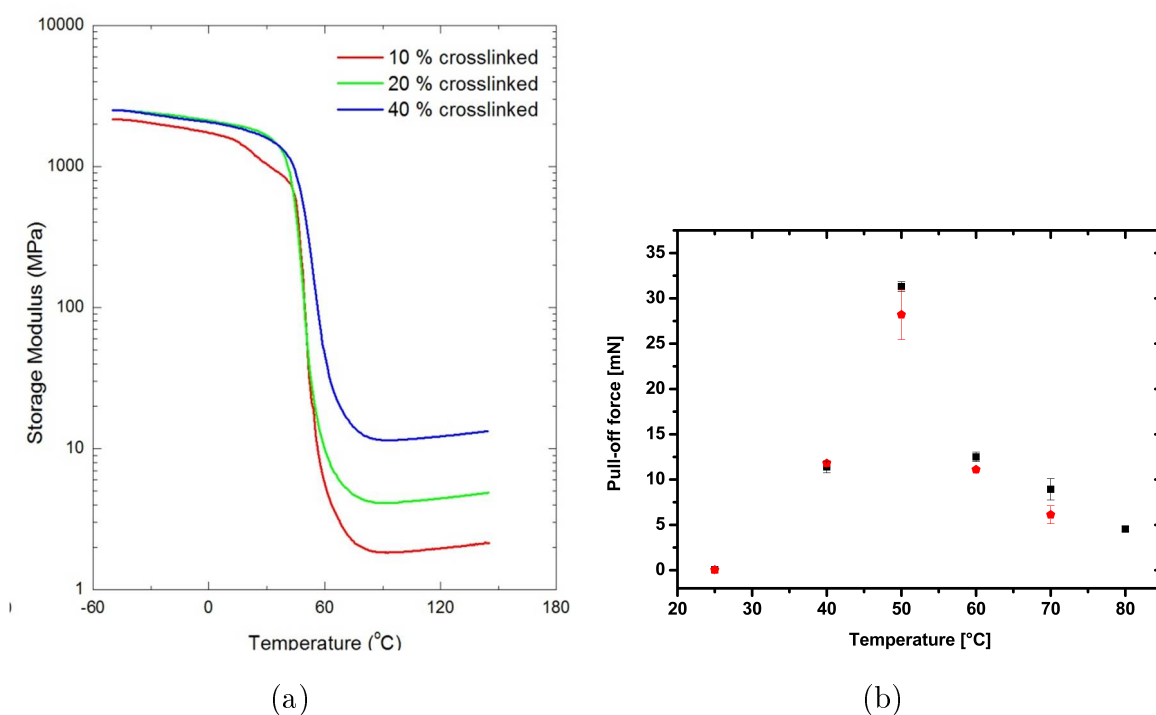


Figure 2.3: (a) Drastic change in elastic modulus at the glass transition temperature (DMA on (tBA+PEGDMA), personal communication from C. Frick). (b) High adhesion near T_g during heating (squares) or cooling (pentagons).

Similarly, by tuning the elastic modulus changes and T_g , Frick and co-workers¹ fabricated reversible adhesive systems based on SMPs. Polymers were tailored to vary in elastic moduli (E) by a large magnitude at a constant glass transition temperature (Figure 2.3 (a)). Polymer networks consisting of linear chains of tetra-Butyl acrylate (tBA) were cross-linked with poly (ethylene glycol) dimethacrylate (PEGDMA). In their room temperature state these

¹This work was initiated as a side project along with the present work. Polymer network systems were prepared by the group of Prof. Carl P. Frick, Department of Mechanical Engineering, University of Wyoming, USA. Adhesion tests were performed by Ms. Pranoti Kshirsagar, Summer Internship Project-June-July 2011.

stiff network polymers were non-adhesive. When heated above the T_g ($\approx 50^\circ\text{C}$), these networks softened considerably increasing the contact adaptability and therefore the adhesion, Figure 2.3 (b). Both heating up and cooling down cycles showed at least a three-fold increase in adhesion near the T_g , Figure 2.3 (b). Beyond the T_g adhesion drops as the viscoelastic effects dominate. Larger energy fraction gets dissipated within the system during peeling. Different sets of T_g as well as structuring of polymer surfaces is underway to create adhesive switches. Such systems may be envisaged for biological application by tuning the T_g nearer to body temperatures and activating the adhesion by in-vivo insertion.

2.1.1.3 Adhesive-film terminated shape memory polymer

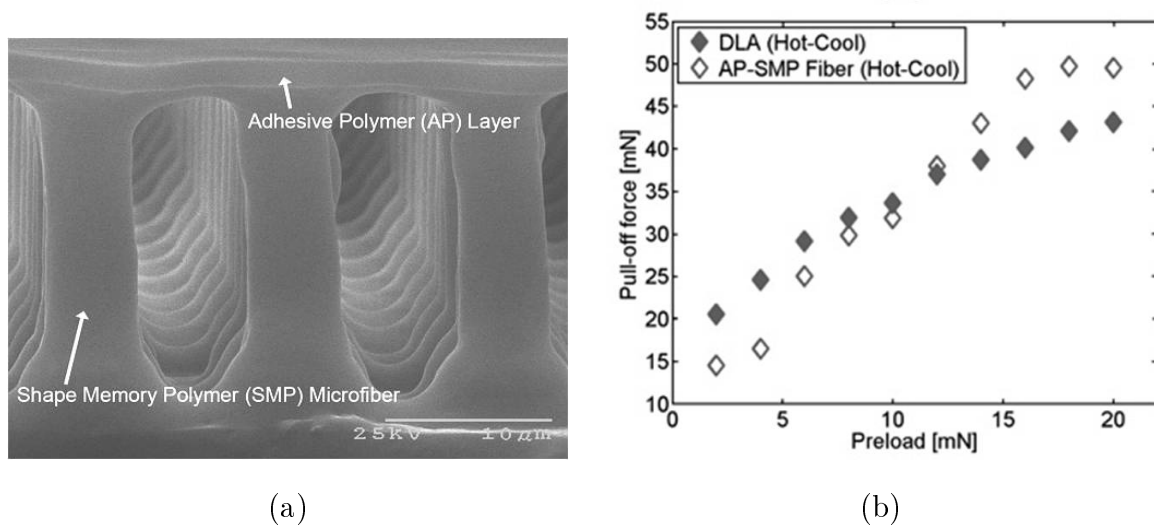


Figure 2.4: (a) Film-terminated shape memory polymer fibrillar array (AP-SMP) and (b) adhesive performance of AP-SMP under controlled temperature conditions in comparison to film-terminated non structured SMP (DLA) [Kim2009b].

Sitti, Xie and co-workers [Kim2009b] combined the advantages of temperature controlled bulk softening of SMP with those gotten by structuring a surface. An array of SMP fibrils was coated with a terminal film of an adhesive polymer (Figure 2.4 (a)). These adhesive structures were heated above the transition temperatures and compressed when hot. Contact adaptability was enhanced due to material softening and the compliant fibrillar structures, generating a high adhesion state. Retaining the compression and cooling down to room

temperature retained the attached state. The room temperature detachment was driven by the high intrinsic adhesive strength of the terminal polymer film.

However, it appears that even without the structuring, a double layer AP-SMP gave similar adhesion enhancement 2.4 (b). Different combinations of hot and cool conditions during loading and unloading were shown to having varying influences on the adhesion. Overall, this study does not come out clear on whether there was any significant gain in adhesion performance compared to the simple SMP based systems of Xie *et al.* [Xie2008]. Also, the elaborate and complex fabrication effort involved [Kim2009b] undermines greatly any practical use of such a combinatorial approach.

2.1.1.4 Metal-polymer hybrid system²

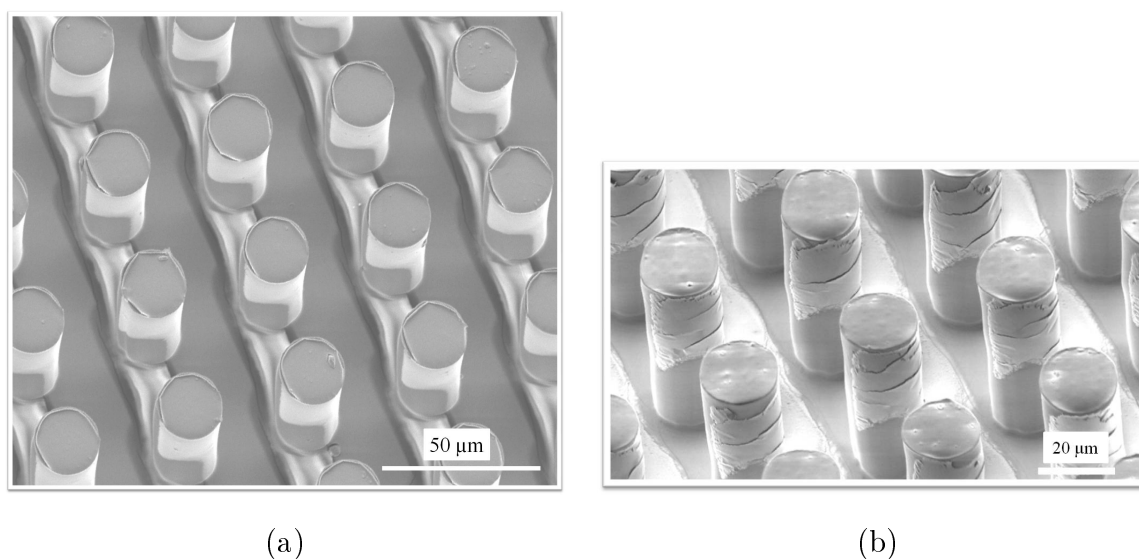


Figure 2.5: SEM images of Au-PDMS hybrids showing (a) side Au film as brighter rectangular patch on PDMS fibrils and (b) cracks on Au film after repeated adhesion tests [Trejore2010].

The phenomenon of bending of a bimetallic strip when heated is based on the mismatch in coefficients of thermal expansion (CTE) between the two metals. The same principle was employed to reversibly change the interface contact area of Au-PDMS fibrils [Trejore2010].

²Work on metal-polymer switchable systems was initiated within the framework of present work. Initial findings were reported in the Masters thesis by Victoria Liliana Mejia Trejore [Trejore2010].

Au was thermally evaporated on a tilted PDMS fibrillar array such that the metal coated only one side of the fibrils. In addition to the difference in their CTE ($\alpha_{PDMS} \approx 20 \alpha_{Au}$), the metal and the polymer also differed in their elastic moduli ($E_{Au} \approx 10^4 E_{PDMS}$). Consequently, strain mismatch during thin film deposition led to pillars being slightly tilted to the gold side (Figure 2.5). Additionally, the slight temperature increase of the sample surface above the room temperature during the thin film deposition may also contribute to thermal stress due to CTE mismatch.

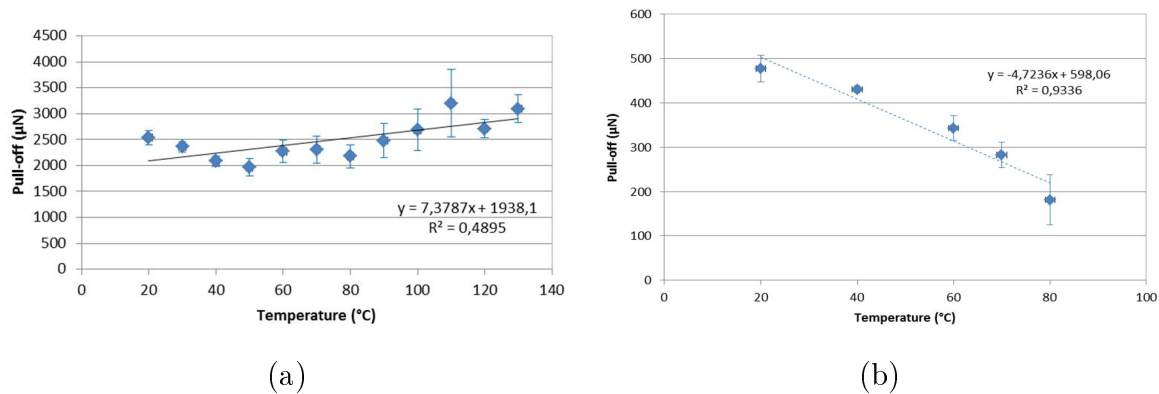


Figure 2.6: Response of fibrillar adhesive to temperature for a (a) virgin (no Au coating) fibrillar PDMS array and (b) side Au-coated fibrillar PDMS array [Trejore2010].

Measurements were done on Au-PDMS hybrid structures and compared with those on the virgin PDMS structure with similar dimensions (Figure 2.6). The starting adhesion strengths for the Au-PDMS hybrid structures were lower compared to virgin PDMS sample. This was attributed to the initial tilt in the Au-PDMS fibrils, which reduced fibril-probe interface contact area. When adhesion was measured as a function of increasing temperature, it was found that a drop in adhesion for the Au-PDMS sample resulted (Figure 2.6 (b)). The adhesion dropped by more than 50% of its room temperature value for temperatures around 80°C . For similar high temperatures, the control samples did not show much change from their room temperature adhesion (Figure 2.6 (a)). The drop in adhesion at high temperatures was attributed to the increase in tilt of the Au-PDMS fibrils towards the metal side due to mismatch strains.

Upon cooling, the adhesion reversed back to the room temperature value. This demonstrated the ability of using metal-polymer hybrid systems as temperature reversible adhesives. How-

ever, the repeatability of adhesion values from one test to the other was poor [Trejore2010]. Cracking of the gold film was thought to be one of the reasons that hindered the repeatability of the hybrid system. SEM micrographs of the Au-PDMS fibrils, after adhesion tests showed cracks in the gold film (Figure 2.5 (b)). Repeated loading-unloading of the Au-PDMS fibrils most likely caused the observed cracking [Paretkar2008]. Once cracked, the gold film lost its integrity which localized the effect of strain mismatch to smaller regions in the film. Localized strain mismatch failed to generate the desired tilt in the entire fibril (Au-PDMS) during new trials, resulting in poor repeatability.

2.1.2 Magnetic switch: polymer-Ni

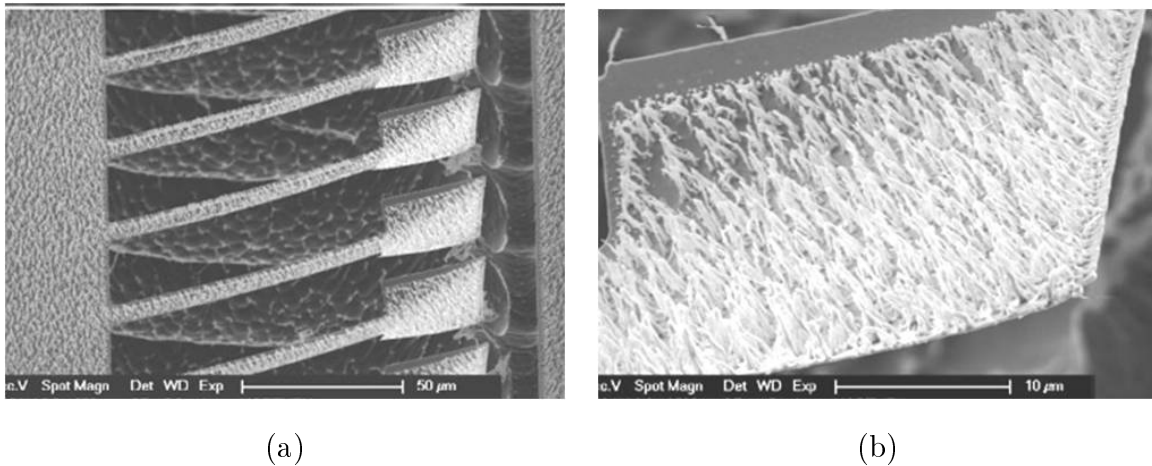


Figure 2.7: Magnetic field induce adhesion switchability in structures composed of (a) Ni-microcantilevers coated at ends with (b) polymer nanorods [Northen2008].

Turner and co-workers demonstrated the use of a magnetic field as an external stimulus to reverse adhesion in metal-polymer system [Northen2008]. The hybrid system combined the adhesive property of a structured polymer with the magnetic response of a metal to generate switchable adhesion. Microfabricated nickel cantilevers acted like the gecko setae (Figure 2.7 (a)), whereas the terminal polymer nanorods provided adhesion similar to the gecko spatulae (Figure 2.7 (b)).

The polymer nanorod array was coated selectively on the microcantilevers. The resulting material mismatch deposition stresses made the cantilevers bend. The bent cantilevers

acted like a spring enhancing contact adaptability. This resulted in a default high adhesion state. When the magnetic field was switched on, the bent cantilevers rotated away from the test surface, drastically reducing the contact area. This resulted in a low adhesion state [Northen2008]. However, the reported adhesion strengths were relatively low (≈ 14 Pa).

2.1.3 Mechanical switch: PDMS

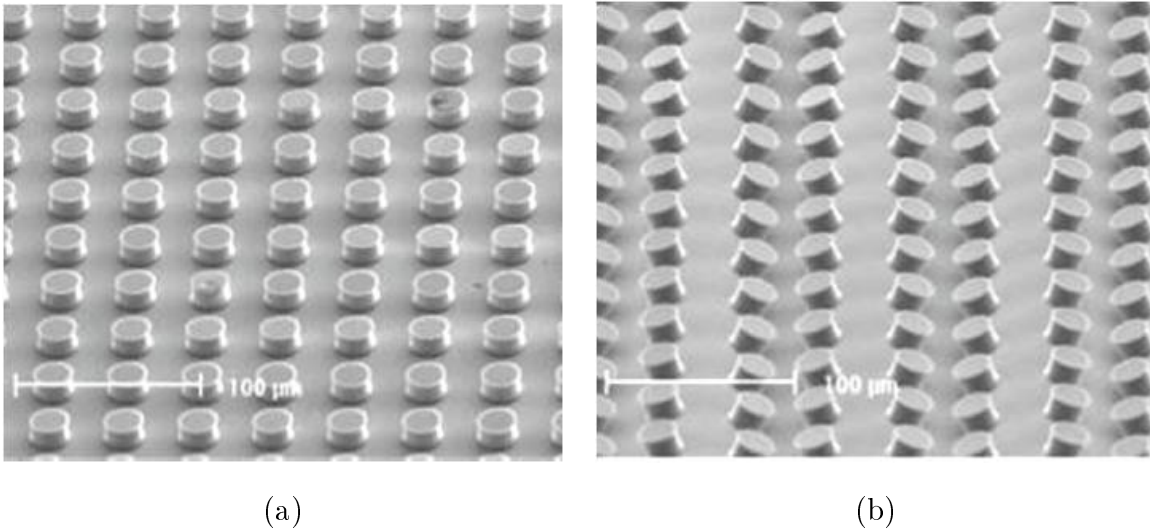


Figure 2.8: Structured PDMS sheet in (a) stretched state with vertical fibrils (high adhesion) and (b) wrinkled state with tilted fibrils (low adhesion) [Jeong2010].

Suh and co-workers combined the elastic properties of surface wrinkles with the structuring based adhesion enhancement in an elastomeric sheet to tune adhesion [Jeong2010]. A sheet of PDMS contained micropillar structures at the surface. The wrinkles were generated by inducing a strain mismatch between a stiff SiO_x film ($E \geq 100$ MPa) on the surface of a soft PDMS film ($E \approx 2$ MPa). When the film was mechanically stretched, all micropillar tips were aligned to a contacting surface (Figure 2.8 (a)). Vertically aligned pillars offered an increased contact area, giving rise to a high adhesion state. Releasing the stretch made the PDMS film wrinkle back, which misaligned the micropillar tips with respect to test surface. This resulted in reduction of contact area, giving rise to a low adhesion state (Figure 2.8 (b)). The adhesion switch was repeatable over many cycles and functioned in normal as well as shear modes [Jeong2010].

Ultra Violet Ozone (UVO) surface treatment was employed to create the thin SiO_x layer on the patterned PDMS surface. A stiff layer is less adaptable to a surface and reduces adhesion. Therefore, the pillar tips needed to be protected from the UVO, so that they retained an adhesive PDMS top surface. Jeong *et al.* [Jeong2010] used inking techniques to selectively cover the micropillar tips, which is not trivial to optimize. Secondly, getting an optimal wrinkle-pillar geometry was fundamental to the working of their switch. For an optimized wavelength of the wrinkles the pillars were located slightly off the wave peak and the spacing between them such that the bending induced by wrinkling did not make them stick to one another. Spacing pillars widely to avoid sticking, on the other hand, was detrimental for adhesion. Optimizing the design considerations in addition to having a control on the UVO process which formed wrinkles are great experimental challenges. These undermine the overall reproducibility of their adhesive system.

2.1.4 Pneumatic/mechanical pressure switch: PDMS

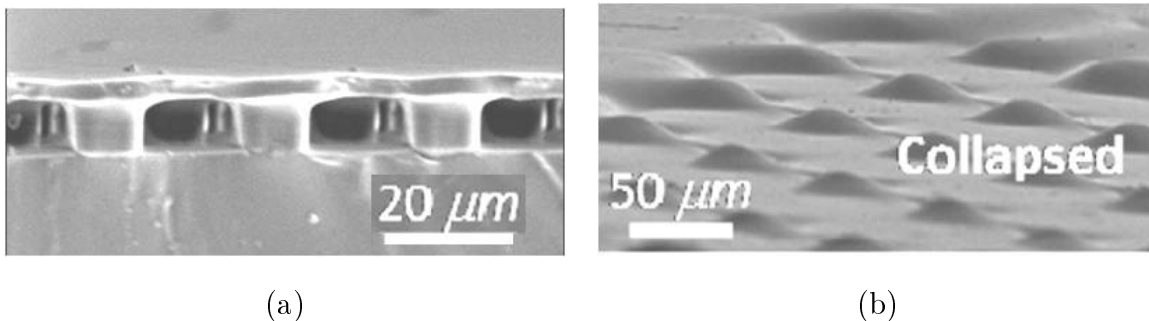


Figure 2.9: Film-terminated fibrillar adhesive in (a) side view of uncollapsed high adhesion state and (b) top view of the collapsed low adhesion state [Nadermann2010].

Jagota and co-workers showed that a terminal film on an array of PDMS fibrils has higher adhesion than that of a continuous film alone [Glassmaker2007]. Using this architecture and optimizing the spacing between the fibrils they prepared a switchable adhesive [Nadermann2010], Figure 2.9. The terminal PDMS film was sucked in using air pressure or mechanical pressure. This caused it to collapse between the pillars and stick to the substrate below. Collapsed film configuration substantially reduced the contact area, resulting in a low adhesion state (Figure 2.9 (b)). Alternatively, when the film was blown up or the pressure removed, it

returned to the original, flat plate-like configuration between the fibrils. The uncollapsed continuous film offered a larger contact area returning to its default high adhesion state (Figure 2.9 (a)).

A major drawback of such an architecture is the delicate nature of the film switching. Optimization of the fibril spacing and film thickness was critical. For, an excessively thick film of the PDMS undermined the adhesion enhancement from the underlying fibrils. And a thinner compliant film easily buckled and stuck too well to the substrate. Thus a narrow range of work of adhesion was available for designing a system that was switchable. Secondly, even in the optimized geometry any excess applied stress permanently collapsed the film. Hence, the application of their switch is restricted to extremely small loads.

2.1.5 Compressive/shear displacement switch: PDMS

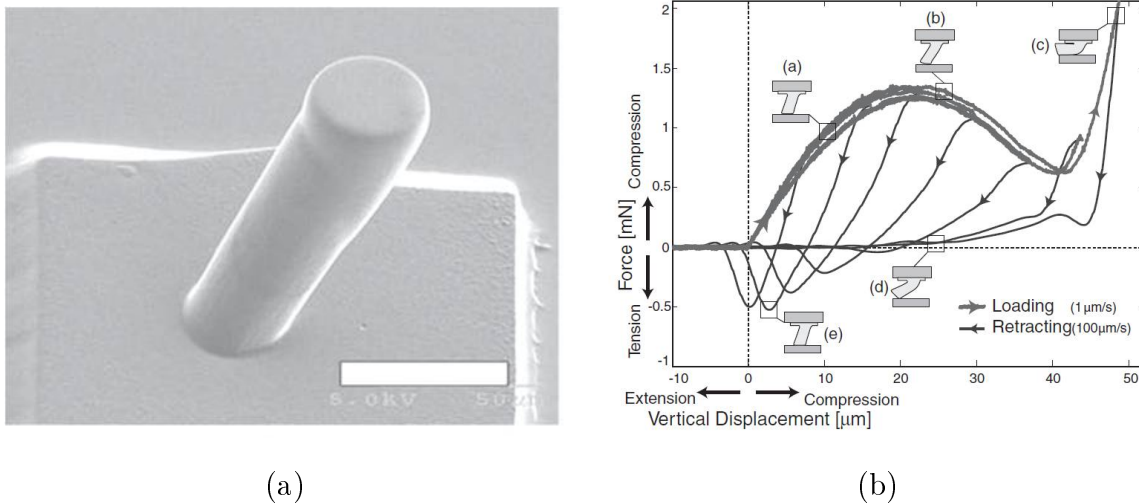


Figure 2.10: Displacement controlled adhesion by (a) single tilted micropillar ($h = 90$ and, $d = 35 \mu\text{m}$) adhesive showing (b) force change as a function of vertical displacement [Menguc2012].

As this chapter was being written a new report by Sitti and co-workers on controllable adhesion has appeared [Menguc2012]. This concurrent work proposed the use of vertical or shear displacement to generate a drastic change in fibril contact area for adhesion control. Their basic adhesive device was an isolated single polyurethane micropillar of diameter 35

μm and length $90\mu\text{m}$ and angled at an inclination of 20° to the horizontal, Figure 2.10 (a). An initial directionality introduced by the tilted fibrils governed the direction of fibril transition induced by compression or shear displacement. Intimate top face fibril contact was achieved by lightly loading the fibril on a given surface. This created the adhesive state. Applying compressive or shear displacement while in the attached state made the fibril lose the adhesive top face contact and slip into a side contact. This change of top to side contact drastically reduced adhesion during retraction at a high displacement rate, Figure 2.10 (b). The basic idea of the adhesion switch used by Sitti and co-workers [Menguc2012] is similar to the mechanical instability induced switchability in adhesion presented in this thesis. However, in their case, control of adhesion was additionally achieved by a shearing motion control that benefited from the fibril tilt. Also rapid retraction compared to loading was employed to release adhesion. A major limitation of their switch appears to be precise control and repeatability in the switchability of adhesion. Sitti and co-workers claim that a force-control measurement led to non-linear response from the adhesive and only a displacement-control test can capture all load states [Menguc2012]. This highly debatable keeping in perspective the work presented here.

In summary, the synthetic switchable adhesives presented above rely on a common working principle: Maximization and minimization of the interface contact area, when achieved reversibly, can result in an adhesion switch. Most of these adhesive systems are inspired by the gecko adhesive system, a much superior naturally available adhesive system (see for *e.g.* <http://robotics.eecs.berkeley.edu/~ronf/Gecko/gecko-compare.html>, Comparison of Gecko-inspired Fibrillar Adhesives).

2.2 Gecko adhesive system: lessons from nature

2.2.1 The gecko adhesive structure

The key to the understanding of the extraordinary adhesion achieved by the gecko and its ability to reversibly and repeatedly switch adhesion is to analyze the underlying structure

of its adhesive. The gecko adhesive system is a three tier structuring of the toe-pad: at the

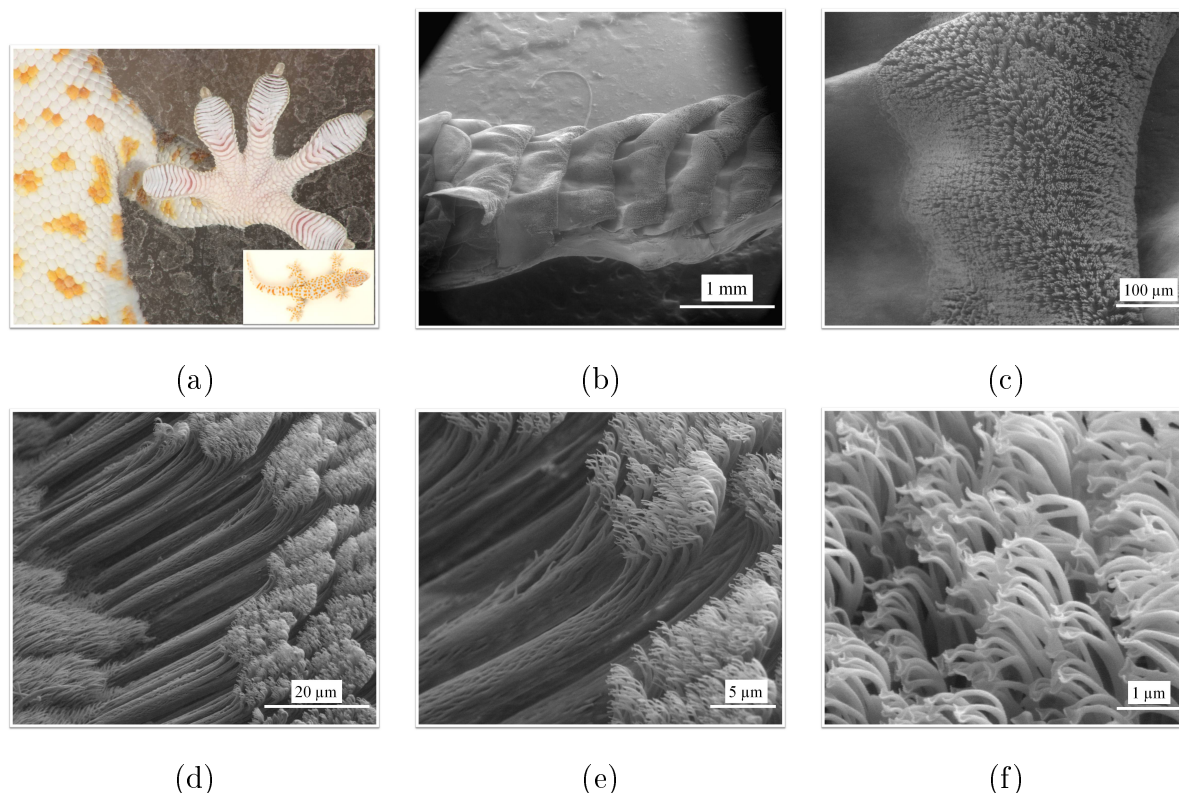


Figure 2.11: Three tiers of the gecko hierarchical adhesive system. (a) Gecko toes (inset, Tokay gecko), (b) macroscopic toe pad and (c) scensor on toes. (d) and (e) Microscopic setae, (f) branched setae into nanoscopic spatulae. Images sources: (a) courtesy J. Blau and (b) to (f) taken in ESEM, FEI Quanta 400 F with M. Koch.

macroscopic, the microscopic and the nanoscopic levels as shown in the Figure 2.11. The gecko toe anatomy can be summarized with the help of the work of Autumn and co-workers [Autumn2008] as follows: The five toes of the gecko foot seen in Figure 2.11 (a) each have some twenty macroscopic leaf-like scensors seen as white lines spanning across the toe. Six of these are seen at a higher magnification in Figure 2.11 (b). Each of these scensors, seen in Figure 2.11 (c), has an array of densely packed setae orientated at angles $<45^\circ$ to the scensor. The setae are approximately $110\text{-}130\ \mu\text{m}$ each in length and $4\ \mu\text{m}$ in diameter at the microscopic level, see Figure 2.11 (d) and (e). The setae terminate in nanoscale spatulae at the last hierarchical level, see Figure 2.11 (f). A spatula forms a contact region of $100\text{-}250\ \text{nm}$ in size. The material system *i.e.*, the protein β -keratin forming the hierarchical structure

is a relatively stiff material with bulk Young's modulus $E \approx 2\text{-}4$ GPa.

2.2.2 The gecko adhesive dynamics

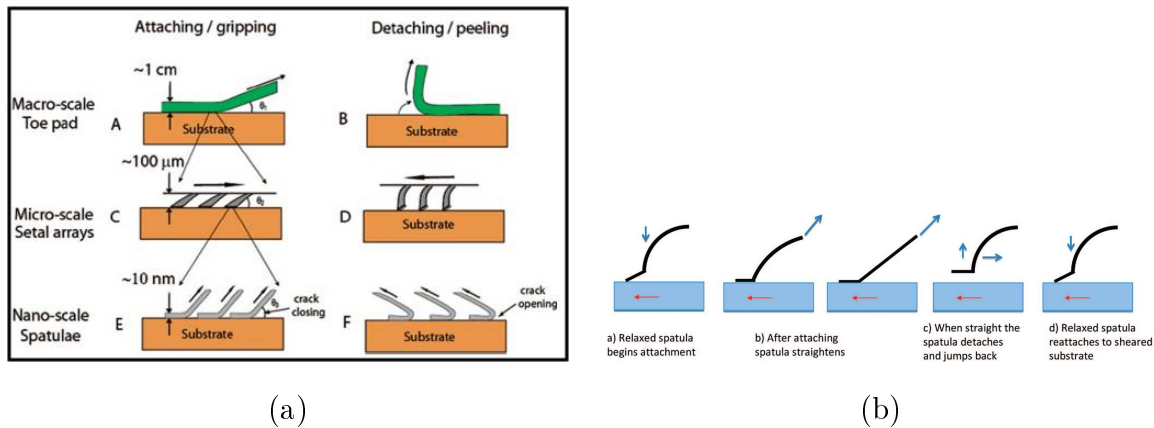


Figure 2.12: The gecko attachment-detachment dynamics. (a) Schematic of attachment and detachment mechanism at the level of a (A and B) toe, (C and D) setae and (E and F) spatulae ([Zhao2009]). (b) Model of attachment-detachment mechanism of a single spatula ([Yamaguchi2009]).

The gecko locomotion involving the coordinated movement of its legs, feet, toes, down to the finest hierarchy of spatular tips is described with the help Figure 2.12 (a) as follows: When a gecko wishes to move and attach to a surface it places one pair of diagonally opposite legs forward as the other pair detaches. The two attaching feet are loaded compressively and pulled inward to the animal's body. The setae flatten from their initial orientation (45°) under small compressive loading. The spatular tips are thus pointing away from the animal's body. However, the slight drag towards its body pulls the setae into tension and brings the spatulae in uniform contact with the surface producing adhesion.

The two detaching feet are able to release the adhesion by simply increasing the angle of the flattened setae above 30° . This makes the setae spring back to their original non-adhesive configuration inducing peeling of the spatula and consequently detachment from surface. A simple orientation change of the setae can thus cause reversal of a strongly adhesive state, as was discovered by Autumn and co-workers [Autumn2002b], [Tian2006] and [Autumn2006]. Creton and co-workers model the setae and the spatulae as curved beams to explain their

stick-slip like working [Yamaguchi2009]. Their model showed that the curved beam-like setae induce an angle dependent coupling between the frictional drag force and the adhesion force which is repeated at the spatula level, Figure 2.12 (b).

Interestingly, the gecko adhesive system does not require active grooming or maintenance. The natural operational environment of the geckos is full of tiny dirt, sand, pollen and other such particulate matter. Yet, the adhesive hairs show resistance to contamination and appear to be self-cleaning. Hansen and Autumn [Hansen2005] ascribe this to the material properties of β -keratin such as low surface tension, high bulk stiffness and hydrophobicity to understand a hair's non-adhesion to other hairs and particulate dirt.

Natural structural feature	Contact mechanics lessons	Design implications
Hairy surface structure.	Effectively compliant material. Fibrils as crack arrestors. Large surface-to-volume ratio.	Ease of surface adaptation. Resistance to peel-off. Less energy expenditure to form contact.
Nanoscale spatular contact ends.	Uniform stress distribution.	Defect tolerance.
Orientation dependent adhesion state.	Drastic contact area change.	Reversible adhesion.
Hard, low surface energy material.	Non self-sticking, repels dirt.	Self-cleaning.

Table 2.1: Lessons from the gecko adhesive system.

Thus, the salient functionalities of the gecko adhesive system can mainly be attributed to the natural hairy structure. The *structure-property* correlation for the gecko system has interesting contact mechanics foundations. A summary of these lessons and their design implications for synthetic adhesives are presented in Table 2.1 and discussed ahead.

2.3 Contact mechanics: structured surfaces

The reasons for high adhesion in the case of the gecko attachment system are examined here. The basis for adhesion of the gecko hairs was shown to be van der Waals forces [Autumn2002], [Arzt2002] (and capillary forces [Huber2005], excluded for present discussion), which are independent of surface chemistry (*i.e.* non-covalent in nature). The splitting of a single contact into fine, multiple sub-contacts considerably increases the van der Waals forces [Autumn2002], [Arzt2003]. This has been explained using the adhesion theory proposed by Johnson, Kendall and Roberts (JKR) [Johnson1971].

2.3.1 Johnson-Kendall-Roberts- JKR theory

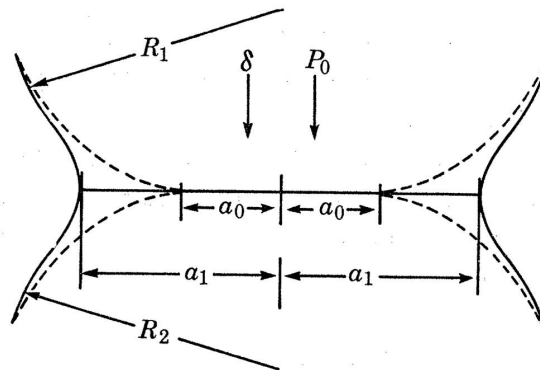


Figure 2.13: Two elastic spheres (radii R_1 and R_2) form increased contact (radius a_1) due to adhesion under normal load (P_0) [Johnson1971].

JKR theory predicts the force of adhesion between two lightly loaded solid surfaces that are elastic and spherical (Figure 2.13). The basis is an energy balance between the stored elastic energy, the applied mechanical energy to form the contact and the surface energy. The equilibrium contact radius derived from this energy balance is given by ([Johnson1971]):

$$a^3 = \frac{R}{E^*} \left\{ F + 3\pi R\gamma + [6\pi R\gamma F + (3\pi R\gamma)^2]^{1/2} \right\}, \quad (2.1)$$

where R is the radius of the spherical solid, E^* is the average plain strain modulus, γ is the energy per unit contact area (*i.e.* interfacial binding energy of the two surfaces) and F

is the small compressive load applied to form the contact. Their analysis predicts a finite tensile force *i.e.* a pull-off force at which the separation of the two spheres occurs:

$$F_c = \frac{3}{2}\pi R\gamma. \quad (2.2)$$

For a given pair of elastic solids the adhesion energy γ is fixed but according to Equations 2.1 and 2.2, but R , the radius of the solid can be modified to influence pull-off force. Arzt *et al.* argue that most natural hairy systems, including that of the gecko, by virtue of splitting an integral contact into several sub-contacts, effectively increase R and hence the pull-off. If a spherical solid of a large radius R is split into N smaller spheres of radius R_0 each, such

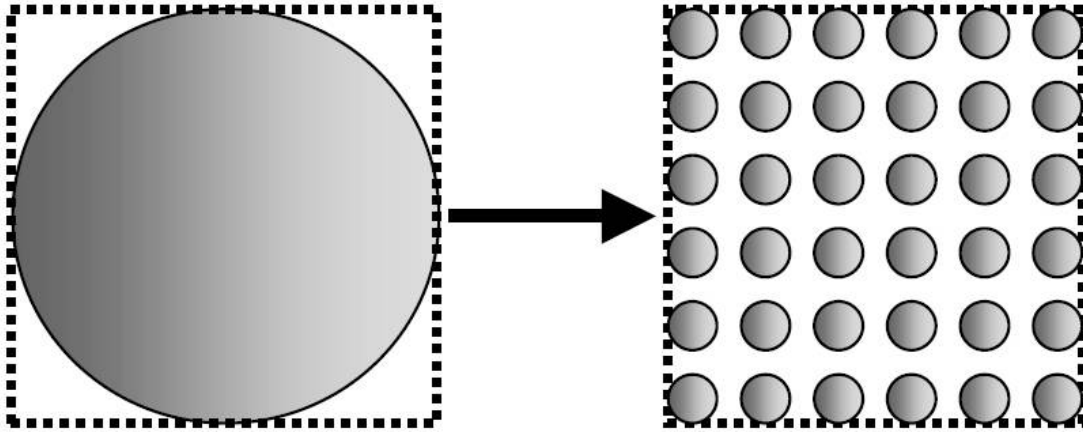


Figure 2.14: Principle of contact splitting. One large contact is split into N smaller sub-contacts with same projected area, [Greiner2007a].

that, $R = \sqrt{N}R_0$ (scaling based on self-similarity of the splits), then the force to pull-off N spherical contacts would be:

$$F_c = \frac{3}{2}\pi\sqrt{N}R_0\gamma. \quad (2.3)$$

The non-adhesive (Hertzian) contact area did not change with the contact splitting, however, the geometrical length of contact increased thereby increasing the force required to pull-off.

2.3.2 Limitations of JKR theory

There are two limitations of application of JKR theory to predict adhesion enhancement by the process of contact splitting. One is the apparent lack of a limit to adhesion enhancement

predicted by an endless contact splitting. When sub-contacts are small spheres, the ratio of the contact radius a of each sphere to its radius R_0 , a/R_0 rapidly increases as the sub-contacts become smaller. Saturation of adhesion enhancement is already reached below the JKR prediction (Eq. 2.3) for a critical size given by γ/σ_0 , where σ_0 is the theoretical van der Waals strength [Gao2005]. The critical size is the effective range of van der Waals interaction, which for a spherical tip shape is a few atomic spacings wide. Hence pure spherical contact shape or a hemispherical tip is a poor shape [Gao2005], [Gao2004]. Instead, as seen often encountered in nature, the end shape of the contacts is flat. Modifying the contact shape to improve interface coverage is considered ahead, see Section 2.3.3.

Second limitation of Eq. 2.3 is the assumption that each of the N sub-contacts pulls off simultaneously. For all the sub-contacts to break off simultaneously the pull-off force should be distributed uniformly across all of them. However, this is hardly ever achieved in practice, especially given the directional nature of peel-off during an adhesive detachment, such as in the gecko adhesive. Compared to a single contact by an integral solid surface, any fibrillar surface splits the contact formation as well as deformation processes into multiple events in time. For the pull-off force to be equally distributed over all sub-contacts a strict control on the dimensions and the compliance of the entire adhesive pad is required [Federle2006]. Federle [Federle2006] estimates that equal load sharing might be possible for very small adhesive pads, if the fibrils are very compliant and if the structures from which the fibrils emerge are very stiff. The pull-off under directional loading or unequal load-sharing is examined using mechanics of contact fracture, Section 2.3.3.

These limits to the JKR predictions reduce the pull-off force only slightly from that predicted by Eq. 2.3. In summary, the main advantage of adhesion enhancement by splitting a contact remains valid [Kamperman2010].

2.3.3 Contact adaptability

2.3.3.1 Geometry of a sub-contact

An important consequence of the surface structuring into fine sub-contacts is the lowering of the effective modulus of the contact. This consequently enhances contact adaptability and adhesion as shown by the following consideration. Consider an adhesive pad of area A containing N sub-contacts (fibrils) each in the form of a cylinder of length h and diameter d made of a material of bulk modulus E will have an effective modulus of [Persson2003]:

$$E_{eff} = CE \frac{Nd^2}{16a \left(\frac{h}{d}\right)^2}, \quad (2.4)$$

where C is a number which depends on the shape of the fibril (typically of order 10) and a is the fibril radius. Accordingly, the estimated E_{eff} of the gecko adhesive, made of the bulk protein β -keratin ($E \approx 2\text{-}4$ GPa), is of the order of 100 kPa [Autumn2006a]. Such compliant fibrils conform to a given surface of arbitrary roughness without large investment of strain energy, Figure 2.15 (a) [Jagota2002], [Persson2003]. Persson and Gorb identify the elastic strain energy as an important driver for detachment from a surface. They conclude that longer, more slender fibrils by stretching elastically prolong the peel process during detachment [Persson2003a], [Persson2003].

The aspect ratio (AR) is the ratio of fibril's height, h to its diameter, d , which according to Equation, 2.4 is a direct measure of a fibril's compliance. Hence, aspect ratio of a sub-contact affects adhesion performance of fibrillar adhesives. This is relevant to the present study where fibril AR was changed to investigate adhesion switching behaviour.

Another argument made in favor of structuring a surface for adhesion enhancement is based on fracture of the interface. Figure 2.15 (b) shows the unloading of fibrillar structure against uneven surface and detachment of fibrillar interface via crack propagation. The energy invested in peeling an adhesive fibril is spent on the growth dynamics of an unstable crack at the interface [Jagota2011]. Hence, peeling an array of fibrils from a surface requires reinvestment of energy to initiate crack at the interface of each new fibril. In effect, the fibrils are crack arrestors. This makes the effective work of adhesion higher than that for a

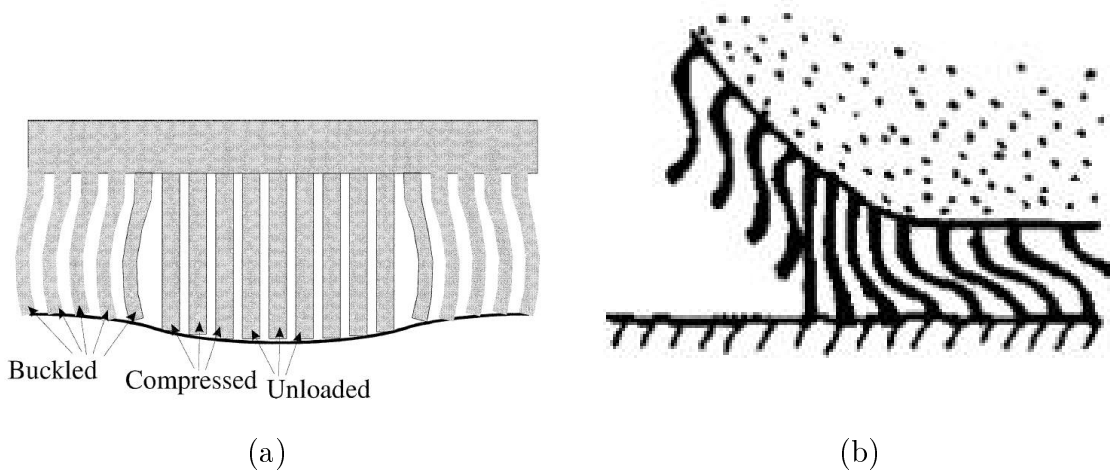


Figure 2.15: Fibrillar surface attachment and detachment. (a) Fibrillar surface adapts to arbitrary rough surface without large deformations [Jagota2002] and (b) long fibrils stretch and have increased surface interaction prior to contact rupture [Persson2003].

continuous solid where a crack once initiated can grow more easily.

2.3.3.2 End-shape of a sub-contact

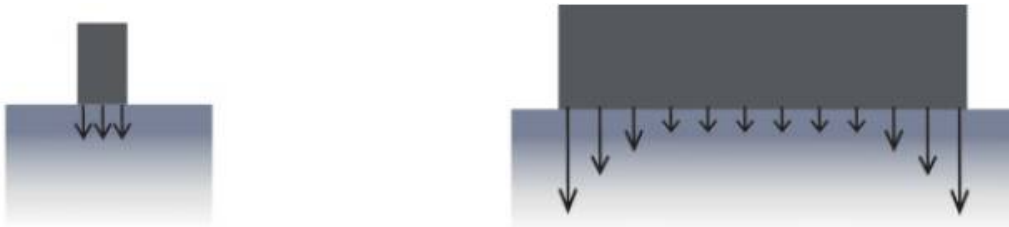


Figure 2.16: Uniform stress distribution in a contact of smaller size results in maximizing adhesion strength, [Kamperman2010].

Gao and Yao [Gao2004] show that the reduction of contact size for a fibril below a critical size will result in uniform stress distribution, Figure 2.16. Only when the stress at the interface is uniformly distributed is it possible to attain the maximum possible theoretical adhesion between the surfaces. Continuous splitting of a spherical end shape of a contact into self-similar sub-contacts may not be ideal [Gao2005]. For a given material stiffness, *e.g.* $E \approx 2\text{-}4$ GPa as in the gecko adhesive, Gao and co-workers [Gao2005] show that only when the subcontacts are a few atomic spacing wide, would it be possible for the solid

to realize its maximum theoretical adhesion strength. Practically, such a contact cannot be fabricated. The basic stress distribution of a curved profile is that of tensile stress at the edge and compressive stress at the center, which delays reaching the uniform stress distribution criterion until the sub-contact reaches the length scale of few atomic spacings.

Natural animal attachment systems, however, are not generally spherical but replete with specialized terminal shapes that tend to generate uniform stress at the interface. Consider the examples of a flat spatula shape with a size of a few hundred nanometers in the gecko, or the mushroom-like flexible discs at the ends of tubes in sea-stars. These are paragons of optimal contact shapes. Many researchers have shown that these shapes adapt to a given surface roughness or defect on surface far better than a spherical or other similar contact shapes, for example Sitti and co-workers [Kim2006], [Kim2009a], Gorb and co-workers [Gorb2007], [Varenberg2008], and Arzt and co-workers [delCampo2007], [Greiner2007], [Spuskanyuk2008].

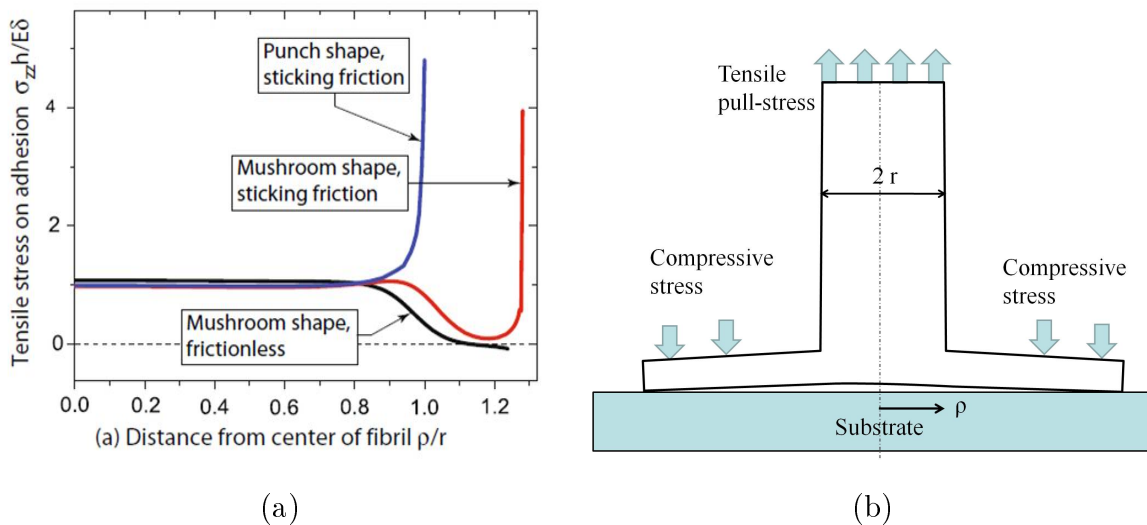


Figure 2.17: Stress distribution at pull-off of mushroom fibril. (a) Stress distribution for pull-off of a mushroom shaped fibril in comparison to punch shaped fibril [Spuskanyuk2008]. (b) Simplified stress scheme for a mushroom shape fibril under tensile pull.

Figure 2.17 shows the stress distribution at pull-off for a mushroom shaped fibril. It is understood by following the reasoning due to Hui *et al.* [Hui2004] and McMeeking *et al.* [McMeeking2008] based on the edge of the contact as the sight of crack initiation.

Spuskanyuk *et al.* [Spuskanyuk2008] extended it specific to the mushroom shape. The flanges or the end-flaps in the mushroom shape act as areas of low stress during pull-off as shown in the stress distribution profiles, Figure 2.17 (a). Any defect present at the edge of the contact area of a non-mushroom shape fibril (in Figure 2.17 (a), punch shape) is detrimental. This is due to the fact that during pull-off the the edge supports significant tensile stresses, being the site where failure initiates. Such a defect at the edge of the flap is much less detrimental due to the compressive stress distribution around the flange edges consequent to the tensile pull on the fibril shaft [Spuskanyuk2008], Figure 2.17 (b). Hence mushroom shape ends of fibrils not only help in enhancing adhesion strength but also make fibrils tolerant to minor defects. In the present work the relevance of a terminal contact shape similar to a mushroom contact shape is investigated in context of an adhesion switch.

2.4 Contact mechanics: switchability in adhesion

2.4.1 Interface contact length: macroscopic view

A reduction in geometrical length of contact affects adhesion adversely according to the JKR theory. A gecko implements such a contact area change by a spring like detachment of adhesive structures during the orientation change of the adhesive pad. Maximizing or minimizing the interface contact length, in turn maximizes or minimizes the resultant adhesion between two surfaces. Synthetic systems have also used this principle. This section explores previous studies which have observed mechanical instability induced change in fibril orientation during adhesion tests. Micropillars having cylindrical or rectangular cross-section with or without modified tips are the most commonly employed fibril geometries used in bioinspired adhesives, *e.g.* see [Greiner2007], [Glassmaker2004] and many others see [Kamperman2010]. Peressadko and Gorb [Peressadko2004] noted that change in the fibril contact from the tip to the side which was generated by excessive compressive loading of fibrils, results in adhesion drop, Figure 2.18 (a). They proposed fibril buckling as a possible reason for the drastic contact change. Commenting on the observed loss in adhesion Persson and co-

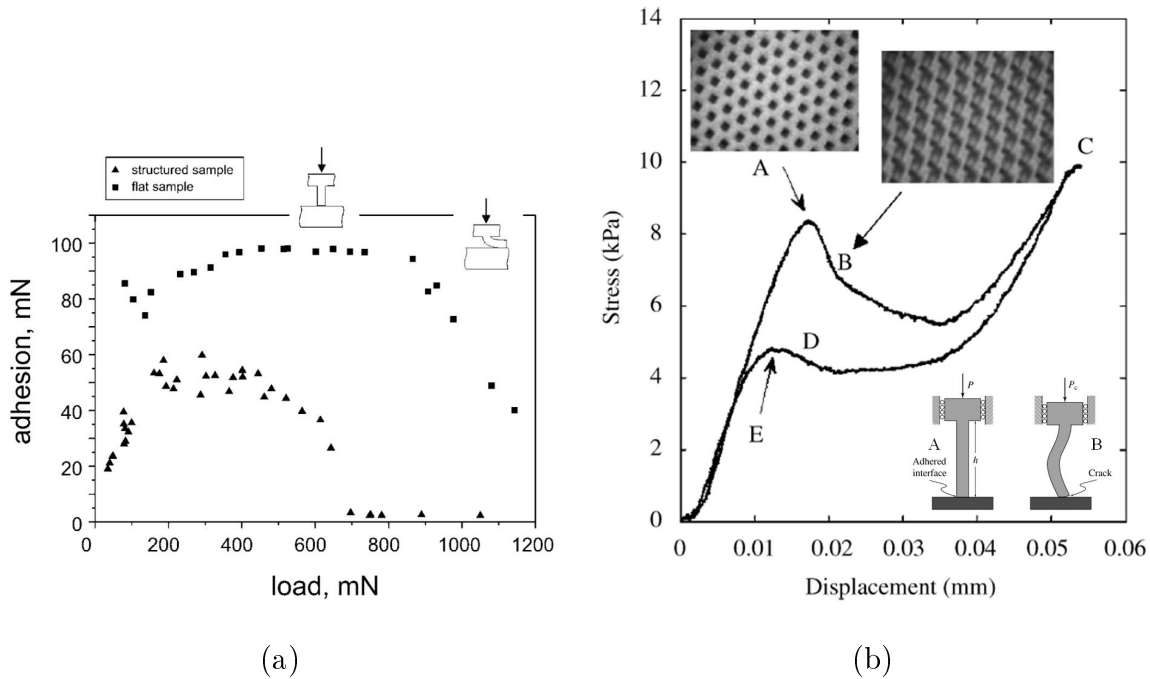


Figure 2.18: Mechanical pressure induced contact area change in fibrillar arrays. (a) Drop in adhesion at high preloads observed by Peressadko and Gorb [Peressadko2004]. (b) Reduction in area and compliance of fibrillar arrays initiated by buckling [Hui2007].

workers [Persson2005] put forth the elastic energy release argument. When the applied load was reversed, the stored elastic energy in the fibrils was returned back, causing the interface between the fibril and the test surface to decohere. It is noted that this result could be specific to their test-device and may not be universally applicable. When interface decohesion was performed keeping an equilibrium between the recovering fibrils whose elastic energy was accommodated by a spring (test surface), the elastic energy release argument fails to explain the observed adhesion recovery. The general message of drastic reduction in contact area being the cause of adhesion loss, however, remains valid .

Hui *et al.* [Hui2007] observed a concurrent drop in stiffness of the fibrillar adhesive to the contact area change from top to side, Figure 2.18 (a). They explained the loss of contact on the basis of fibril buckling, Figure 2.18 (b). Under applied compressive stress, at a critical stress, the fibrils buckle, which opens the interface by breaking the adhesion with the test surface, inset Figure 2.18 (b). Euler buckling theory was used to predict the buckling load

by Hui and co-workers [Hui2007], [Glassmaker2004], [Nadermann2010],

$$F_{crit} = \frac{n^2 \pi^2 EI}{h^2} \quad (2.5)$$

where E is the Young's modulus of the fibril, I is the second moment of area, $I = (\pi d^4/64)$ for a circular cross-section with diameter d , and h is the length of the pillar. The pre-factor, n is the half-wavelength of the buckled shape and takes different values depending on the end constraints on the fibril, Figure 2.19. Such fibril buckling was shown to be detrimental to adhesion [Hui2007].

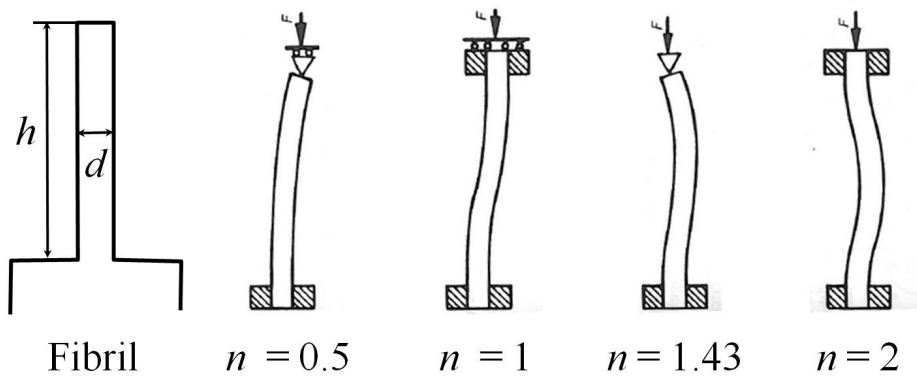


Figure 2.19: Schematic of a fibril on backing (left). Pre-factor n (Equation 2.5) takes different values in accordance to the different end-constraints imposed on fibril ([Ashby2000]).

Inducing such a mechanical instability controllably and using it to gain reversible adhesion is the focus of the present work.

2.4.2 Interface contact length: microscopic view

Maximizing or minimizing the macroscopic interface contact length may not necessarily imply a corresponding change at the microscopic contact points in the normal direction within the interface. The JKR theory predicts that the attractive surfaces forces will result in a finite deformation in the soft body, resulting in a finite area of contact under zero applied load. The interface of interest for this work is that formed by a soft solid (PDMS fibril, $E \approx$ few hundreds of kPa) and a polished hard surface (steel/glass probe, RMS roughness \approx few

hundreds nm). Owing to the finite values of fibril softness and the surface roughness, within the apparent macroscopic contact, a finite set of contact points will generate a real contact length. A singular detachment of one fibril from the surface consists of several detachments between the real contact points created by the soft fibril bridging the asperities on the rough test surface. A more compliant fibril will bridge more surface asperities enhancing real contact.

What we actually measure as the adhesion, is the energy that is invested (alternatively, the force required) to separate, not just the real contacts themselves, but also the near contact points held together by van der Waals forces.

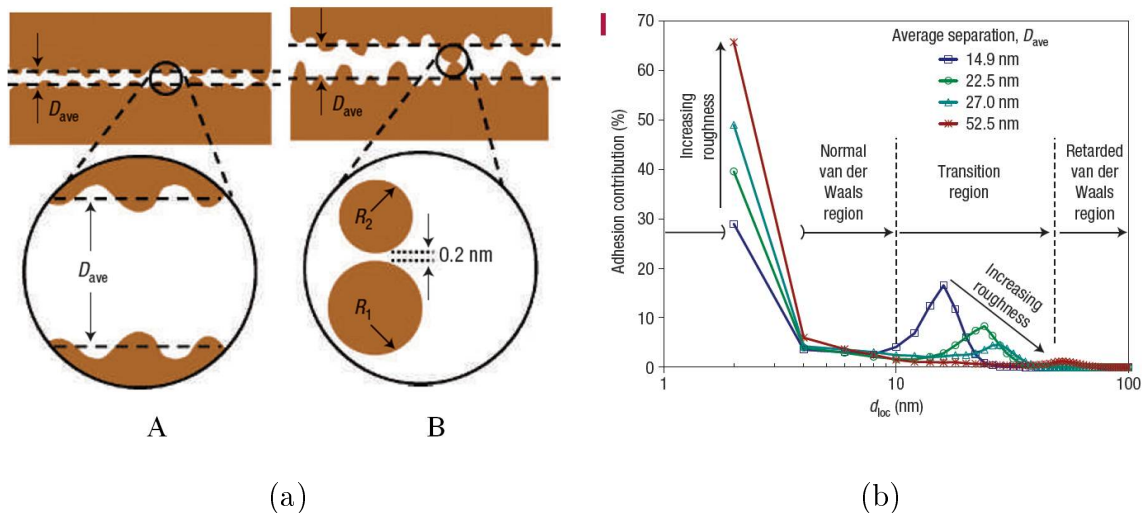


Figure 2.20: Adhesion contributions as a function of local gap (d_{loc}). (a) Two extremes of surface roughness (A) relatively smooth and (B) relatively rough. (b) Adhesion transition from normal to retarded van der Waals region, [Delrio2005].

Intermolecular van der Waals forces are universal in nature. Yet, they are effective over a finite length scale. The extent to which the van der Waals forces affect the measured adhesion is understood with the help of the schematic by Delrio *et al.* [Delrio2005], Figure 2.20 for two micromachined surfaces.

Within a fibril-probe contact, areas where the roughness profile is relatively smooth, the adhesion will be dominated by the contributions from the non-contacting points (A) in Figure 2.20 (a). Whereas, for areas which are relatively rough, the adhesion from the areas which are near the few asperities that nearly bridge the gap will dominate adhesion. The

overall contributions to adhesion change accordingly within an interface. For smooth areas adhesion is dominated by normal van der Waals forces, while for the rough areas it is dominated by the retarded van der Waals forces.

Normal van der Waals forces scale as $(1/r^6)$, r is molecule radius). They are a result of the interactions between temporary dipoles of two neighbouring molecules. For distances larger than the wave-spectrum of these molecules, the forces decay slightly and scale as $(1/r^7)$ known as the retarded van der Waals or Casimir forces. The adhesion contribution transitions gradually from normal to retarded van der Waals forces with the increase in the gap between the two surfaces, see Figure 2.20 (b). The qualitative picture of decay of adhesion contributions within small separation distances ($d_{loc} \approx 100$ nm) helps us understand why an "intimate" contact between two surfaces is necessary to generate any adhesion, at all.

An additional note on humidity induced adhesion enhancement is also needed. Generally, in the controlled conditions of the laboratory, the ambient humidity is 40-45%. It can effectively increase adhesion of a fibril on a glass surface as shown by Arzt and co-workers [Huber2005]. Condensed vapor forming monolayers of water at the interface may result in increased adhesion. Water bridges the gaps by pulling the non-contacted regions within an intimate dry contact. Attraction due to capillary forces scale with $1/(d_{loc})^{1/2}$ and directly with the length of the contact and is much stronger than van der Waals forces [Maboudian2004].

2.5 Summary

- Current literature on switchable adhesive systems was reviewed. Structuring of polymeric surfaces or introducing sub-surface patterns appears to enhance their adhesion. Depending on the specific material-property and adhesive-structure combination, an external stimulus such as temperature, pressure, magnetic field or shear displacement may be selected. These stimuli induced a drastic change in the surface contact area of an adhesive, often reversibly, to generate switchable adhesion.
- Gecko adhesion system was studied to understand its enhanced adhesion as well as

reversibility in adhesion. The surface hierarchical structure of the gecko toe-pad was responsible for the unique dry adhesion produced by maximization of the intermolecular van der Waals forces. Simple orientation change in the adhesive structures resulted in a reversible peel-off from the contacting surface.

- JKR theory was used to understand the advantages offered by structuring a surface into sub-structures or contact-splitting. It predicts an enhanced adhesion for a structured surface on the basis of an increased effective length of contact. Fracture mechanics of opening of an interface by a crack (*e.g.* due to an edge of a contact) additionally supports the contact splitting argument on the basis of multiple fracture sites of sub-contacts.
- Contact shape modification can be used to further influence the crack dynamics during an interfacial fracture. A superior stress distribution compared to other end shapes such as a punch at the edges of the mushroom-shape geometry was shown to delay detachment.
- Contact mechanics studies of buckling in fibrils showed that the interface contact breaks because of such a mechanical instability causing a drastic reduction in adhesion.

With this background, we employ variations in fibril tip-shape, contact radius, aspect ratio and alignment to study the mechanical instability induced change of contact area in the switchable adhesion systems developed in this work.

Chapter 3

Experimental: sample fabrication and test methodology

Abstract

The low stiffness of polymers along with easy processability into fibrillar or other adhesive surface architectures qualify polymers as the material of choice. Photolithography patterning and replica molding were employed to structure polymer surfaces for fabrication of bioinspired adhesives. Adhesion was tested on three different custom-built test devices, each offering specific advantages. Contact mechanisms during an adhesion test were visualized in a top view of the fibril-probe contact interface. Additionally, high magnification visualization from the side of the fibril-probe contact was carried out *in situ* using an environmental scanning electron microscope (ESEM).

3.1 Structuring of polymers

3.1.1 Polydimethylsiloxane, PDMS

Polydimethylsiloxane (PDMS) is a rubbery elastomer prepared by mixing a liquid base and a curing agent (commercially: Sylgard™ 184 from Dow Corning Ltd.). The usual mixing ratio is that of 10 parts base to 1 part curing agent. The liquid prepolymer is subsequently

oven cured at temperatures of 60-120°C for an optimal duration (2-14 h). The resulting polymer has the Young's modulus (E) in the range of 1-5 MPa. Using surface structuring, the effective stiffness of PDMS reduces to few hundreds of kPa in the normal direction. Such a compliant fibrillar surface is the synthetic adhesive fabricated for this work.

Both the base and the curing agent contain siloxane ($Si-O-Si$) oligomers with vinyl groups at the end. The elastomeric nature of PDMS depends on the average chain segment length between $Si-CH_2-CH_2-Si$ cross-links on the $Si-O-Si$ backbone. The elastomeric polymer network is a result of cross-linking of very high molecular weight chain molecules. When the network chain vectors are free i.e. not cross-linked, then the fluctuations in them lower the value of the modulus. However, the cross-linked chain vectors are constrained in their fluctuations, being firmly embedded within the network by the cross links [Mark1977]. Hence, increase in the ratio of the curing agent to the base (within limits) leads to more crosslinks, stiffening the elastomer in the cured state. Thus the modulus of PDMS can be tuned within a range of 100's of kPa to 10's of MPa.

Property of PDMS	Fabrication implications	Adhesion implications
Low and tunable modulus ($E \approx 1-5$ MPa).	Ease of structuring and replica molding.	Ease of surface adaptation.
Low and tunable surface energy ($\gamma \approx 20$ mJ/m ²)	Non-sticky release from master and easy surface modification (O_2 plasma, silanes)	Unreactive and non-toxic, retaining clean adhesion.
Liquid pre-polymer	Fills all features on master. High submicron replication fidelity.	Tunable end contact shape.
Thermally stable (up to $T \approx 180^\circ\text{C}$) and low $T_g \approx -150^\circ\text{C}$.	Stable against decomposition and crystallization.	Repeated mechanical usage.

Table 3.1: Properties of PDMS and their influence on fabrication techniques and adhesion.

The mechanical behaviour of bulk PDMS is that of a typical rubber. It can recover tensile strains of at least 40% without viscoelastic deformation [Schneider2008]. Small applied stress, whether in compression [Wang2011] or tension [Schneider2008], results in a linear response. PDMS adhesives used in the course of this work were subjected to low stresses during the adhesion tests. Hence a linear stress response of adhesives was assumed for all analysis purposes. Table 3.1 based on information from [McDonald2002] summarizes the relevance of PDMS as the material choice for structuring biomimetic adhesives.

3.1.2 Photolithography

Conventional photolithography is a way to pattern surfaces. It can be summarized with the help of Madou [Madou2002] as follows: Selective removal of a photo-active polymer (photoresist) layer is carried out using an irradiation source (UV light) and chemical solvents. The pattern imprinted on the resist is dictated by the radiation blocking design on an UV transparent photo-mask. Irradiation through the mask makes the exposed areas of a positive tone resist (or the unexposed areas of a negative tone resist) soluble in a developer solution. The selective dissolution results in the desired 3-D pattern in the resist film.

Photolithography procedures for this work were carried out in a class 100 clean room facility on Saarland University campus at Saarbrücken (<http://www.mitranz.uni-saarland.de>). SU-8 negative tone photoresists were used to obtain 3-D patterns or masters for replica molding. It is a popular choice for a photoresist for fabricating high aspect ratio structures due to its high stiffness ($E \approx 5$ GPa) and long term stability [delCampo2007b]. Photo-masks were designed to contain arrays of hexagonally packed circles or single circles. These patterns were transferred into 3-D arrays of either cylindrical holes and pillars or single isolated cylindrical holes in the SU-8 master. The usual area covered by the patterns was $\approx 8 \times 8$ cm^2 . The depth of the holes (or in case of pillars their heights) in SU-8 were governed by the SU-8 film thickness.

3.1.2.1 Spin coating

The first step in photolithography involved surface preparation of Si wafers, which act as substrates for SU-8 films. Surfaces of silicon wafers (100 orientation, Crystec Berlin, Germany) were cleaned with acetone in an ultrasonic bath. This was followed by oxygen plasma cleaning (55% oxygen, 600 Watt), which volatilized any organic impurities on the surface of the wafer. Finally, a dehydration bake at $T = 150$ °C removed any residual water from the wafer surfaces. SU-8 resists were subsequently spin coated on clean Si wafers using a

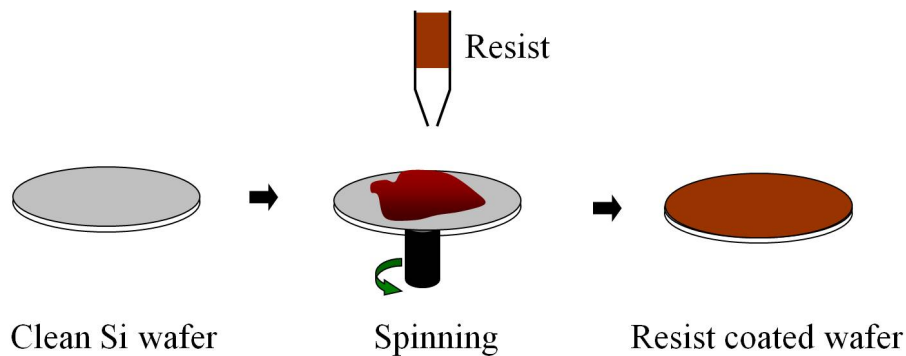


Figure 3.1: Process of spin coating

spin coater (Suss Microtech, Germany). Spin coating parameters listed in Table 3.2 were optimized using calibration spin-curves.

Photo-resist	Spin speed	Thickness
SU-8 2010	1000 rpm	$20 \pm 1\mu\text{m}$
SU-8 2025	3000 rpm	$30 \pm 3\mu\text{m}$

Table 3.2: Spin coating parameters and resulting film thicknesses for SU-8 photoresists.

3.1.2.2 Thin film processing

The standard photolithography processes to structure thin SU-8 films are illustrated in the schematic in Figure 3.2. They are: Soft bake, UV exposure, post-exposure bake and developing. The process details for the different lithography steps are listed in Table 3.3.

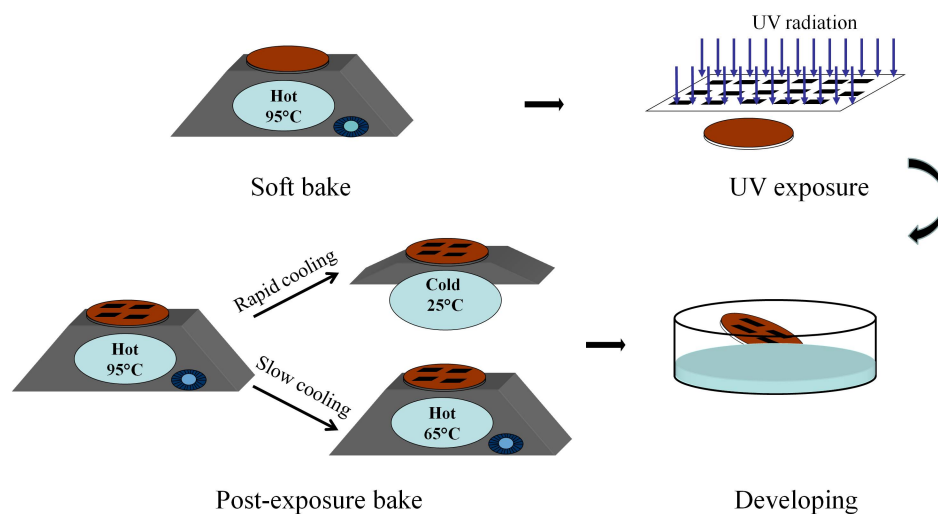


Figure 3.2: Photolithography process scheme

Subsequent to the post-exposure bake, the wafers with resist pattern were either cooled rapidly or slowly depending on the end requirement. Stresses are generated due to the mismatch of coefficients of thermal expansion (CTE) between the resist and substrate. Rapid cooling amplified the stresses in the resist film, whereas the stresses were minimal when SU-8 films were cooled slowly. Slow cooling from 95°C was followed to temperatures below the cross-linking temperatures ($T \approx 65^\circ\text{C}$). The intentional amplification of stresses was used to control terminal shapes of the fibrils (for a detailed description see Chapter 6, Section 6.2.1). The SU-8 masters were obtained at the end of development step. The final step consisted of a hard-bake of the SU-8 masters at 150°C for 30 min. The fully hardened SU-8 masters retained a long term stability outside clean room conditions.

3.1.3 Silanization procedure

PDMS may stick and bond chemically to the SU-8 masters. This can be avoided by coating a monolayer of silane on the SU-8 masters. Silanization of SU-8 masters over the gas phase was done using a mixture of 20 μL of perfluorinating agent in 2 ml of *n*-Hexane in a vacuum desiccator for 30 min. Hexadecafluoro-1,1,12,2-tetrahydrooctyltrichlorosilane (Sigma Aldrich, Germany) was used with 96% purity *n*-Hexane (Sigma Aldrich, Germany). Subse-

Process step	SU-8 2010	SU-8 2025
Soft bake: leveled hot-plate	5 min at 95 °C	5 min at 95 °C
UV exposure: stepper (Suss Microtech, Germany), lamp intensity $\approx 15 \text{ mW/cm}^2$	13.4-16.6 s	11-19.3 s
Post-exposure bake: leveled hot-plate	5.5 min at 95 °C	5.5 min at 95 °C
Developing in mrDev 600 solution (Micro Resist Technology, Germany)	4-5 min	4-5 min

Table 3.3: Photolithography process details for SU-8 photoresists.

quently the templates were baked at 95 °C in vacuum to stabilize the coating by increasing lateral cross-linking and by reaction with free OH groups at the resist surface with the silane [Greiner2007]. The silanization created a hydrophobic monolayer on the structured SU-8 surface that allowed for the easy removal of the PDMS structures.

3.1.4 Soft molding

Soft molding or replica molding replicates the negative of the pattern in the hard SU-8 masters on to a PDMS surface. Cylindrical holes in SU-8 generate pillars in PDMS. Liquid PDMS was prepared by mixing the prepolymer and cross-linker from the Sylgard 184 kit (Dow Corning MI, USA) in 10:1 ratio. The mixture was degassed to remove air bubbles and subsequently poured to cover the pattern on the silanized SU8 masters. Generally, a reservoir of rapidly curable elastomer TurboFlex™ was created on the surface of the SU-8 master to contain the liquid PDMS. Liquid PDMS was cross-linked at 75 °C for 12 to 14 h under light vacuum, which ensured that all the SU-8 features were covered by PDMS and no air pockets left in SU-8 master. The cured PDMS was carefully peeled manually from the SU-8 master to avoid any damage to the pillar structures and the master.

3.2 Adhesion test methodology

The adhesion performance of the samples was measured using load-displacement tests. A typical load-displacement measurement was generated by applying normal compressive displacement to the adhesive against a probe of defined geometry till a certain predefined maximum in compressive force was reached, referred to as the *preload*. The adhesive was held at the compressive maximum for no longer than was necessary for reversing the mechanical displacement in the testing machine. It was pulled away from the probe in normal tensile displacement until detachment. The maximum tensile force recorded at detachment was taken to be the measure adhesion, referred to as the *pull-off force*. A typical 'Force' versus 'Displacement' plot and the evolution of the 'Force' with 'Time' from an adhesion test on structured PDMS sample are shown in Figure 3.3. .

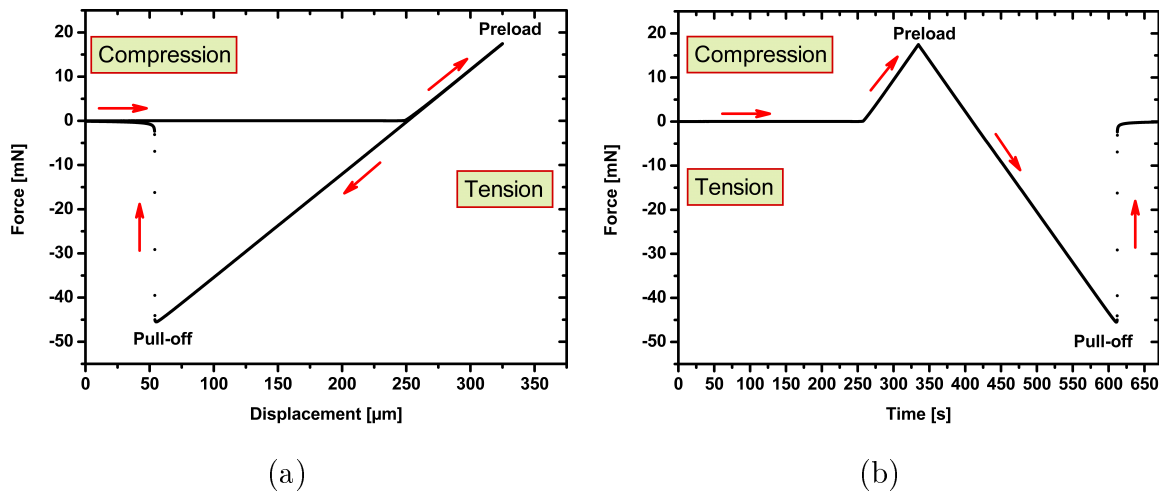


Figure 3.3: Typical adhesion test result. (a) Force-displacement plot and (b) Force-time plot for same sample of structured PDMS tested against flat glass cylinder.

3.2.1 Adhesion test devices

During the course of this work three different custom-built adhesion testing devices were used: (1) *Macroscopic Adhesion testing Device* at the INM-Leibniz Institute for New Materials in Saarbrücken, (2) *Microtack* at the Physico-chimie des Polymères et Milieux Dispersés Sciences et Ingénierie de la Matière Molle (PPMD), École Supérieure de Physique et de

Chimie Industrielles de la Ville de Paris (ESPCI ParisTech), Paris and (3) *Contact Adhesion Testing Device* at the Crosby Research group, Polymer Science and Engineering, University of Massachusetts, Amherst, USA.

Although the specifics of motion control, force measurement and optics are different for each of three test devices, the general common principle of a load-displacement test to measure adhesion is followed in all. The applied displacement is controlled in all the three set-ups and the rate of displacement is kept between 0.9 to 10 $\mu\text{m/s}$. In the devices (1) and (3), deflection of a calibrated cantilever was used to deduce forces. This methodology deviates from the ideal displacement control test in the sense that the force sensor is not "infinitely" rigid or fixed, but is a movable spring of known spring constant. The spring is much stiffer than the test structures and the forces measured are comparable to those measured by a rigid force sensor in device (2). The specific working details of these devices are presented, for (1) in Chapter 4 and 6, for (2) in Chapter 4 and for (3) in Chapter 7.

3.2.1.1 *Macroscopic Adhesion testing Device*

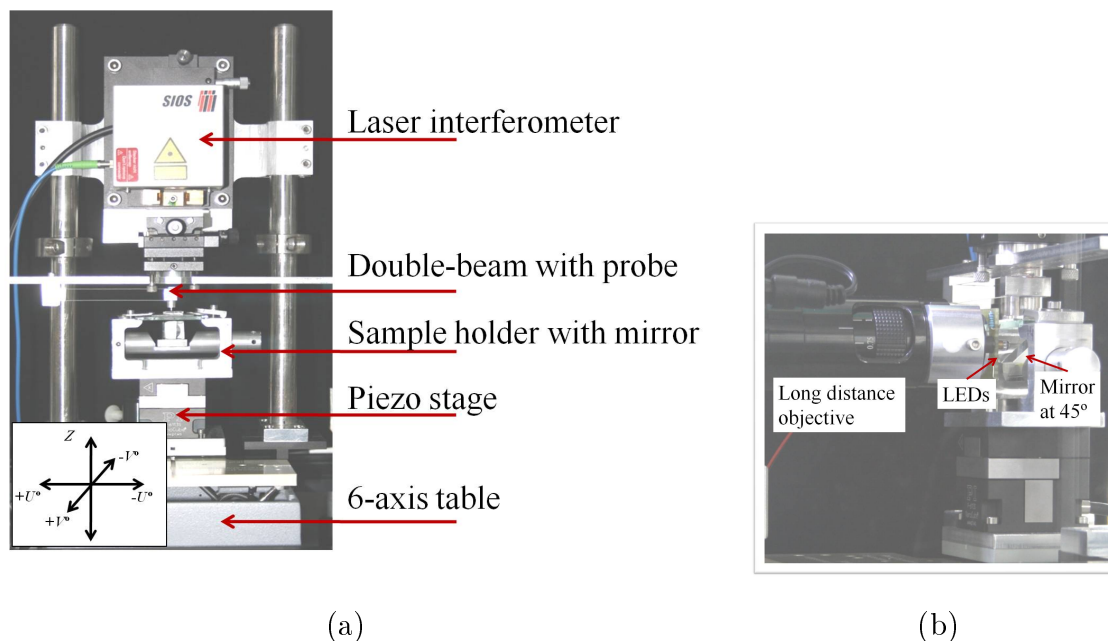


Figure 3.4: (a) Macroscopic Adhesion testing Device [Kroner2012]. (b) Visualization appendage (new custom-addition by J. Blau).

The use of three different testing setups was justified by the specific contact mechanisms investigated. The in house *Macroscopic Adhesion testing Device* due to Kroner et al [Kroner2012] was used most extensively during this work. Extremely sensitive displacement control (in the nanoscale) and the ability to finely control the sample tilt were its main advantages over the other two devices. It also provided a nanoscale force resolution [Kroner2012].

For the present work, the *Macroscopic Adhesion testing Device* was modified to provide contact visualization during an adhesion test. A long distance (60 mm) objective equipped with a camera (The Imaging Source, DMK 31BF03, Germany) was custom fitted. Light emitting diodes were fitted around the rim of the objective to shine light on the 45° tilted mirror. The mirror was located at the bottom of the translucent sample. The objective captured the reflected light from the mirror giving information of the contact interface (Figure 3.4 (b)). However, it failed at providing a high resolution needed to examine the specific contact mechanisms due to a mechanical instability (optical magnification $\leq 2.5x$). Visualization was important for the present work and hence other devices were sought.

3.2.1.2 *Microtack*

Microtack (setup (2)) due to Josse *et al.* [Josse2004] was sought for its ability to present an optically magnified view (up to 100x) of the contact interface. The configurational changes in the fibrils during an adhesion test were closely followed by visualizing the fibril-probe contact interface, Figure 3.5. However, the *microtack* lacked did not provide any control on the tilt of the sample with respect to the probe. Additionally, the force resolution was limited to few millinewtons (mN).

3.2.1.3 *Contact Adhesion Testing device*

Contact Adhesion Testing device due to Crosby *et al.* [Crosby2005] was especially interesting for the ability to resolve low forces (μNs) in combination with a high resolution contact information. This was required for tests on single micropillars. An inverted microscope helped in visualizing the fibril-probe contact mechanisms specific to buckling of a fibril,

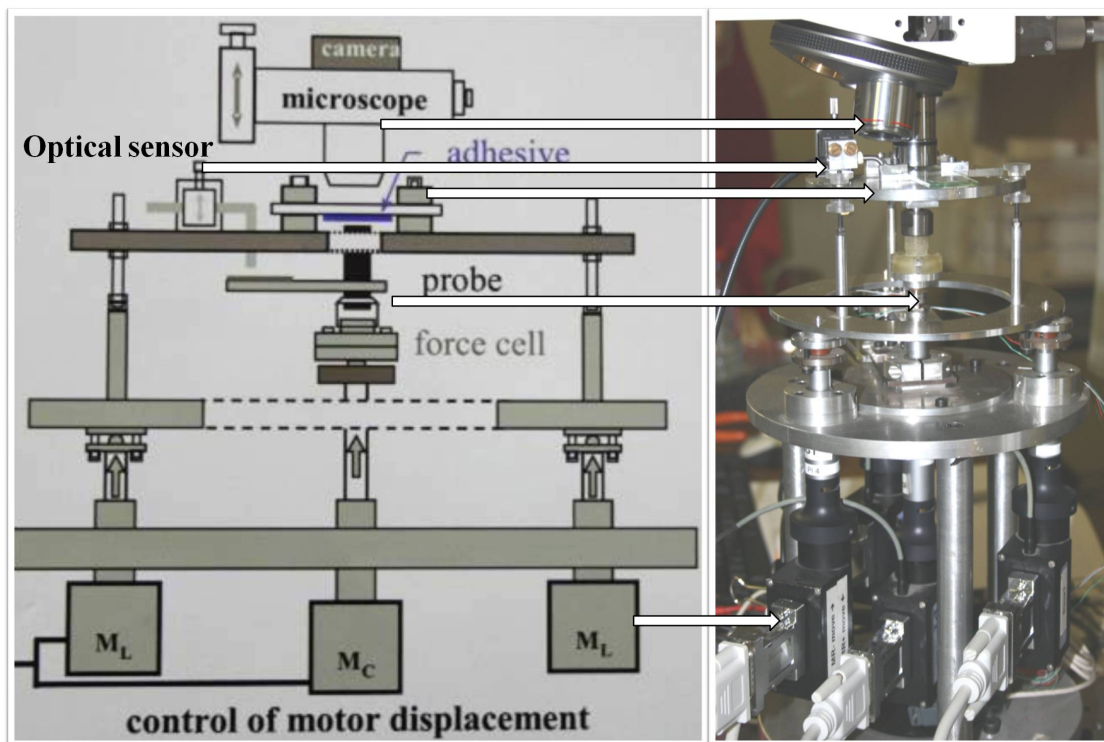


Figure 3.5: Schematic and photograph of Microtack with labeled components [Josse2004].

Figure 3.5.

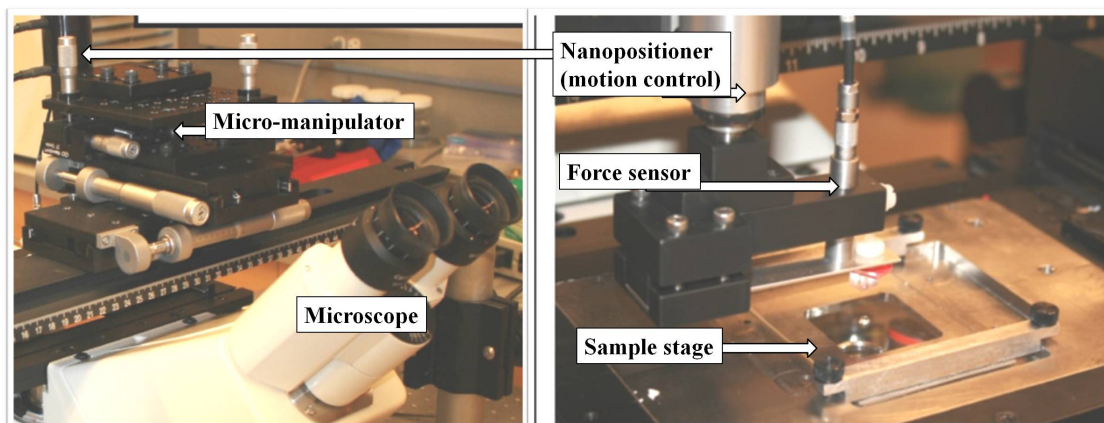


Figure 3.6: Contact Adhesion Testing Device with labeled components [Crosby2005] (image courtesy C. Davis).

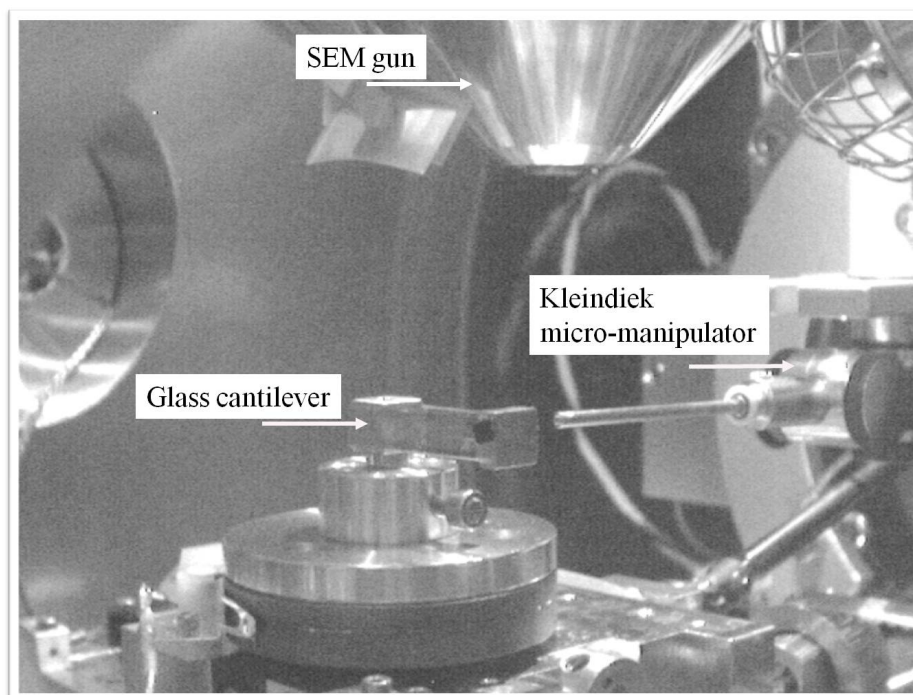


Figure 3.7: Custom built adhesion test set-up inside ESEM, (image courtesy A. S. Schneider).

3.2.1.4 ESEM *in situ* test device

In all the above test devices, *in situ* visualization of the contact interface was a key experimental tool. However, only a top-view impression of the fibril-probe contact interface could be generated. This limitation was overcome by the high magnification *in situ* visualization from the side, provided by an environmental scanning electron microscope (ESEM), FEI Quanta 400 F. The ESEM offered an important advantage of visualizing a polymeric sample without the need for gold coating. Using the low-pressure mode (100 kPa) instead of the conventional high vacuum mode, the adhesive samples were tested in their virgin state. Adhesion testing inside the ESEM was carried out by appending it with a micromanipulator (Kleindiek Nanotechnik GmbH, Germany) and a custom built glass cantilever (Figure 3.7). The study employed for the first time an *in-situ* method in an ESEM to investigate the details of contact formation and separation (Chapter 5).

3.3 Typical results

An overview of typical fibrillar structures on polymeric surfaces fabricated using photolithography and replica molding is presented here. The details and special features of most of these structures are presented in conjunction to their adhesion performance throughout this thesis. Figure 3.8 shows different aspect ratio cylindrical PDMS fibrils having rounded edges and flat tops (for fabrication details see Chapter 6, Section 6.2.2).

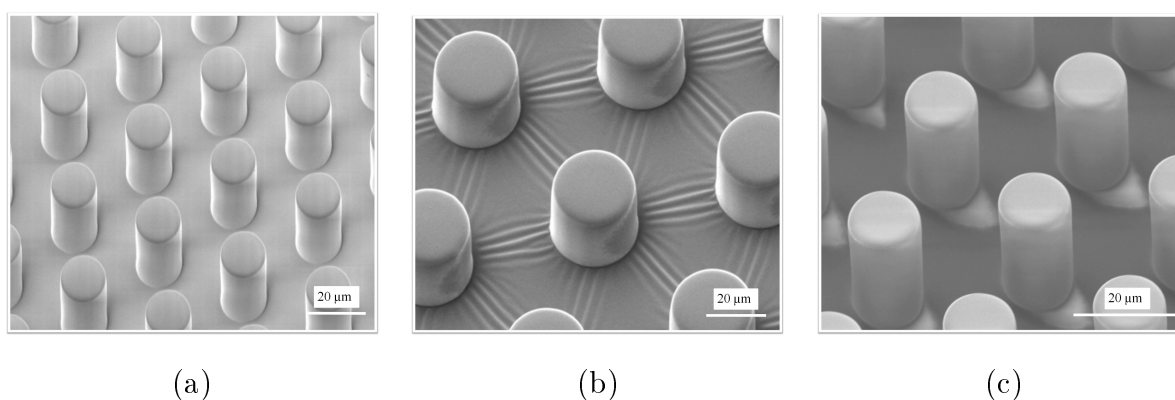


Figure 3.8: Typical rounded edged PDMS cylindrical fibrils with flat tops.

Figure 3.9 (a) and (b) show different aspect ratio cylindrical PDMS fibrils having terminal flaps (end-flaps) and flat tops (for fabrication details see Chapter 6, Section 6.2.1). Similar contact shapes can also be generated in other polymers such as the shape memory polymer Tecoflex™ 72 D (Figure 3.9 (c)).

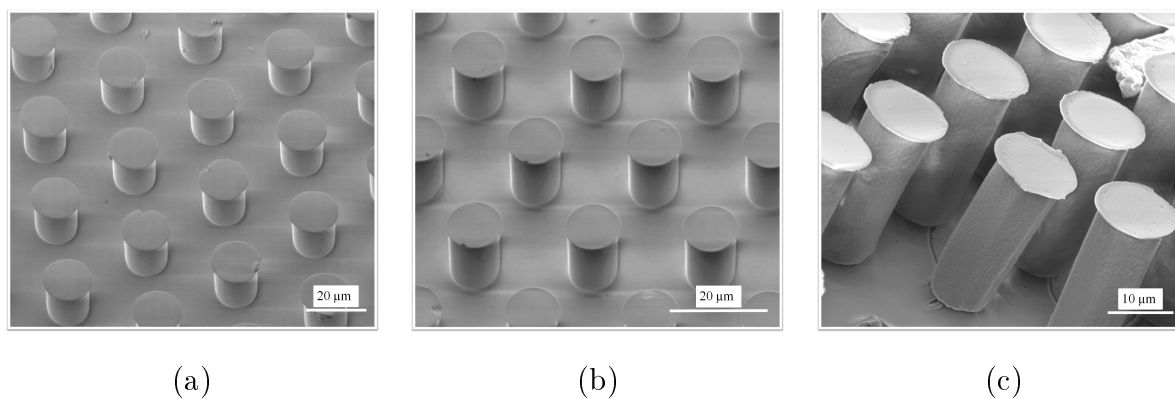


Figure 3.9: Typical end-flap terminated cylindrical fibrils with flat tops.

Figure 3.10 shows that the processing capability is not limited only to PDMS or to vertical structures. Hybrid metal-polymer structures were fabricated using thin-film side-deposition, Figure 3.10 (a) (for fabrication details see [Trejore2010]). Surface of Tecoflex™ 72 D was structured with mushroom shaped and hollow fibrils using replica molding from SU-8 masters. Additionally, tilted structures were produced by inducing mechanical shear in the softened state when heated above the glass transition temperature, Figure 3.10 (b) and (c) (for fabrication details see Appendix I).

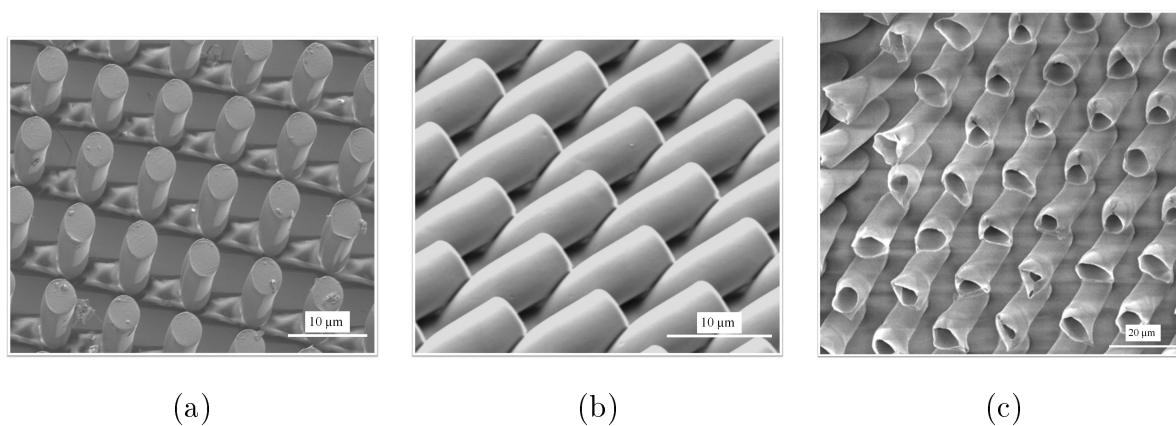


Figure 3.10: (a) Hybrid metal-PMDS fibrillar adhesive bent due to mismatch in deposition stresses. Solvent induced (b) shear or (b) hollowness in cylindrical fibrils of Tecoflex™ 72 D.

Chapter 4

Bioinspired pressure actuated adhesive system¹

Abstract

A dry synthetic adhesive system inspired by gecko feet adhesion was developed. It can switch reversibly from adhesion to non-adhesion with applied pressure as external stimulus. Micropatterned polydimethylsiloxane (PDMS) surfaces with pillars of 30 μm length and 10 μm diameter were fabricated using photolithography and molding. Adhesion properties were determined with a flat probe as a function of preload. For low and moderate applied compressive preloads, measured adhesion was 7.5 times greater than on flat controls whereas for high applied preloads adhesion dropped to very low values. *In situ* imaging shows that the increased preload caused the pillars to deform by bending and/or buckling and to lose their adhesive contact. The elasticity of PDMS aids the pillar recovery to the upright position upon removal of preload enabling repeatability of the switch.

¹This chapter was published as a full paper [Paretkar2011]

4.1 Introduction

Nature offers multitudes of structures in different plants and animals, the functionalities of which have inspired scientists to the design of advanced material systems. Actuation based on change of structural configuration in response to external stimuli has often been intriguing. For example, the intricate structure of the plant cell wall in pine and spruce cones is responsible for differential swelling of different parts of the tissue in response to changing humidity levels which results in a slow opening and closing of pine cones [Fratzl2009]. Similarly, wheat awns attached to seeds can penetrate the soil by bending reversibly thus depositing seeds in ground [Fratzl2009]. These functionalities do not involve any metabolic activities on behalf of the plant or animal thus opening the gates for mimicking these structures with the help of synthetic materials and fabrication routes. Another example is the microstructure based adhesive system of the gecko foot [Autumn2000]. The multi-scale hierarchy of the gecko foot has been extensively examined and the resulting adhesion has been attributed to van der Waals forces [Autumn2002] and capillary forces [Huber2005].

Previous work has demonstrated that splitting of a contact into several small microscale contacts by a pillar microstructure is at the heart of strong gecko adhesion [Arzt2002], [Arzt2003]. The micropillars facilitate intimate contact formation with surfaces of any roughness giving rise to strong adhesion. These observations have led the way in designing pillar surface microstructures and fabricating synthetic biomimetic adhesives, e.g. [Sitti2003], [Schubert2007], [Greiner2007], [Jeong2009], [Boesel2010], [Nadermann2010a]. As opposed to single contact by an integral solid surface, any pillar surface splits the contact formation as well as deformation into multiple events. The nature of these events in time depends on the geometry and orientation of the pillars, elastic moduli of pillars and probe and roughness of probe. The interplay between these parameters is complex and has been the focus of several studies [Jagota2002], [Persson2003], [Hui2004], [Spolenak2005], [Spuskanyuk2008], [Jagota2007], [Creton2007]. Especially interesting for the present study is the effect of change of applied pressure or preload on the adhesion behaviour of structured surfaces. Greiner *et al.* showed that adhesion initially increases with increasing preload and then plateaus for higher preloads [Greiner2007]. Peressadko and Gorb observed a drop in adhesion for flat as well

as structured polyvinylsiloxane (PVS) pillars at high applied preloads [Peressadko2004]. A recent review by Kamperman *et al.* summarizes the interplay between the design parameters with the following relationships [Kamperman2010]:

1. Adhesion strength of pillar surfaces increases with decreasing pillar radii.
2. For a constant pillar radius the adhesion force increases with increasing aspect ratio.
3. Mushroom-shaped tips for micropillars have so-far shown the best adhesion performance.
4. A second level hierarchy at micro-scale so-far fails to enhance adhesion in spite of theoretical predictions.
5. For thinner backing layers the adhesion performance increases.

The gecko shows rapid attachment and detachment actions (milliseconds) during movements on any surface when following a prey or under threat from predators. Quick detachment from the attached state is inherent to such a motion. The tilted setae, by a simple change of orientation, can peel off easily from a surface [Tian2006], [Zhao2008]. While high adhesion strengths have been obtained for artificial pillar surfaces, it is still a great challenge to mimic the specific gecko biomechanics of strong adhesion and easy release. A first example using a shape memory polymer was developed by Reddy *et al.* [Reddy2007]. It was shown that by changing the orientation of micropillars from their vertical to tilted state results in a significant loss of adhesion. Different external stimuli such as magnetic field, pressure, electric field can be envisioned for actuated adhesion systems. A fully reversible adhesive based on magnetic switching of polymer coated Ni-micropads was demonstrated by Northen *et al.* [Northen2008]. Mechanical stretching as external stimulus was used to tune adhesion of an array of polydimethylsiloxane (PDMS) pillars by orientating the pillars normal to the surface from an originally wrinkled configuration [Jeong2010].

A pressure actuated adhesive system using the loss of intimate contact by change of orientation is presented here. Pressure as an actuation mode for realizing fully reversible adhesion has not been shown before. The adhesive system is composed of PDMS micropillars with

aspect ratio 3 (length 30 μm and diameter 10 μm) fabricated using photolithography and molding. This system shows reversible switching between adhesive and non-adhesive state by applying preload.

4.2 Experimental methods

4.2.1 Fabrication of SU-8 lithographic templates

SU-8 2025 (Micro Resist Technology, Berlin, Germany) was spin coated to thickness of 30 μm on silicon wafers (100 orientation, from Crystec Berlin, Germany). Before spin coating, the silicon wafers were cleaned with acetone in an ultrasonic bath followed by oxygen plasma cleaning, which volatilized any organic impurities on the surface of the wafer. Finally a dehydration bake at $T = 150\text{ }^\circ\text{C}$ removed any residual water from the wafer surface. To obtain SU-8 lithographic templates with holes of aspect ratio 3, the SU-8 film was UV irradiated through a quartz mask having hexagonally packed 10 μm diameter circular chrome spots. A mask aligner (Suss Microtech) was used for the irradiation step. A WG 320 filter was used to cut off wavelengths below 320 nm during irradiation. A summary of the processing parameters of the photolithography process is given in Table 4.1.

4.2.2 Soft molding

PDMS was prepared by mixing the prepolymer and cross-linker from the Sylgard 184 kit (Dow Corning MI, USA) in the standard 10:1 ratio. The mixture was degassed to get a bubble free final structure. SU-8 templates were silanized over the gas phase using perfluorinating agent hexadecafluoro-1,1,12,2-tetrahydrooctyltrichlorosilane for 30 min. in a desiccator to facilitate easy removal of cured PDMS from the holes. Subsequently the templates were baked at 95 $^\circ\text{C}$ in vacuum to stabilize the coating by increasing lateral cross-linking and by reaction with free OH groups at the resist surface [Greiner2007]. Degassed PDMS was poured on the silanized templates and allowed to cure for 12 to 14 h at 75 $^\circ\text{C}$ in light vacuum to ensure all the holes were filled. The cured PDMS was carefully peeled from the SU-8

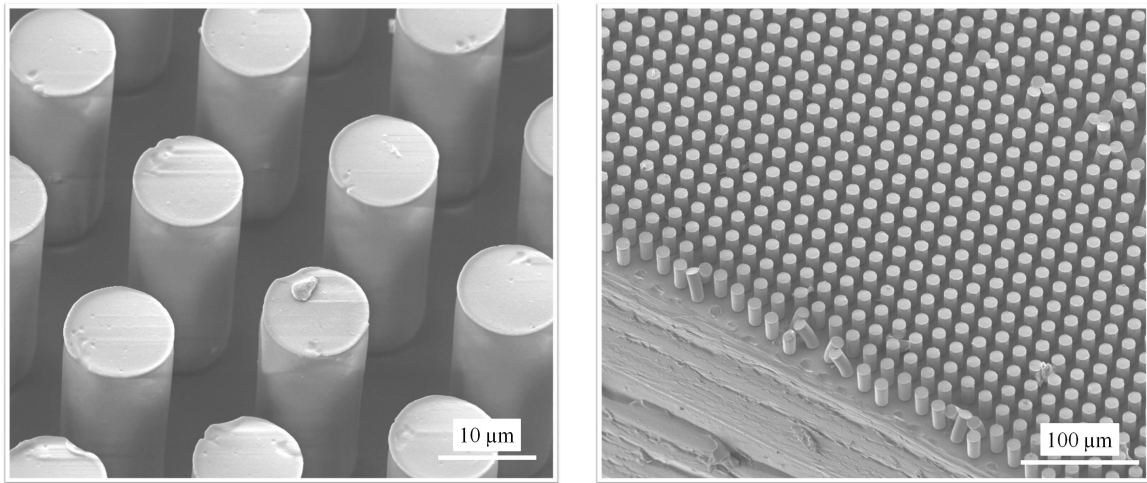
Process	Steps	Temperature [°C]	Time
Si wafer cleaning	Sonication in acetone and isopropanol rinse	Room temperature	5 min.
	O ₂ plasma cleaning (55% oxygen, 600 Watt)		5 min.
Dehydration baking	Clean Si wafer on flat hot plate	150 °C	5 min.
Spin coating SU-8 2025	(a) 500 rpm at 1000 rpm/s	Room temperature	(a) 15 s
	(b) 2000 rpm at 3000 rpm/s		(b) 30 s
Soft baking	SU-8 coated wafer on flat leveled hot plate	95 °C	6 min.
Exposing	Wafer under UV lamp (Hg lamp 15 <i>mW/cm</i> ²)	-	11 s
Post-exposure baking	Wafer on flat leveled hot plate	95 °C	6 min.
Developing	Wafer immersed in mrDev 600 solution	Room temperature	3 min.
Hard baking	Wafer heated in oven	150 °C	30 min.

Table 4.1: Photolithography process parameters

template to avoid any damage to the pillar structures. The arrays of hexagonally packed PDMS micropillars had dimensions of 50×50 mm and had pillars with a length of $30 \mu\text{m}$ and diameter of $10 \mu\text{m}$. The backing layer of PDMS was 1 mm thick.

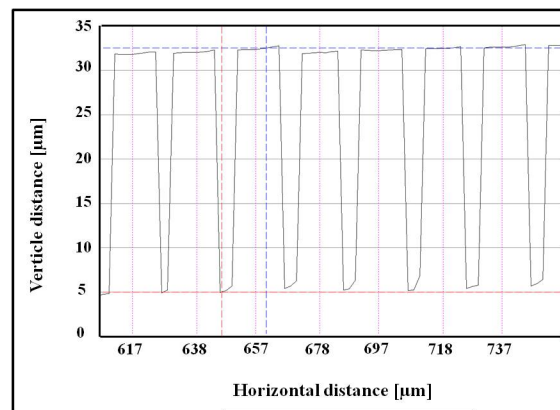
4.2.3 Sample Characterization

The samples were characterized using scanning electron microscopy (SEM) and white light interferometry. SEM images were obtained with an FEI Quanta 400 F operating at an energy of 1-5 keV after sputtering the films with gold. SEM images of a portion of such an array with the accompanying white light interferometry (Microsurf3D, FogaleNanotech) image are shown in Figure 4.1.



(a)

(b)



(c)

Figure 4.1: PDMS microfibrillar array characterization in SEM. (a) Flat top edge for PDMS cylindrical pillars. (b) Arrays of fibrils with defects such as bent or missing pillars (estimated to be below 5 % of total test area). (c) White Light Interferometry profile of micropillars with diameter of 10 μm and height of 30 μm .

Defects such as missing or bent pillars, seen in the micrograph, occur statistically more on the edges of a test sample due to handling and cutting. With the help of optical microscopy (Olympus BX51), the total defect area was estimated to be well below 5% of the test area.

4.2.4 Adhesion measurements

The adhesion performance of the samples was measured by standard load-displacement tests on a custom-built test apparatus *Macroscopic Adhesion testing Device*, Figure 3.4 [Kroner2012]. 6-axis positioning table (F-206 Hexapod, Physik Instrumente Karlsruhe, Germany) was used for generating a nanoscale positional accuracy in the vertical axis as well as a tilting ability with a fine control of 0.01° . The device was placed on a vibration isolation system (TS 150, HWL Scientific Instruments, Germany). The sample, mounted on a glass slide, was loaded against and retracted from a flat probe with circular cross-section ($d = 1$ mm, glass cylinder) at a constant velocity of $1 \mu\text{m/s}$. A laser interferometer (SP 120, SIOS Messtechnik Ilmenau, Germany) positioned vertically above the motion stage read spring deflections. The spring was calibrated prior to the adhesion test using a force sensor (range 0-0.5 N, Althen GmbH, Germany). Measured deflections were converted into forces using the spring stiffness of 247 N/m , (resolution = $1 \mu\text{N}$). LabView™ software was used to control the load-displacement test. Alignment of the flat probe surface and the PDMS sample was achieved using the six-axis positioning system. The sample was scanned for maximum in adhesion values and minimum in the applied preload for a fixed probe indentation depth by tilting along U- and V-axes to get the best alignment. In this way, parallel alignment between the probe and the sample was achieved with an accuracy of 0.01° (see supplementary information in Appendix II, Figure 8.2).

Measurements were also performed with the *Microtack*, Figure 3.5 [Josse2004]. *Microtack* device enabled *in situ* visualization of mechanical deformation of the PDMS micropillar array during adhesion testing. The translucent PDMS sample, mounted on a glass slide was viewed with the help of a long range microscopic lens from the glass slide side i.e. from the back of the sample. The *Microtack* device was a displacement-controlled set-up as opposed to the load-controlled Macroscopic Adhesion testing Device mentioned above. A polished flat steel probe with circular cross-section ($d = 6$ mm) was used to test adhesion. The details of the *Microtack* device can be found in [Josse2004].

The geometry of the adhesion test principle, which is the same for both testers, is schematically depicted in Figure 4.2(a). Also a typical force-displacement curve is displayed which

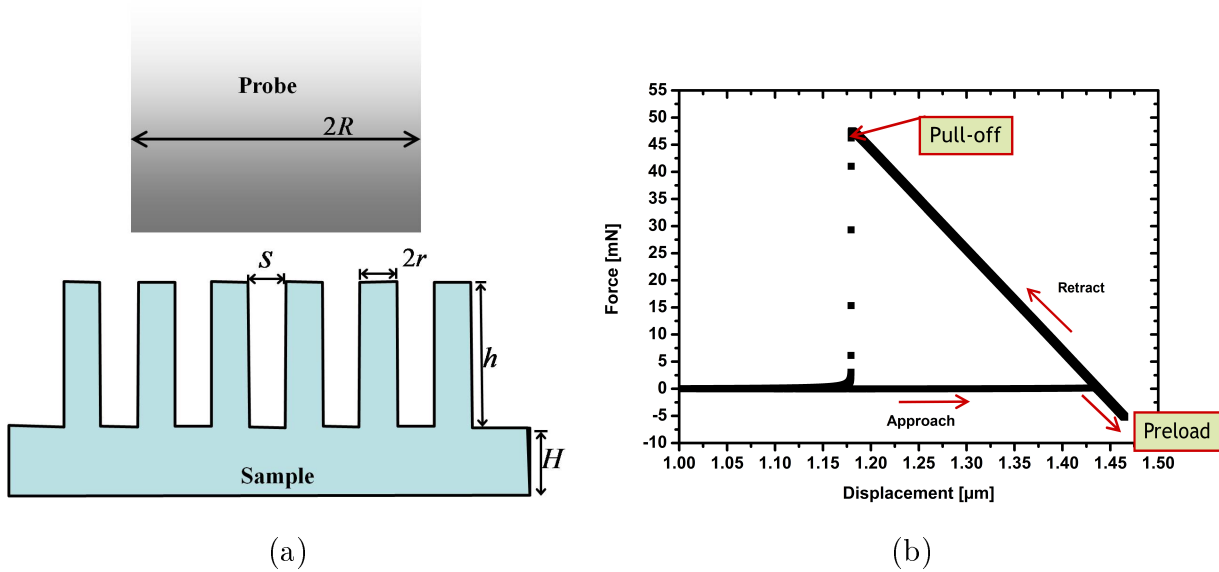


Figure 4.2: Adhesion test. (a) Schematic of adhesion test geometry: R = radius of flat cylindrical glass probe (0.5 mm), r = pillar radius ($5 \mu\text{m}$), S = spacing between pillars ($10 \mu\text{m}$), h = pillar length ($30 \mu\text{m}$), H = thickness of backing layer (1 mm). (b) Typical load-displacement curve obtained from an adhesion test where PDMS pillar array with the above dimensions is tested against a cylindrical probe.

shows the approach, loading and retraction of the sample against the cylindrical probe (Figure 4.2(b)). During approach, the sample is loaded in compression to a defined preload (P_p). The measure of adhesion is the maximum pull-off force (P_c) determined as the probe loses contact with the sample during retraction. The preload-stress and the pull-off strength are calculated by dividing (P_p) and (P_c) with the probe contact area. Additional tests simulating the load-displacement adhesion test were performed using a micromanipulator (Kliendiek Nanotechnik GmbH, Germany) in SEM to obtain *in situ* high resolution pillar deformation images.

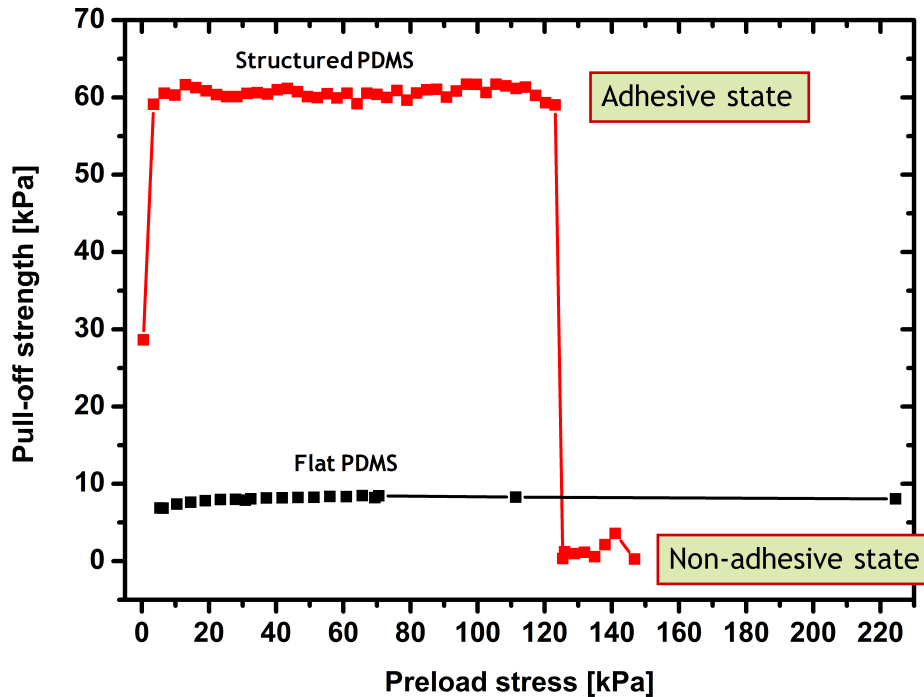


Figure 4.3: Adhesion switch. Dependence of pull-off strength on applied preload stress. Adhesion state with high pull-off strength and non-adhesion state with low pull-off strength can be distinguished.

4.3 Results

4.3.1 Adhesion states and repeatability

Figure 4.3 shows the dependence of pull-off strength on the applied compressive preload stress for structured PDMS as well as for flat controls. Flat controls are blocks of plane PDMS (10:1) with curing conditions and dimensions similar to the structured samples, 10×10 mm and 1 mm thick. Compared to control samples (maximum pull-off strength 8 kPa), the measured pull-off strengths of structured samples were about 7.5 times higher. At extremely low preloads (0.5 kPa), the measured pull-off forces were also low (30 kPa). With an increase in preload (> 3 kPa), the pull-off forces rapidly reached a maximum of 60 kPa. The pull-off strengths were retained at maximum for an intermediate preload range between 3 and 123 kPa, after which a sudden drop to extremely low pull-off strengths (1.2 kPa) was

recorded for high preloads. Thus, two distinct states, that of adhesion (high P_c) and that of non-adhesion (very low P_c) were realized by a change of preload stress.

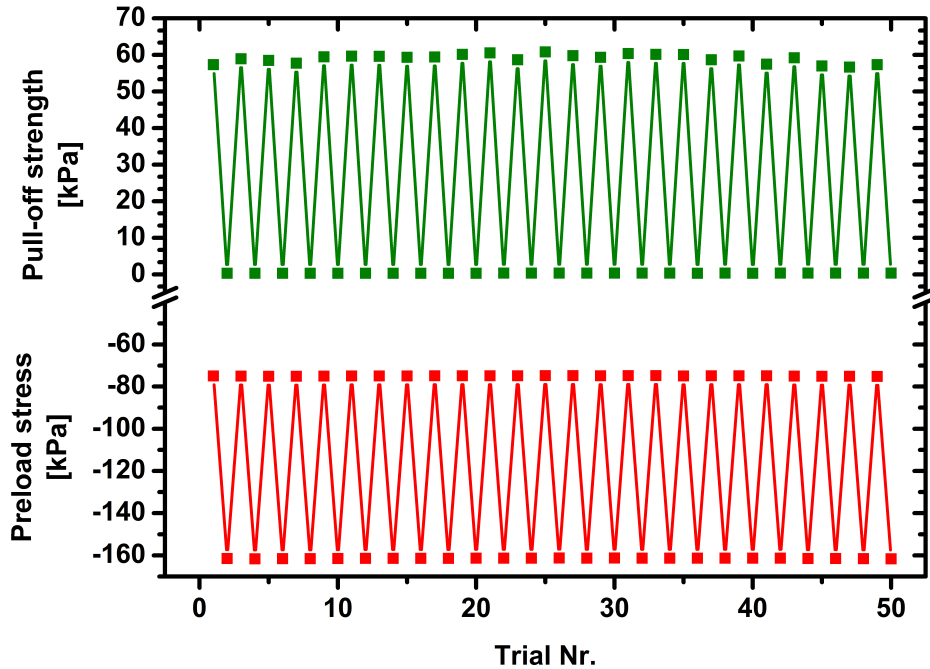


Figure 4.4: Adhesion repeatability. 50 cycles of repeatable adhesion switching between high and low adhesion states.

The repeatability of the actuated system was tested over many cycles using alternating low and high preloads and measuring the resulting adhesion. A selection of 50 cycles is shown in Figure 4.4. Pull-off strengths of 60 kPa for the adhesion state and below 0.5 kPa for the non-adhesion state were recorded. Thus the actuated adhesive system is reversible as well as repeatable over several cycles.

4.3.2 *In situ* video and SEM results

Figure 4.5 shows representative force-time plots during adhesion tests for a moderate applied preload of 0.75 N (26.5 kPa). Contact formation can be observed in the video snapshots (Figure 4.5, insets I-III): light contrast in inset I indicates absence of contact. In II, contact of the pillars left of the superimposed line (dark contrast circles) is seen, while in III full contact is reached. In insets III and IV of Figure 4.5, a small lateral displacement of the

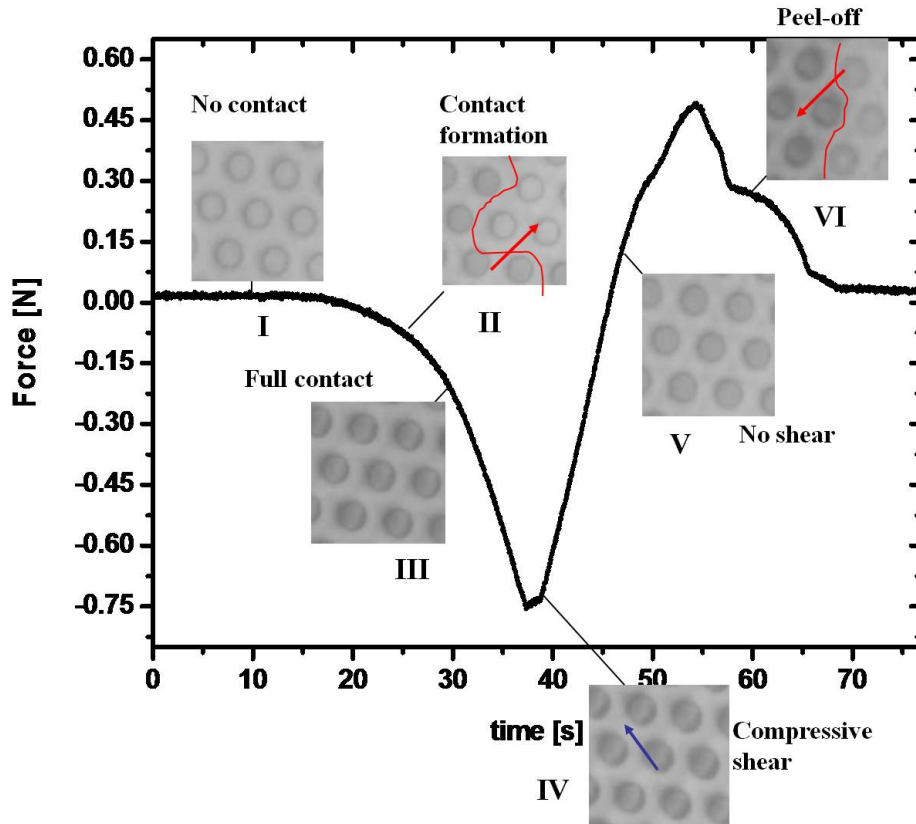


Figure 4.5: Force-time plot accompanied with *in situ* video snapshots of the sample-probe interface. For 0.75 N preload, I- pillars tips before contact, II- contact formation with darker circles indicating pillars in contact, III- all pillars in contact, IV- pillar tops in compressive shear, V- no residual shear and full contact, VI- Peel-off with adhesion. Line in II and VI demarcates the contacted area from peeled area.

pillar tops with respect to their bottoms can be observed; this results in some blurring. During retraction of the probe, the lateral shift disappears and the pillar top faces are again in intimate contact with the probe (inset V). Detachment of the pillars from the probe is observed in the form of a peel wave in the direction indicated by the arrow (inset VI). Dark circular regions again indicate pillars in contact, while light circular regions indicate pillar top surfaces detached from the probe.

For the higher preload of 5 N, the observations are different (Figure 4.6). After contact formation and lateral displacement of the pillar tops with respect to their bottoms (inset

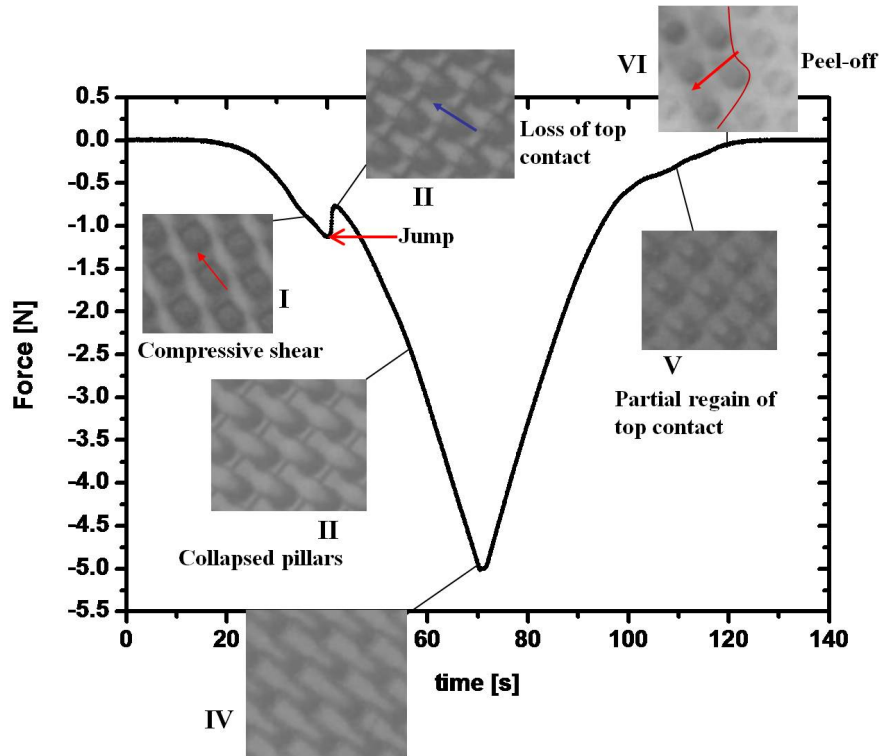


Figure 4.6: Force-time plot accompanied with *in situ* video snapshots of the sample-probe interface. For 5 N preload, I- laterally displaced pillar tops, II- pillars flipped after jump in force (≈ 1.18 N), III and IV- pillars lying flat on PDMS backing, V- apparent recovery from flip during retraction and VI- detachment with peel wave, no adhesion (arrows indicate direction of contact/shear).

I), a rapidly propagating wave corresponding to the flipping of pillars from top contact to the side seems to occur. This is synchronous with a jump in the measured force at around 1.15 ± 0.05 N. Insets II and III show pillars lying flat after the flip. At even higher loads, the flipped pillars are seen flattened against the PDMS surface of the backing layer and touching neighbouring pillars (inset IV). During unloading the video suggests that the pillars flip up and show only lateral displacement with respect to their bottoms (inset V). The subsequent peel off wave is observed to proceed much faster in comparison to that of the low preload case (inset VI). The demarcation of the peeled off pillars (light gray) from the attached pillars (dark gray) is shown by the superimposed line.

Side view images of the loading-unloading process were obtained with SEM. A flat Si probe

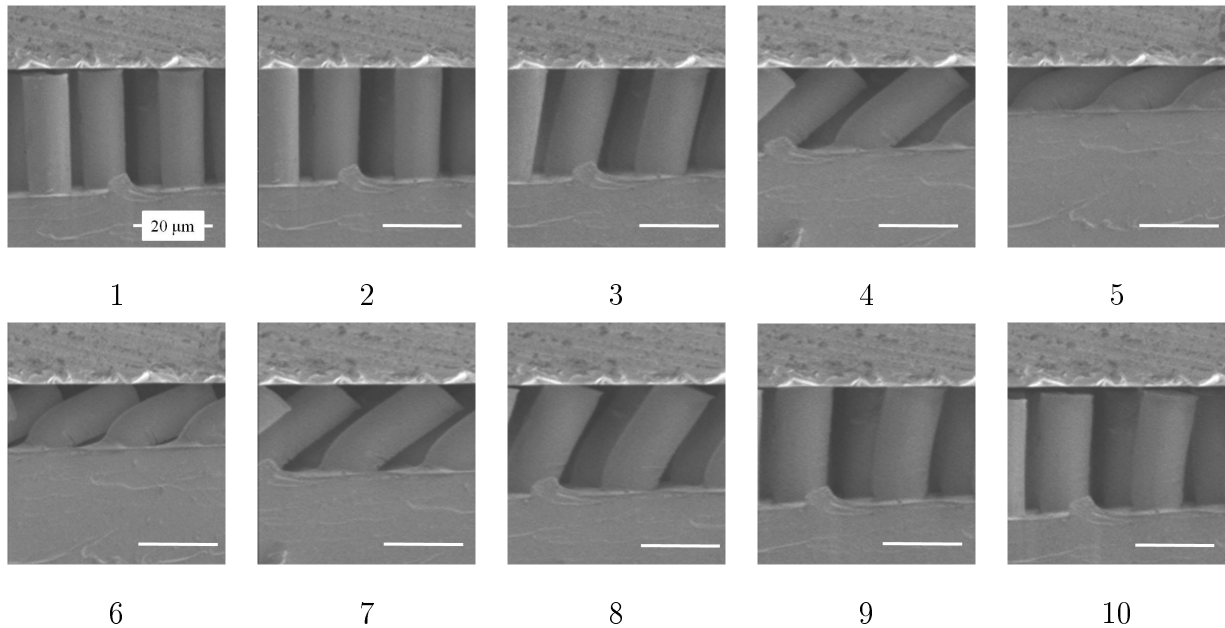


Figure 4.7: Side-view *in situ* snapshots of adhesion test on micropillar array in SEM. Sequences 1 to 5 show sample loading to high preload followed by unloading in 6 to 10. Note the partial retention of micropillar deformation at the end of test in sequence 10.

(smooth side of wafer) is brought in contact with the PDMS pillar array using a micromanipulator. Images 1 through 10 of Figure 4.7 show the loading sequence, 1-5 and unloading sequence, 6-10 in SEM. After contact formation (image 2), further loading leads to bending of the pillars in one direction (image 3 and 4). The pillars appear to lose the top face contact with the probe in these loading sequences. Maximum compressive load is reached in the next sequence where pillars are crushed under the probe, image 5. During unloading, as the probe retracts the pillars flip up (images 6 and 7). Eventually the pillars appear to regain top contact and/or partial top contact (images 8 and 9) before complete detachment from the probe with retention of a slight bend (image 10).

4.4 Discussion

PDMS surface was structured to fabricate micropillars that mimic the first level of hierarchy of the gecko adhesion system. These pillar arrays can be switched from a state of adhesion to non-adhesion by changing the applied preload. The short range van der Waals forces which

are responsible for the measured adhesion require the formation of an intimate contact. All tests were performed at a low velocity of $1 \mu\text{m/s}$ which can be assumed to be in equilibrium. Thus effects of pillar spring back can be neglected for present discussion.

4.4.1 Effect of preload change

Low pull-off strengths (28.6 kPa) obtained for extremely low preloads (0.5 kPa) are indicative of the fact that a certain minimum compressive loading is necessary before an intimate contact with the probe surface can be established (Figure 4.3). A minimum preload of 3.5 kPa was determined to be required for achieving the plateau pull-off strength of 60 kPa. The adhesion remained almost unchanged when the applied preload was increased, indicating that there was no further increase in real contact area. For preload stresses above 120.9 ± 2.2 kPa, however, the sample showed a loss of adhesion with average pull-off strengths as low as 1.2 ± 1.1 kPa. Loss of adhesion with increase in applied pressure for relatively large PVS pillars ($l \times b \approx 0.250 \times 0.125$ mm, length 0.4 mm) on PVS backing and flat PVS was reported by Peressadko and Gorb [Peressadko2004]. The loss in adhesion was explained on the basis of elastic energy [Persson2005]. This energy stored during compressive loading is freed during unloading, which helps in breaking adhesive bonds at the interface. There was no measurable decrease in adhesion for flat PDMS with an increase in preload even for very high preloads (224 kPa). It remains unclear why Peressadko and Gorb [Peressadko2004] found such an effect on flat specimens.

4.4.2 Inferences from the *in situ* tests: low preload

The *in situ* videos with *Microtack* device have shown that contact formation proceeds as waves starting from the circumference of the probe. This suggests that the sample was misaligned. From the speed of the propagating wave, the misalignment can be estimated to be 0.2° . As the system alignment was optimized prior to the test, there are two other reasons which could explain this observation. The 6 mm diameter flat steel probe has a roughness with wavelengths much larger than the diameter of the pillars giving rise to topography

effects.

Secondly, the PDMS sample itself is not perfectly flat. Due to this, the pillars are not exactly normal to the probe which may induce an additional shear component to the applied normal compressive forces (see IV of Figure 4.5). Consequently pillar deformation occurs under compressive shear, which may be responsible for the observed lateral displacement of the top of the pillars with respect to their bottoms. The direction of the lateral displacement seems to be dictated by the misalignment. Retraction of the probe from a preload of 0.75 N initially relieves the compressive shear. Detachment proceeds as a peel wave in the direction opposite to that of the contact formation with the crack usually initiated at the edge of the circular contact interface between probe and sample. Owing to the intimate contact of each pillar with the probe, the peel-off wave proceeds at low velocity and adhesion is observed (see Figure 4.5).

4.4.3 Inferences from the *in situ* tests: high preload

Loading to a high preload causes the pillars to flip at forces of 1.15 ± 0.05 N. This is related to a sudden transition from top contact to side contact of the pillar in the video and is accompanied by a jump in the force time curve. The 'jump' can be due to slip of the adhesive contact and/or buckling of the pillars. It is expected that the aspect ratio of the pillar and roughness of probe will play a significant role in deciding between these two mechanisms. For example, a low aspect ratio pillar is highly resistant to buckling and is more likely to slip before it can buckle, whereas a high aspect ratio pillar will buckle before it slips from top contact. For an intermediate aspect ratio (such as AR 3 as in present case), there will be a competition between the two events. In this case the probe roughness would most likely decide between buckling and slip.

The probe retraction from high preload of 5 N, for which micropillars flip during loading, proceeds initially with the pillars separating from side contact with neighbouring pillars, but still retaining side contact with the probe. Upon further retraction the pillars flip up and appear to regain partial top surface contact shortly before the compressive shear stresses

are completely relieved (inset V Figure 4.6). The *in situ* SEM images which show the side-view of pillars during unloading confirm this observation (images 8-10 Figure 4.7). The detachment as a peel wave proceeds in the direction opposite to the contact formation and at a much faster rate than for low preloads. Low pull-off forces are measured because there is no intimate contact formed between the pillar top and the probe during retraction. SEM images after complete unloading show that some pillars retain a slight bend.

4.4.4 Insights from theory

Let us assume that the 'jump' in force, which closely corresponds to the flipping of pillars and loss of top face contact, is due to buckling. Theoretical force for pure Euler buckling is given by [Glassmaker2004], [Ashby2000], [Wang2009a]:

$$F_{crit} = \frac{n^2 \pi^2 EI}{h^2}, \quad (4.1)$$

where E is the Young's modulus of the pillar, n is the half-wavelength of the buckled shape, I is the second moment of area ($I = r^4/4$), for circular cross-section with radius r , and h is the length of the pillar. The pre-factor n takes different values with one end always clamped i.e. fixed at the backing while the other end is: free to translate or rotate ($n = 0.5$), free to translate but not rotate ($n = 1$), free to rotate but not translate ($n = 1.43$) or is also clamped at the other end ($n = 2$). Table 4.2 lists the critical forces calculated using the above equation and forces measured with both setups.

Measured force at jump, per pillar [μN]		Calculated buck- ling force, per pillar [μN]		
		$n = 1$	$n = 1.43$	$n = 2$
<i>Macroscopic Adhesion testing Device</i>	32 μN	7 μN	15 μN	28 μN
<i>Microtack device</i>	14 μN			

Table 4.2: Comparison of theoretical and measured critical buckling force

Comparing the theoretical force per pillar with the measured force, it is clear that the

measured force at jump in the *Macroscopic Adhesion testing Device* ($32 \mu\text{N}$) is close to the force expected for $n = 2$ ($28 \mu\text{N}$). In contrast, the jump force measured using the *Microtack* device ($14 \mu\text{N}$) corresponds closely to that calculated using $n = 1.43$ ($15 \mu\text{N}$). The difference in buckling forces obtained for the different setups can be attributed to differences in alignment: misalignment is more critical for loss of contact with a larger diameter probe as used in the *Microtack* device. In addition, the large diameter probe may statistically lead to lower adhesion. This could lead to pillars having a clamped-free configuration for the *Microtack* device (steel, $d = 6 \text{ mm}$) and a clamped-clamped configuration for the *Macroscopic Adhesion testing Device* (glass, diameter $d = 1 \text{ mm}$).

Although the measured force values match quite well with the theoretical predictions it cannot be conclusively claimed that the buckling instability corresponds to the jump. Above calculations ignore the effect of the backing layer and assume a defect free sample area. Recent studies have shown that the backing layer can have a strong effect on adhesion [Schoen2010], [Guidoni2010]. As mentioned earlier, slip could also lead to such a jump in force. New experiments are underway in which the influence of the aspect ratio as well as roughness of the probe surface on adhesion of the pillars will be systematically investigated. The results indicate that adhesion is fully reversible (as in Figure 4.4). This suggests that retention of small deformations (as seen in image 11 Figure 4.7) in the pillars at the end of the loading-unloading cycle to high preloads is not critical for the reversibility of the system. The effect of velocity is currently being investigated to clarify the role of (visco)elastic energy in pressure actuated adhesion.

4.5 Conclusions and outlook

- PDMS micropillars with AR 3 (diameter $10 \mu\text{m}$, length $30 \mu\text{m}$) were tested for normal adhesion performance using standard load-displacement tests. Pull-off forces 7.5 times higher than those of flat PDMS under the same test conditions were recorded.
- Samples were tested for switchability of adhesion by changing the applied preloads. Two preload dependent states of adhesion and non-adhesion were found. For applied

stresses between 3 and 125 kPa, an adhesion maximum of 60 kPa is realized, whereas for preloads larger than 125 kPa, very low adhesion strengths of 1.2 kPa are recorded.

- The repeatability of the on-off states was also tested for 50 cycles. Full switchability from the adhesive to the non-adhesive state by a simple change of the applied preload was found.
- A qualitative understanding of the actuated adhesive system based on *in situ* videos and SEM studies of adhesion tests was presented. The actuation mechanism mimics that of the gecko adhesive system in that the change of orientation of the micropillars is responsible for loss in adhesion. Intimate contact at pull-off from low applied preloads leads to high adhesion. Loss of contact during high applied preload leads to lack of intimate contact re-establishment during pull-off resulting in loss of adhesion.

Unlike conventional adhesive tapes which can only be directionally peeled off, the pillar PDMS array can be easily detached using higher pressure. This might be of potential importance in bonding two rigid substrates.

Chapter 5

In situ observation of contact mechanisms in bioinspired adhesives at high magnification¹

Abstract

The contact mechanisms of bioinspired microfibrillar adhesives are analyzed using in situ scanning electron microscopy. During adhesion tests it is observed that (a) the superior adhesion of mushroom shaped fibrils is assisted by the stochastic nature of detachment, (b) the aspect ratio of microfibrils influences the bending/buckling behaviour and the contact reformation and (c) the backing layer deformation causes the microfibrils to elastically interact with each other. These studies give new insights into the mechanisms responsible for adhesion of bioinspired fibrillar adhesives

5.1 Introduction

During the last decade, researchers have developed sophisticated methods to fabricate adhesives inspired by the adhesion system of the gecko. Fibrillar structures were fabricated to

¹This chapter was published as a communication [Paretkar2011a]

mimic the natural system and to maximize adhesive performance [Sitti2003], [delCampo2007], [Schubert2007], [delCampo2007a], [Ge2007], [Jeong2009]. Numerous experimental and theoretical studies were carried out to advance the understanding of the underlying contact mechanics [Jagota2002], [Arzt2003], [Hui2004], [Spolenak2005], [Greiner2007], [Spuskanyuk2008], [Long2008]. However, to validate those models, in situ visualization of the contact phenomena at high magnification is necessary. Several groups have presented studies using optical microscopy combined with adhesion measurements [Glassmaker2004], [Crosby2005], [Glassmaker2007], [Vajpayee2008]. These studies show for example the bending of fibrils, the actual contact area or the attachment and detachment front. Although these experiments have given some insight into contact mechanisms, they are not suitable for investigating the processes at interfaces due to the limited magnification of the applied optical microscopy. Advanced bioinspired adhesives have features such as flaps (mushroom tips), which are in the sub-micron range [Kim2006], [delCampo2007a], [Lee2009], [Murphy2009]. To visualize the contact mechanisms at the length scale of these features, new measurement systems are required. Here, scanning electron microscopy assisted visualization of the contact mechanisms during an adhesion test on fibrillar surfaces is demonstrated.

5.2 Experimental methods

Microfibrillar arrays of polydimethylsiloxane (PDMS) with pillars of different aspect ratios (height/diameter) and tip geometries were fabricated using photolithography and soft-molding processes. SU-8 resists (2010, 2025, Micro Resist Technology, Berlin, Germany) were used to prepare templates in a standard photolithography process. The templates were then silanized using hexadecafluoro-1,1,12,2-tetrahydrooctyltrichlorosilane and subsequently filled with PDMS (Sylgard 184, Dow Corning, 10:1 mixture). After cross-linking at 75°C for at least 14 h, the samples were carefully removed from the molds. For specific fabrication details, especially the fabrication of mushroom tip structures, see [delCampo2007].

Contact experiments were performed in an environmental scanning electron microscope (ESEM, FEI Quanta 400 F), extended with a micromanipulator (Kleindieck Nanotechnik,

GmbH, Germany) and a self-constructed cantilever for force measurements. Probes were mounted on the tip of the micromanipulator and the sample was fixed to the cantilever. The low vacuum (pressure ≈ 100 kPa) modes of the ESEM allowed performing the experiments on non-conductive materials such as PDMS without further treatment.

In situ tests were performed by positioning the probe at the focal point using the micromanipulator. The sample was brought into contact with the probe using the ESEM stage and retracted again. This enabled high displacement with high magnification without losing the focus on the interface. At the same time, the deflection of the cantilever during the contact experiment was indicative of the resulting forces.

5.3 Results and discussion

Experiments were performed to investigate the following aspects of contact phenomena for fibrillar surfaces: influence of pillar tip shape on adhesion, bending and buckling of pillars under compression and response of the backing layer to applied pressure.

5.3.1 Influence of pillar tip shape on adhesion

Figure 5.1 shows sequences of side images taken during contact experiments using a spherical probe (on top) on a PDMS fibrillar array with heights of $20 \mu\text{m}$ and aspect ratio 2. In the top sequence the pillars had tips with mushroom shape, while in the bottom sequence the pillars had rounded edges. For each sequence the first image shows the pillars at maximum applied compressive preload. The inlays show the interface at high magnification during contact formation of a single pillar. The subsequent images exhibit an intermediate tensile stress state during retraction of the sample and the last image was taken immediately before detachment. Both samples show adhesion to the spherical probe.

However, while most of the pillars with rounded edges detach at low applied tensile strain, a large fraction of the mushroom shaped pillars sustain much higher strains before detachment. Due to the curvature of the spherical probe it was expected that the pillars at the

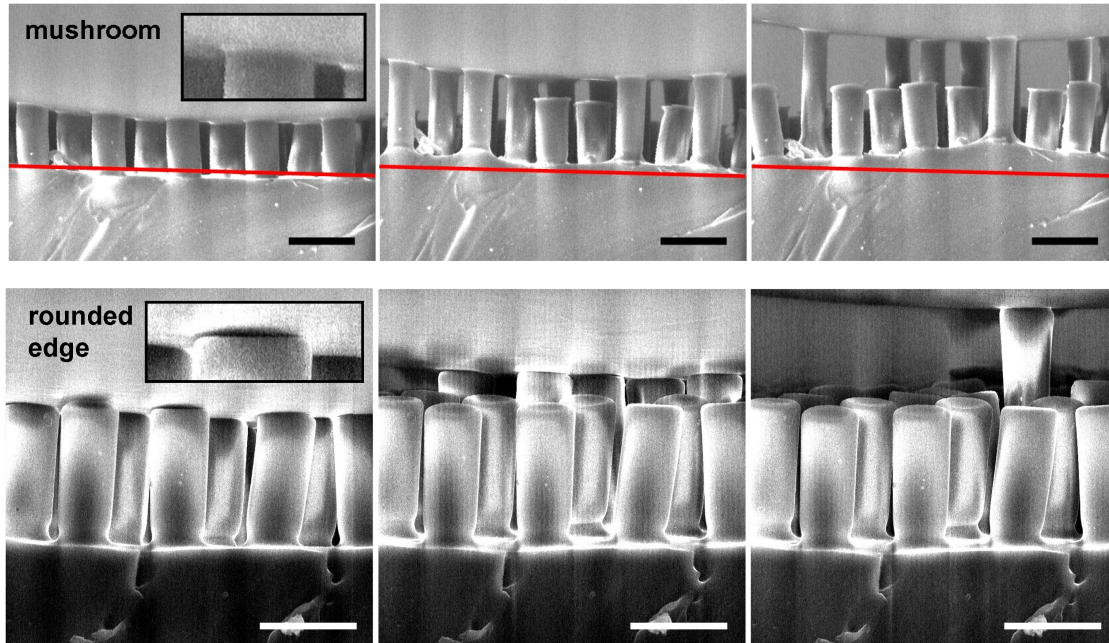


Figure 5.1: Sequences of ESEM side views of pillars with mushroom tips (top) and rounded edges (bottom). Pictures were taken at maximum compressive load (left), during retraction of the spherical probe (center) and immediately before detachment. Insets show interface during contact formation at high magnification, scale bar $20 \mu\text{m}$

contact boundary, which experience the highest strain, would be the first to detach and the detachment front would proceed to the center of the contact area. Instead, it was observed that the pillars detached in a stochastic manner rather than in an orderly fashion. In addition, individual pillars showed very different elongations prior to detachment due to different adhesive strength of the individual pillars. The strain before detachment was found to be approx. 65% for mushroom tip pillars and 55% for pillars with rounded tips. While several mushroom tip pillars in this experiment were extended to maximum elongation, this was found only for a single pillar with rounded edges. This observation indicates that the tip shape, even if it may not significantly affect the adhesion of one single pillar, greatly influences the statistics of detachment in an array of pillars [McMeeking2008].

5.3.2 Bending and buckling of pillars (pressure switching behaviour)

Previous studies have pointed out that the adhesive strength for fibrillar arrays drops significantly at high preload; this effect has been exploited in the design of an adhesive system that allows switching between an adhesive and a non-adhesive state [Hui2007]. The switching was attributed to the loss of contact of the pillar tips due to bending and/or buckling. The sequences in Figure 5.2 show the behaviour of mushroom tip pillars with aspect ratio 3 (top) and 5 (bottom) under compressive preload. In the initial state, the pillars are in intimate contact with the flat probe. With increasing load the low aspect ratio pillars in sequence start to bend, lose tip contact and finally lie flat at maximum applied compressive preload. In the last image of the sequence, the bent pillars show surface wrinkles, which have not yet been reported for an adhesion test on fibrillar adhesives.

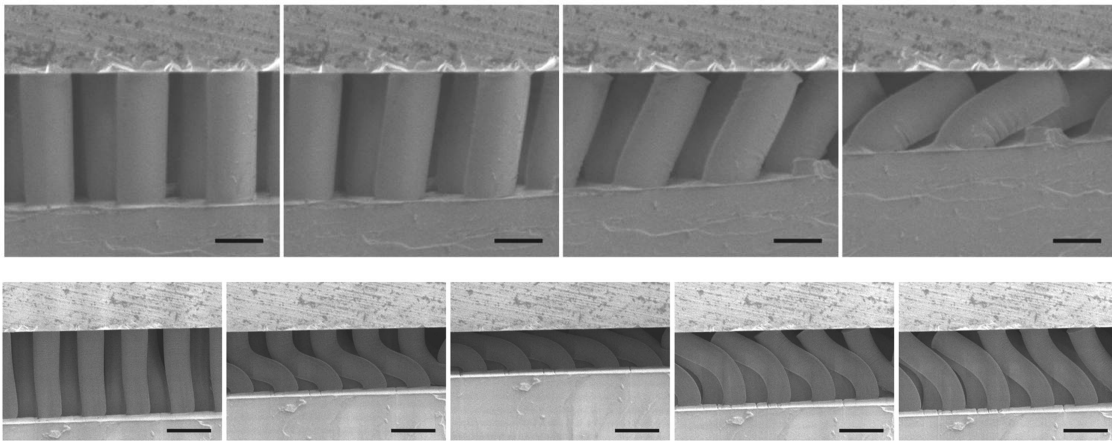


Figure 5.2: Switching behaviour due to bending and buckling of pillars with aspect ratio 3 (top sequence), scale bar $10\ \mu\text{m}$ and 5 (bottom sequence), scale bar $20\ \mu\text{m}$. Increasing compressive stress from left to right for top and bottom 3 images. Partial release of compressive load in the last image in bottom sequence.

The high aspect ratio pillars buckle with increased compressive preload and exhibit an "S" shape after buckling. Compared to the aspect ratio 3 pillars, the pillars in bottom row sequence sustain tip contact even at large deformation and pillars lose tip contact only at very high preload. Unlike the low aspect ratio pillars, the high aspect ratio pillars appear to regain tip contact during unloading (last sequence in bottom sequence). This new vi-

sualization technique enables us to precisely observe the deformation behaviour of pillars under compressive loading and may lead to a better understanding of bending and buckling phenomena of small scale polymeric materials.

5.3.3 Backing layer response to applied pressure

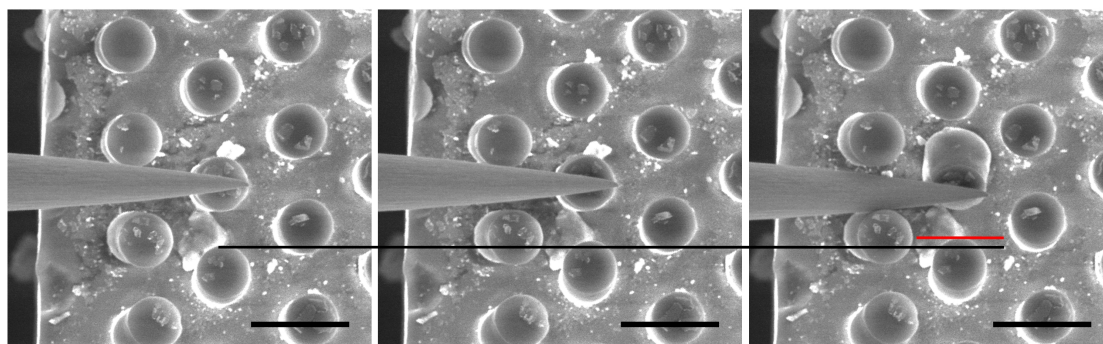


Figure 5.3: Experimental evidence for elastic interaction of the pillars through the backing layer: when the central pillar is compressed with a needle, the adjacent pillars bent towards the central pillar (see marker line), scale bar $20\ \mu\text{m}$

Whereas several mechanics studies acknowledge the importance of the backing layer contribution to the adhesion of fibrillar arrays [Kim2007b], [Long2008], the interaction between the pillars through the backing layer has not yet been observed experimentally. Figure 5.3 shows the response of six hexagonally packed pillars to a load applied to the central pillar. For this experiment, a sharp needle was attached to the micromanipulator. To better visualize the deformation, high contrast particles were dispersed on the fibrillar surface. The applied load presses the central pillar into the backing layer, causing the neighbouring pillars to be slightly bent towards the central pillar. The displacement of one of the surrounding pillars is highlighted by the markerline in Figure 5.3. In addition to the top view, the backing layer interaction can also be visualized in side view as seen from Figure 5.1. There, the red guide line roughly indicates the initial position of the backing layer. It can be seen that the tension in the pillars causes a severe deformation of the backing layer, affecting the orientation of the adjacent pillars. This effect will be especially important for adhesion to rough or spherical surfaces. For example, if a pillar adheres to a spherical probe or an asperity of a

rough surface, the surrounding pillars experience a bending moment away from the adhering pillar. This change in orientation of the neighbouring pillars with respect to the contacting surface may exert significant influence on the adhesion. Besides this, the severe deformation of the backing layer greatly contributes to the stored elastic energy of the adhesive system and, thus, has to be considered in the energy balance of the contact mechanics models.

5.4 Conclusions

A new setup for adhesion experiments with *in situ* visualization capabilities in an environmental scanning electron microscope (ESEM) was presented. The influence of tip shape, bending and buckling under compressive preload and the interaction of pillars through the backing layer on adhesion were investigated and gave additional insight not available otherwise.

Mushroom shaped pillars did not show a notably higher elongation before detachment than pillars with rounded edges; however, the fraction of pillars retaining contact with the probe at maximum elongation was significantly larger. This points to the stochastic nature of the detachment process of fibrillar surfaces, which may be crucial for adhesive performance.

The aspect ratio of the pillars determined the deformation mode under compressive preload. In our experiments, pillars with aspect ratio 3 bent and lost tip contact. Aspect ratio 5 pillars buckled before the tip contact was lost and regained contact again during unloading. Such observations support the rational design of switchable adhesive devices exploiting an adhesive/non-adhesive transition.

With the new set-up it was possible to visualize the interaction of individual pillars through the backing layer in top and side view. Overall, these observations give new insight into the adhesion mechanisms of fibrillar adhesives and will, by improving the mechanistic understanding, support the design of bioinspired adhesive surfaces.

Chapter 6

Preload responsive adhesion: effects of aspect ratio, tip shape, and alignment¹

Abstract

The adhesive response of polymer surfaces structured with arrays of cylindrical fibrils was tested as a function of preload. Fibrils with tip shapes of end-flaps and round edges had diameters of 10 to 20 μm and aspect ratios 1 to 2.4. Mechanical buckling instability of the fibrils was recognized to be reversible and used to generate two states of adhesion and non-adhesion. Non-adhesion in round edge fibrils was reached at preloads that induce fibril buckling, whereas fibrils with end-flaps showed adhesion loss only at very high preloads. The round edge acted as a circumferential flaw prohibiting smooth tip contact recovery, which the end-flaps by themselves folding and unfolding made possible. *In situ* studies showed that after reversal of buckling the end-flaps unfold and re-form contact under available compressive stress. At very high preloads, however, end-flaps are unable to re-form contact as indicated by a large kink at unbuckling and the lack of sufficient compressive stress. Additionally, the end-flaps showed varying contact adaptability as a function of the fibril-probe alignment, which further affects the stress for adhesion loss. The combined influence of preload, tip-shape and alignment on adhesion can be utilized to control adhesion switching in bioinspired fibrillar arrays.

¹This chapter is in preparation for submission as a full paper with co-authors M. Kamperman, A. Lindner, C. Creton, A. Jagota, R. McMeeking and E. Arzt.

6.1 Introduction

Synthetic gecko-inspired adhesives rely on fibrillar structures which create non-chemical adhesion by concentrating intermolecular forces between two bodies, see recent reviews [Kamperman2010], [Boesel2010], [Jagota2011]. The potential to incorporate switchability in adhesion has only recently been explored. Examples include systems which respond to external stimuli such as temperature [Reddy2007], [Xie2008], magnetic field [Northen2008], mechanical stretching [Jeong2010] and pneumatic pressure [Nadermann2010]. The common underlying principle is a reversible change in the area of contact between the adhesive surface and the test probe, leading to a change in adhesion.

In Chapter 4, the adhesion dependence on preload was established for PDMS fibrils with aspect ratio (AR) of 3. Pull-off strengths at low preloads were high, whereas loss in adhesion was shown to occur at high preloads. Reversible buckling transition of the fibrils was observed for preloads higher than a critical preload which made fibrils mechanically unstable. The transition between the states of high and low adhesion was also shown to be reversible and repeatable. Whenever the fibrils were unable to re-form an intimate contact with the probe, after reversible buckling, adhesion was lost. Fibrils, however, were able to re-form probe contact at low preloads in spite of undergoing reversible buckling. Thus there is an important difference between the critical preload that causes reversible buckling and the preload that causes adhesion loss. This is investigated further in the present Chapter and the mechanism of adhesion transition is studied with regards to the following issues:

First, the dependence of the critical preload which causes the mechanical instability in fibrils on the fibril's aspect ratio (AR) will be established. According to Euler-Bernoulli buckling theory it is expected that higher AR fibrils will buckle under lower preload stress [Timoshenko1961]. *In situ* adhesion tests (Chapter 5) at high magnification showed that the AR influences the loss of the fibril-probe contact interface. In the present study, fibrils with different aspect ratios (h/d) of 1 to 2.4 and diameters 10 to 20 μm were fabricated and the influence of AR on the preload that causes buckling (or critical preload) was studied.

Second, the influence of tip shape on the mechanism of adhesion transition from high to low

adhesion is investigated. Contact re-formation during the reversal of buckling and thereby detachment was shown to be influenced by the fibril tip shape by the *in situ* studies (Chapter 5). In this Chapter the contact re-formation during the reversible buckling is compared between two different terminal contact shapes of end-flaps (denoted Type 1) and round edges (Type 2).

Third, practical considerations of using fibrillar arrays as switchable adhesives demand contact adaptability at non-aligned orientations. With this motivation we recently investigated the orientation effects on adhesion performance [Kroner2011]. For structured samples with low AR (< 1) it was shown that small misalignment ($\approx 0.2^\circ$) led to a large drop in adhesion. The effect of systematic change in sample alignment with respect to a flat test probe on the preload dependent adhesion is investigated here.

With this background, Type 1 and Type 2 adhesives having different aspect ratios were tested for their adhesion performance by varying applied preloads and sample alignment. The focus throughout is to gain mechanistic details to understand switchable adhesion.

6.2 Experimental methods

Photolithography and replica molding techniques were used to structure the PDMS surface with an array of hexagonally packed micropillars. PDMS fibrils having four different aspect ratios of 1, 1.7, 2 and 2.4 and diameters of 10, 14 and 20 μm were fabricated (Table 6.1). Different diameters resulted from the chosen diameters of the circular patterns in the photomasks. The length of fibrils was governed by the thickness of the SU-8 films. Table 6.1 summarizes the dimensions of the pillars (length, h and diameter, d) for four aspect ratios of Type1 and Type 2 fibrils on a PDMS backing having thickness of around 2-2.5 mm.

6.2.1 Fabrication of micropillars with end-flaps: Type 1 adhesives

Thermal strain mismatch induced cracking of SU-8 films was used to generate end-flaps (similar to mushroom-heads) on fibrils following previous work of del Campo *et al.* [delCampo2007].

Aspect ratio	Pillar h, d Type 1 [μm]	Pillar h, d Type 2 [μm]	Width of end-flaps [nm]	Thickness of end-flaps [nm]
1	20, 20 μm	20, 20 μm	$360 \pm 10 \text{ nm}$	$310 \pm 40 \text{ nm}$
1.4	20, 14 μm	20, 14 μm	$565 \pm 5 \text{ nm}$	$365 \pm 35 \text{ nm}$
2	20, 10 μm	20, 10 μm	$1250 \pm 50 \text{ nm}$	$635 \pm 15 \text{ nm}$
2.4	33, 14 μm	27, 11 μm	$450 \pm 5 \text{ nm}$	$340 \pm 10 \text{ nm}$

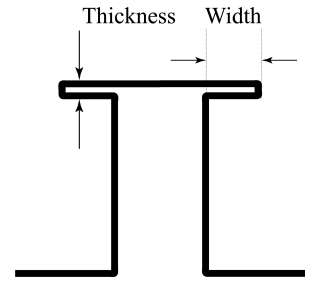


Table 6.1: PDMS fibril dimensions for different AR adhesives of Type 1 (end-flaps) and Type 2 (round edges). End-flap dimensions and schematic of the end-flap terminated fibril (right).

The photothermal crosslinking process in SU-8 is completed only after a post-exposure bake ($T = 95 \text{ }^\circ\text{C}$) [delCampo2007b]. Slow cooling after the bake is usually recommended to minimize the thermal stresses in the stiff, fully cross-linked SU-8. However, by placing the wafers directly on a cool steel surface ($T = 20 \text{ }^\circ\text{C}$) large thermal stresses were induced in the SU-8 film. The magnitude of the equibiaxial thermal stress [Bowden1998] was estimated to be 19 MPa (SU-8 CTE = $50 \text{ ppm}/^\circ\text{C}$, Si CTE = $2.6 \text{ ppm}/^\circ\text{C}$). Thermal stress caused the SU-8 film to crack and delaminate from the wafer at the base of the cylindrical holes (Figure 6.1 (b)).

Cracks/gaps present in the SU-8 film (Figure 6.1 (a)), which have feature sizes greater than tens of nanometer get replicated in the PDMS structure due to its high fidelity [McDonald2002]. During the soft-molding procedure, the uncrosslinked liquid PDMS filled the lithographic holes in the SU-8 master as well as the submicron delamination gaps at the interface. Upon curing, when the PDMS was carefully peeled off from the SU-8 master, it contained fibrils with thin flaps at their ends. Uneven distribution of thermal stress led to variations in the delamination gaps. This, in turn, affected the shape and size of the resulting end-flaps. Sub-micron sized defects in the flap periphery or thickness variation were observed (Figure 6.2).

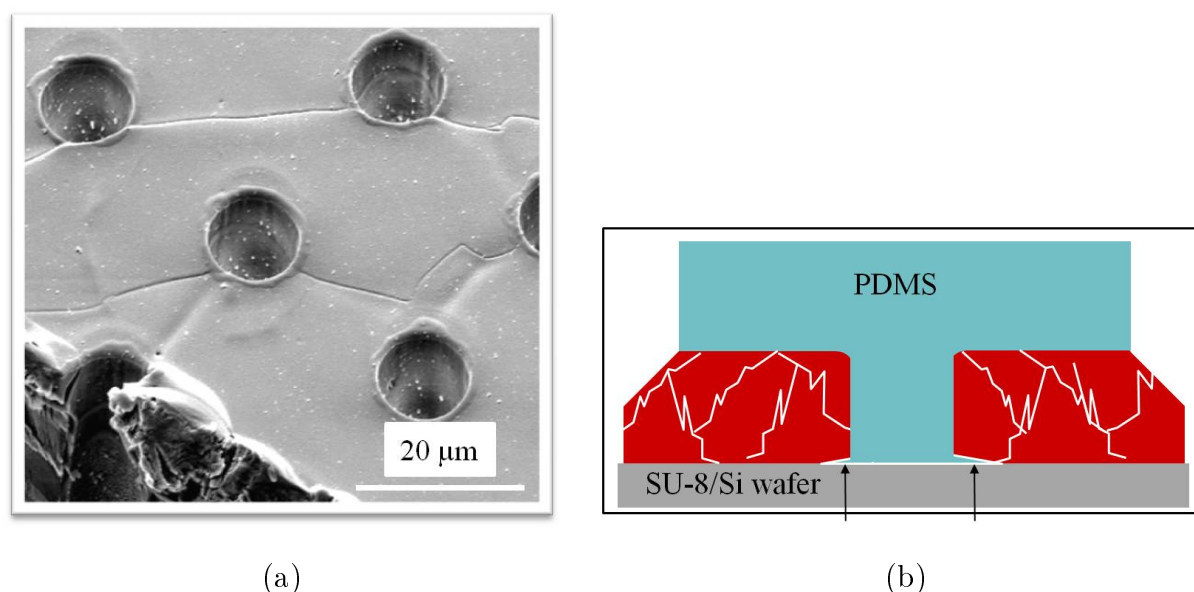


Figure 6.1: SEM micrograph of nanoscale cracks on the SU-8 resist film surface containing a hole pattern. Schematic representation of 3-D network of cracks and film delamination at SU-8/Si wafer interface due to thermal stresses (b). Liquid PDMS (blue) fills the hole and the gaps between SU-8 film (red) and the wafer (see arrows).

The end-flaps are similar to the "mushroom-shape" published earlier e.g. [Varenberg2008], [delCampo2007], with the exception that the flaps here are generally much *smaller* relative to the fibril diameter. Direct evidence of delaminated film was not possible due to the limited penetration depth of electron scanning in SEM. However, it was observed that the complete film peeled off only after a couple of soft molding cycles. A film peel-off resulting from such low mechanical stress was an indirect evidence of the underlying delamination at the interface. SEM micrographs of the different AR Type 1 adhesives investigated for tunable adhesion are shown in Figure 6.3.

6.2.2 Fabrication of micropillars having tips with round edges: Type 2 adhesives

Finite deformation due to surface tension effects has been known for soft solids such as PDMS [Hui2002], [Majumder2007]. Given a sharp corner in the SU-8 master, a slight rounding of the fibril edge results in the PDMS replica due to surface tension effects [Hui2002]. By

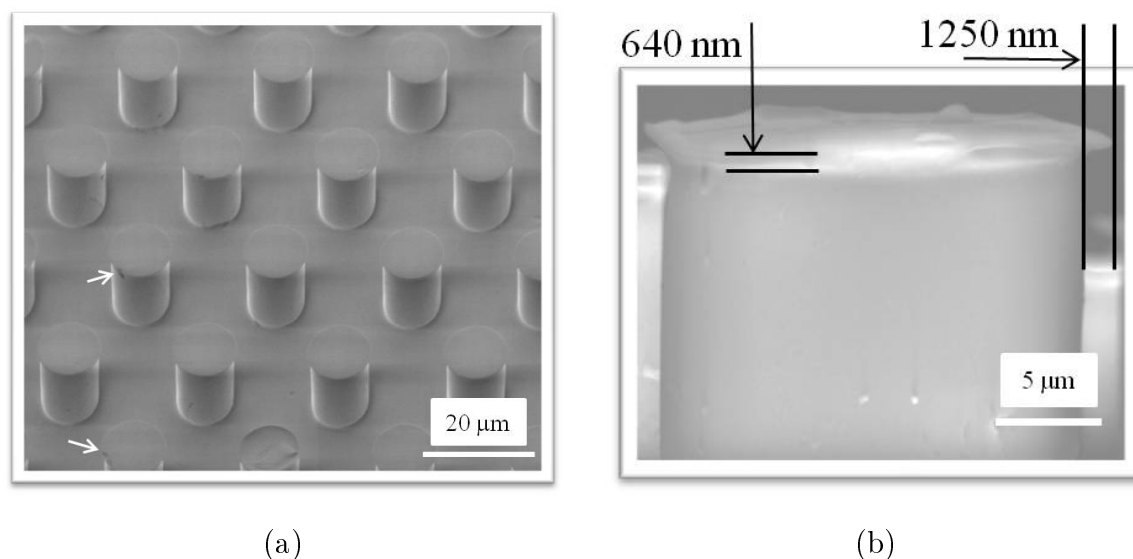


Figure 6.2: Type 1 fibrillar adhesive. SEM micrographs of (a) AR 2 fibrillar arrays and (b) fibril with end-flap. Arrows in (a) point to defects in end-flaps (<10% incidence within contacted fibrils). Dimensions of end-flaps are shown in (b).

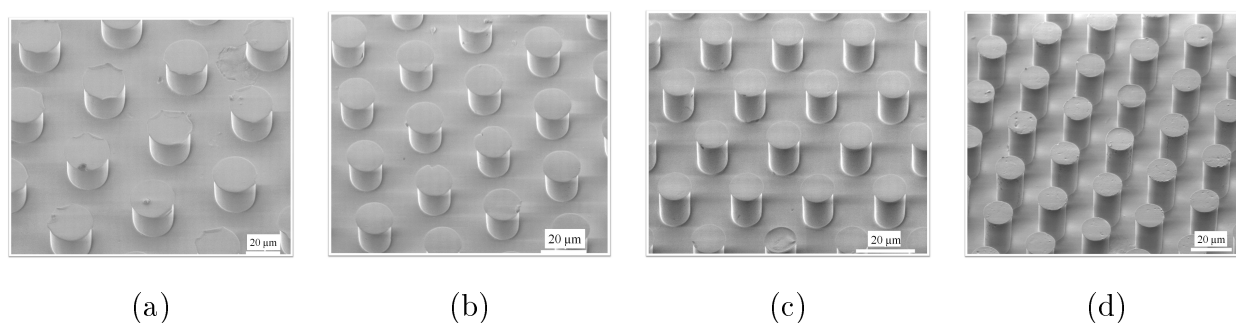
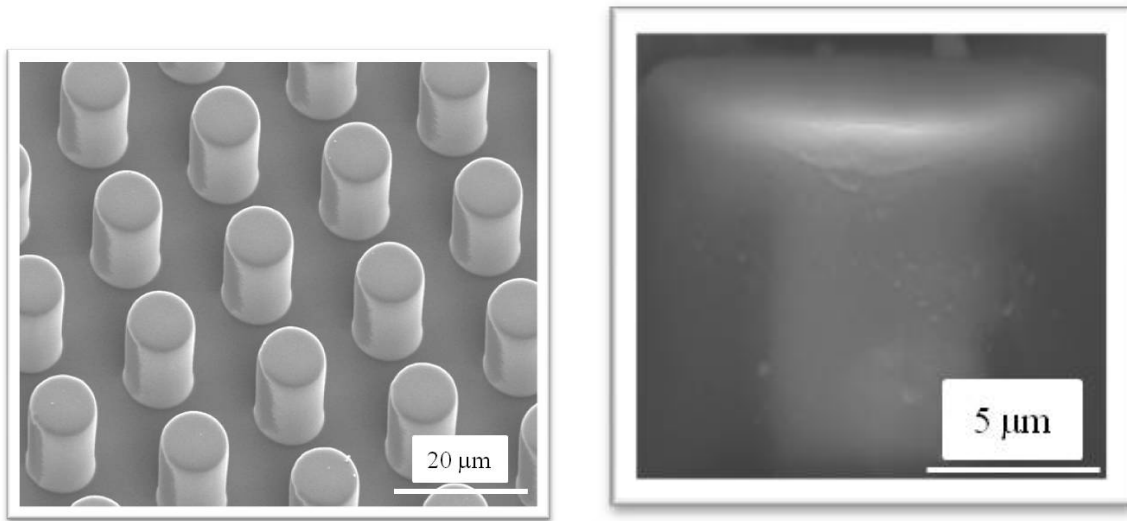


Figure 6.3: SEM images of Type 1 adhesives having end-flap terminated fibrils with aspect ratios of (a) AR 1, (b) AR 1.4, (c) AR 2 and (d) AR 2.4.

introducing a second molding step, rounding effects on fibril edges were amplified. The SU-8 master consisted of an array of cylindrical pillars. A primary mold of PDMS was replica molded from the SU-8 master to generate an array of hexagonally packed holes. A second molding step was carried out by using the primary PDMS mold as the new master. Prior to pouring liquid PDMS on the primary PDMS mold, it was thoroughly silanized (Chapter 3, Section 3.1.3). The silanization step was necessary to avoid PDMS-PDMS sticking. After curing and demolding, the resulting PDMS fibrils had round edges (Figure 6.4). The radius of curvature was approximately $1.85 \mu\text{m}$. SEM micrographs of the different AR Type 2

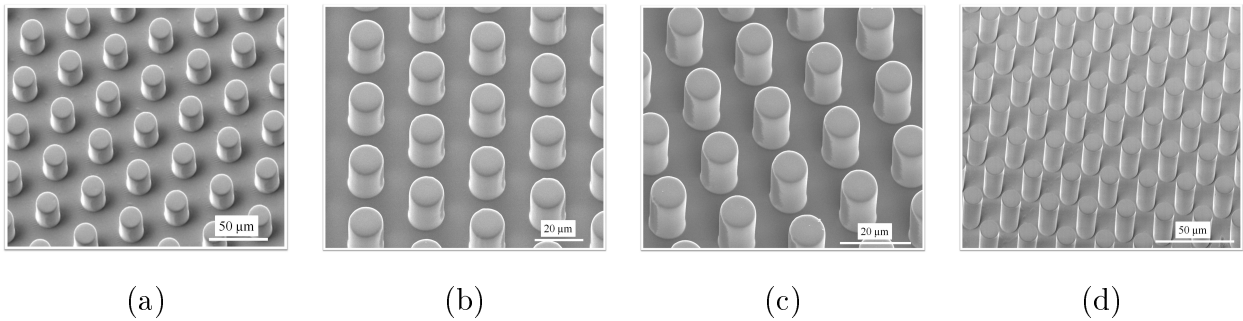


(a)

(b)

Figure 6.4: Type 2 fibrillar adhesives. SEM micrographs of (a) AR 2 fibrillar arrays and (b) fibril with round edges having radius of curvature $\approx 1.85 \mu\text{m}$.

adhesives investigated for tunable adhesion are shown in Figure 6.5.



(a)

(b)

(c)

(d)

Figure 6.5: SEM images of Type 2 adhesives having tips with round edges and fibrils with aspect ratios (a) AR 1, (b) AR 1.4, (c) AR 2 and (d) AR 2.4 .

6.2.3 Adhesion Testing

6.2.3.1 Test method

Adhesion tests were performed on the *Macroscopic Adhesion testing Device* (Figure 3.4) and *Microtack* (Figure 3.5) using a flat test probe ($d = 1 \text{ mm}$, polished steel cylinder).

The flat probe is mounted on a rigid force sensor in the *Microtack* whereas on a double-beam spring of spring constant $k = 430 \text{ N/m}$ in the *Macroscopic Adhesion testing Device*. PDMS sample was attached with its non-structured side onto a glass slide using oxygen plasma activated bonding. The translucent PDMS adhesive sample allowed for visualization of the fibril-probe interface using optical microscopy. Different preloads were achieved by controlled compression of the structured adhesives against the flat probe and the resultant pull-off forces were recorded. The test velocity was $10 \mu\text{m/s}$.

6.2.3.2 Sample alignment

Alignment of the fibrillar sample with respect to the flat test probe was closely controlled. The parallel sample-probe alignment was reached by systematically changing the sample orientation with respect to the probe-double-beam and comparing the resultant pull-off forces at a predefined preload (see supplementary information, Appendix II, Figure 8.2). The aligned state yielded invariance of preload and pull-off force for changes within 0.02° in both U and V axes.

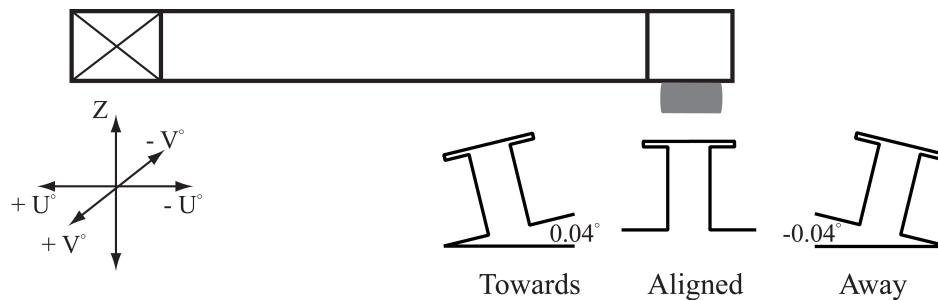


Figure 6.6: Schematic of the probe-double-beam and different fibril orientations along U-axis (*i.e.* along probe-double-beam) with respect to the aligned state. Probe is a flat polished steel cylinder, $d = 1 \text{ mm}$ shown in blue (not drawn to scale).

To study the effect of tip shape on contact adaptability as a function of preload, the fibril alignment was systematically changed with respect to the reference aligned state (Figure 6.6). The sample was tilted in steps of 0.04° , in the positive and negative directions along the U-axis (keeping the tilt along V-axis unchanged) with respect to the aligned state. For

each sample-probe alignment the entire set of preloads were applied and corresponding pull-off forces were recorded.

6.3 Results

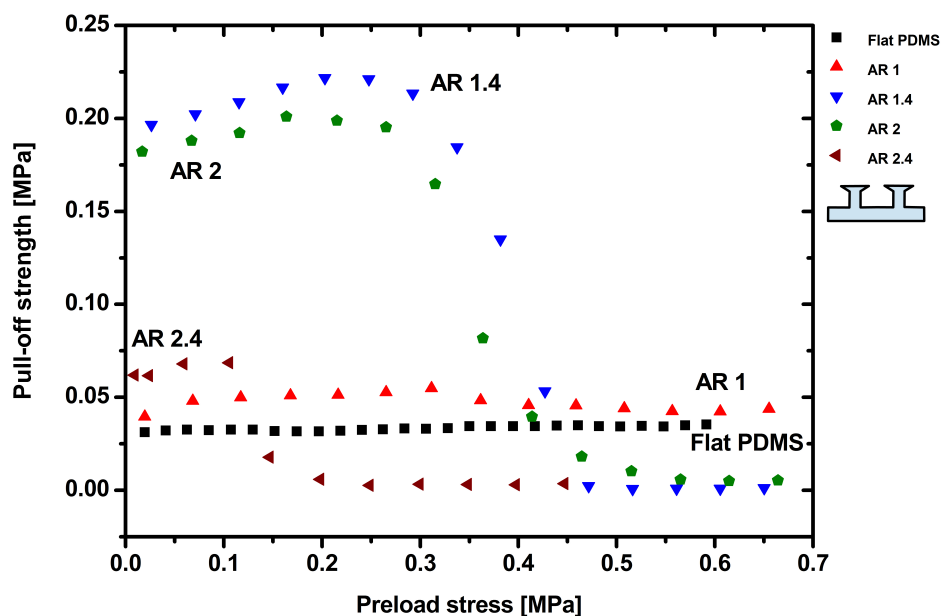
6.3.1 Aspect ratio

Figure 6.7 shows the measured pull-off strength as a function of preload stress for various aspect ratios of Type 1 (a) and Type 2 (b) adhesives. Control samples of flat PDMS having similar thickness (2-2.5 mm) to those of the structured samples were also tested.

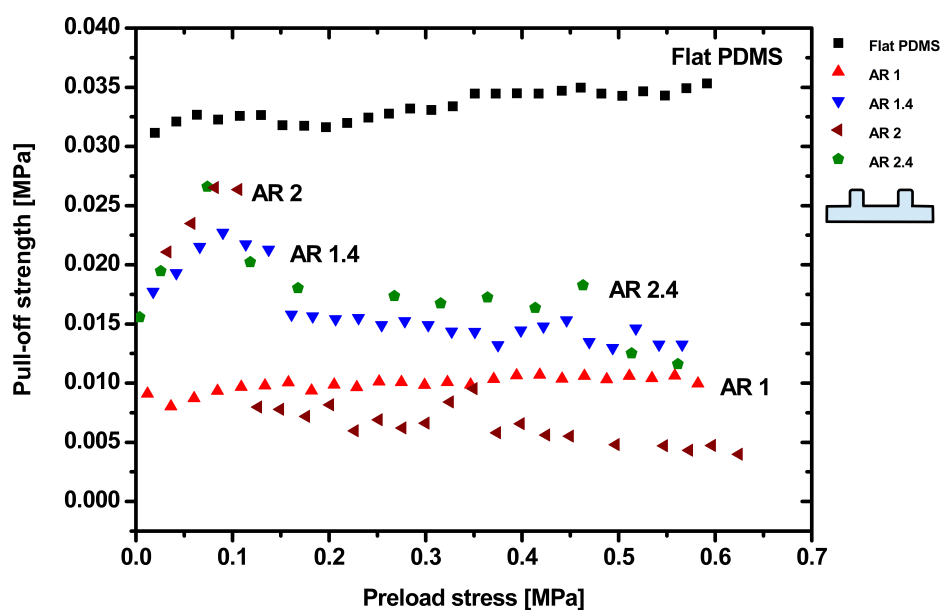
Flat PDMS controls had pull-off strengths of around 0.035 MPa which were insensitive to the preload stress. Repeated tests showed variations of less than 10% in pull-off forces over the range of preloads investigated.

Type 1 adhesives exhibited higher pull-off strengths than flat controls. For a range of low preload stresses (0-0.1MPa), pull-off strengths increased with applied stress for all samples with $AR > 1$. The increase in adhesion strength continued up to a preload stress of 0.03 MPa for lowest AR of 1.4. For higher preload stress, the pull-off strengths of Type 1 adhesives, with the exception of $AR = 1$, fell to levels even below that of flat PDMS. For example, the transition to a state of negligible adhesion was achieved around 0.2 MPa for AR 2.4 and around 0.45 MPa for AR 1.4 and 2. Stresses at which a significant loss in adhesion was measured were recorded as adhesion loss stresses σ_{loss} .

Type 2 adhesives showed pull-off strengths typically 20-30% lower than those of flat control samples, Figure 6.7 (b). AR 1 showed exceptionally low pull-off strengths. For a lower range of preload stress (≤ 0.1 MPa), pull-off strengths increased monotonically for all samples with $AR > 1$. The pull-off strengths fell rapidly with further increase in preload stress (> 0.1 MPa) such that largest stress was required for the smallest AR. Adhesion loss (σ_{loss}) was observed at preload stress > 0.17 MPa for AR 1.4, 2, and 2.4 of Type 2 adhesives.



(a)



(b)

Figure 6.7: Pull-off strengths as a function of preload stresses for various aspect ratio adhesives of (a) end-flap terminated fibrils (Type 1) and (b) round edge fibrils (Type 2). Aspect ratios 1.4, 2 and 2.4 show a drop in adhesion at various preload stresses (error within the size of the symbols).

6.3.2 Evolution of stress

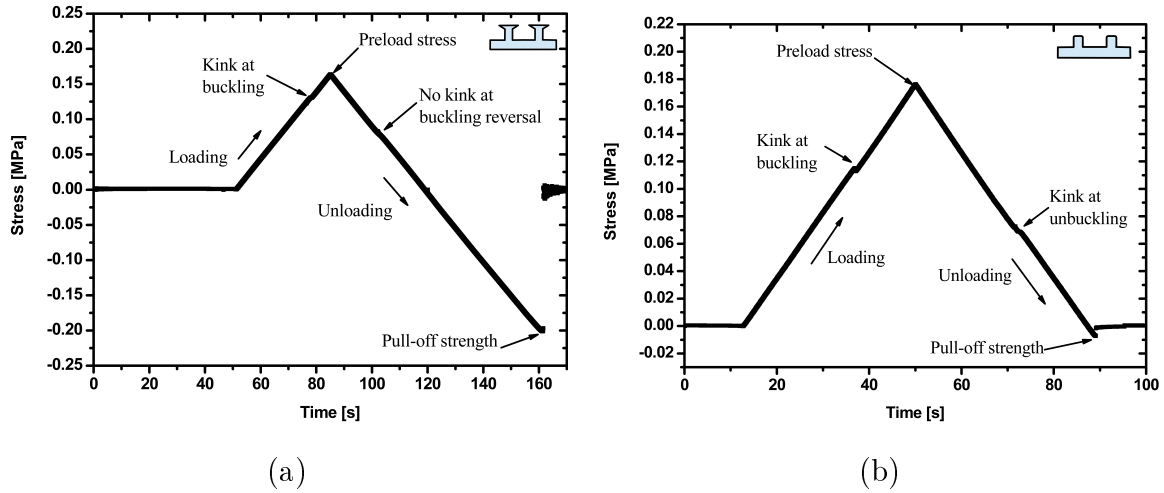


Figure 6.8: Evolution of stress in time during an adhesion test for AR 2 adhesives of (a) Type 1 and (b) Type 2. Preload of 0.18 MPa greater than the critical stress ($\sigma_{critical}$) is reached. Kink in stress at buckling and unbuckling is shown. Kink at buckling reversal (*i.e.* unbuckling) is absent for Type 1. Positive stress indicates compression with a maximum as the "preload stress" and negative stress indicates tension with a minimum as "pull-off strength".

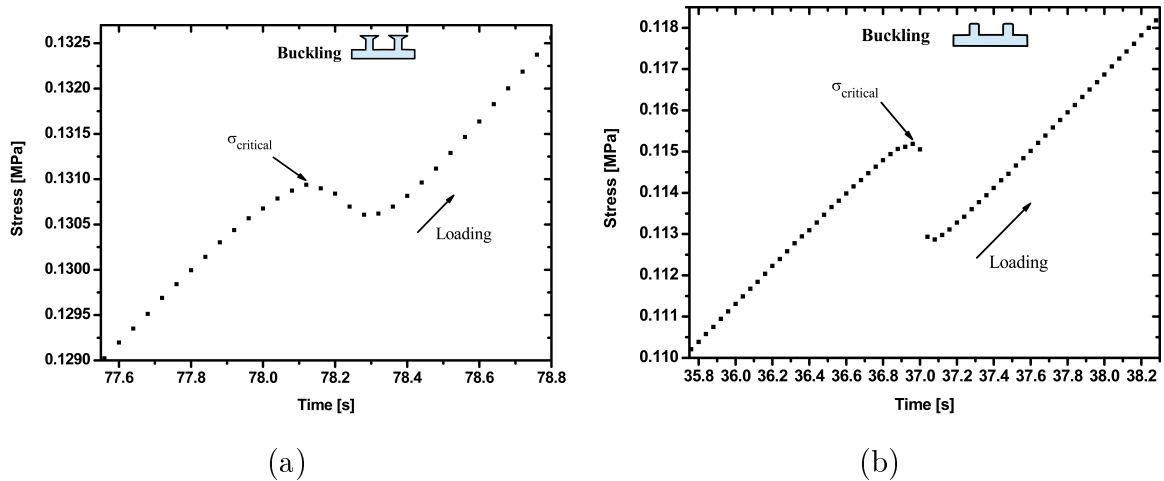


Figure 6.9: Critical stress ($\sigma_{critical}$) at *buckling* shown zoomed in from the loading parts of the curves in Figure 6.8 for (a) Type 1 and (b) Type 2 adhesives. A smaller kink at buckling for Type 1 is seen compared to that for Type 2.

When the preload reached a certain critical value, a *kink* in the stress was observed during the *loading* (Figure 6.8). Stress corresponding to the kink during loading was taken to be

the *buckling stress* ($\sigma_{critical}$). For example, $\sigma_{critical}$ was measured to be ≈ 0.13 MPa for Type 1 at 78.1 s and ≈ 0.12 MPa for Type 2 at 37 s for AR 2 adhesives from the inflection in stress during loading to a preload stress of 0.18 MPa (Figure 6.9 (a) and (b)). Type 1 adhesives exhibited a small stress change (0.3 KPa) and a gradual slope change at the buckling compared to the change in Type 2 adhesives (2.3 KPa) (Figure 6.9 (a) and (b)).

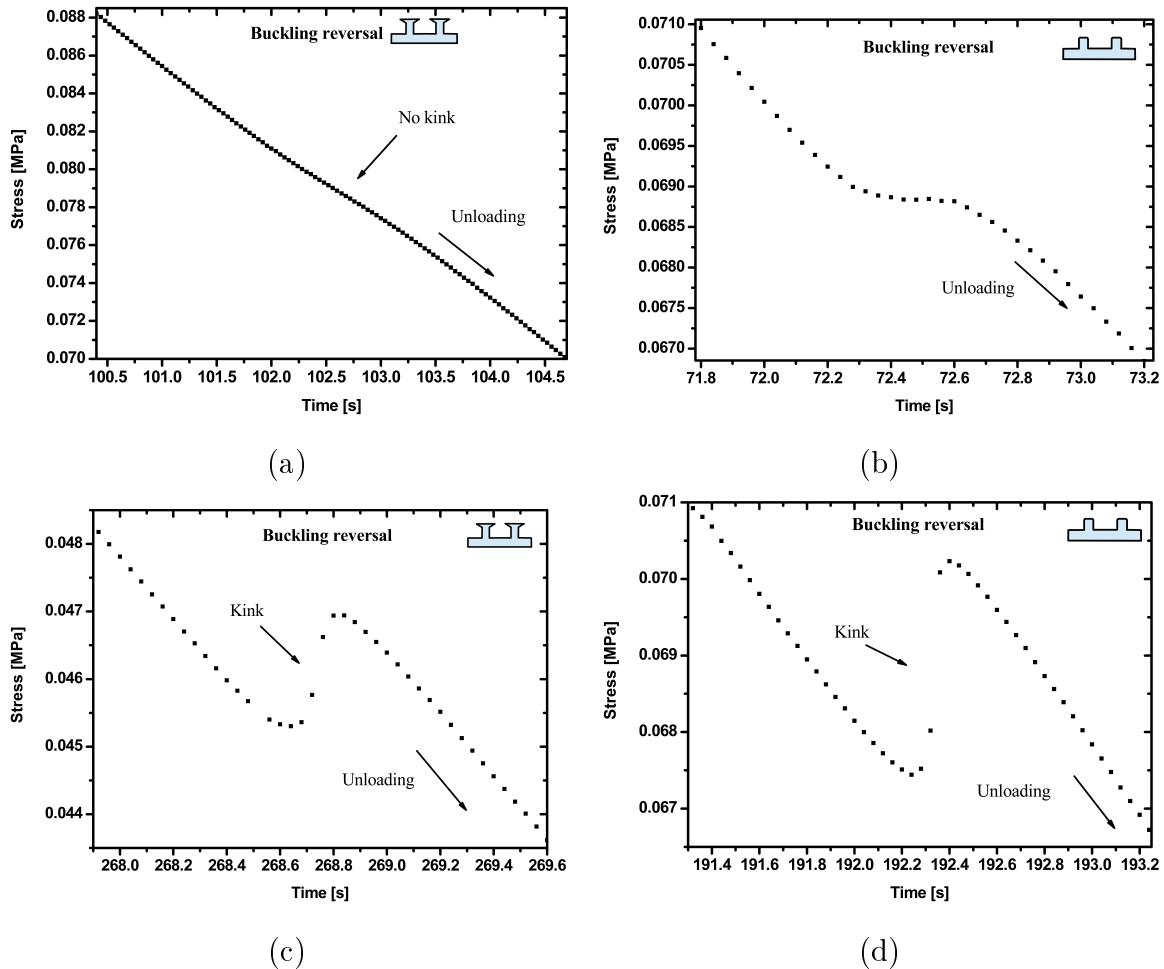


Figure 6.10: Critical stress at *buckling reversal* (or unbuckling) shown zoomed in from the unloading parts of the curves in Figure 6.8 for (a) Type 1 and (b) Type 2 adhesives. No kink is seen for Type 1 adhesives, whereas a step like change in stress is observed for Type 2 adhesives during reversal of buckling from the preload of 0.18 MPa. In comparison, buckling reversal from a high preload stress of 0.5 MPa is dominated by large kinks in stress for (c) Type 1 and (d) Type 2 adhesives.

The *unloading* from the preload stress 0.18 MPa showed reversal of buckling (Figure 6.10).

Whereas a gradual change in stress, without a kink, was characteristic for Type 1 adhesives (Figure 6.10 (a)), Type 2 adhesives exhibited a step like change in stress at buckling reversal (Figure 6.10 (b)). Furthermore, it was observed that for an *unloading* from a high preload stress of 0.5 MPa, larger kinks appeared at buckling reversal for both adhesive types (Figures 6.10 (c) and (d)).

Table 6.2 summarizes the measured critical stresses ($\sigma_{critical}$) as well as the adhesion loss stresses (σ_{loss}) for both types of adhesives.

Aspect ratio	$\sigma_{critical}$ [MPa],	σ_{loss} [MPa],	$\sigma_{critical}$ [MPa],	σ_{loss} [MPa],
	Type 1	Type 1	Type 2	Type 2
1.4	0.21±0.002 MPa	0.47 MPa	0.15±0.006 MPa	0.16 MPa
2	0.13±0.003 MPa	0.56 MPa	0.11±0.003 MPa	0.13 MPa
2.4	0.11±0.001 MPa	0.25 MPa	0.10 ± 0.01 MPa	0.10 MPa

Table 6.2: Observed critical ($\sigma_{critical}$) and loss stresses (σ_{loss}) for Type 1 and Type 2 adhesives.

6.3.3 Video results

Reversible buckling was observed *in situ* for the adhesion tests. Figure 6.11 and Figure 6.12 show video snapshots for Type 1 and Type 2 AR 2 adhesives, respectively, for similar preload stress (≈ 0.18 -0.2 MPa).

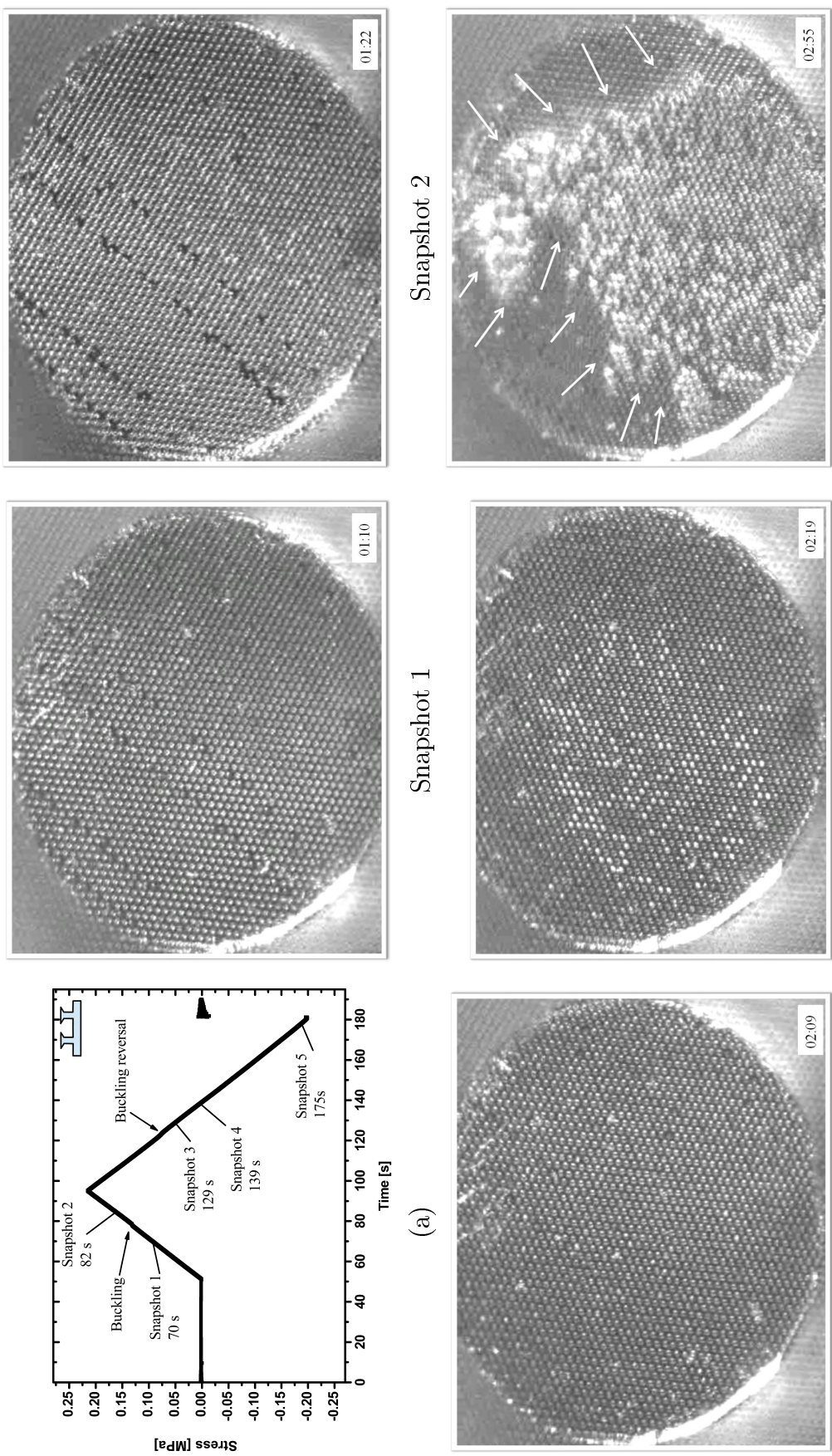


Figure 6.11: Reversible buckling for Type 1 AR 2 adhesives. (a) Stress-time plot with marked points corresponding to video snapshots at given times: Snapshot 1 -fibril tips in full contact. Snapshot 2 -fibrils in side contact after buckling. Snapshot 3 - fibril tips back in contact upon buckling reversal. Snapshot 4 -localized bright spots near center. Snapshot 5 -partial detachment before pull-off with arrows marking detachment front (black spots are defects on probe surface).

Figure 6.11 (a) shows the stress-time plot with changes in stress at *buckling* and *unbuckling*. Different points on the curve correspond to the video snapshots at the given times. Prior to buckling, fibril tips are in full contact, Snapshot 1. Fibril contact transition from top to side contact occurred concurrent to buckling. Fibrils maintained side contact (snapshot 2) till the desired preload stress was reached. The side contact was retained throughout the unloading until a smooth buckling reversal or an unbuckling event with a kink followed.

After the buckling reversal, fibril tip re-formed contact (snapshot 3). Immediately after the fibril contact transition from side to top, series of localized bright spots appeared and disappeared over a period of around 10 s. These spots appeared first along the circular contact edge of the probe and proceeded towards the center. Snapshot 4 captures some bright spots near the center of the contact area. These were taken as indicators of the end-flaps themselves unfolding. Subsequently, unloading proceeded into tension and a detachment front was observed to proceed from the top edge of the contact as indicated by the arrows in snapshot 5. Type 1 adhesives showed high pull-off strength after undergoing reversible buckling in case of the preload stress of around 0.2 MPa.

Similarly, Figure 6.12 shows the reversible buckling process followed by detachment at low pull-off strength for Type 2 AR 2 adhesive. Note that the Type 2 fibrils with their round edges do not exhibit any bright spots after the buckling reversal. Additionally, the buckling reversal occurred in the form of a distinct unbuckling event with a kink at the corresponding location in stress (Figure 6.12)

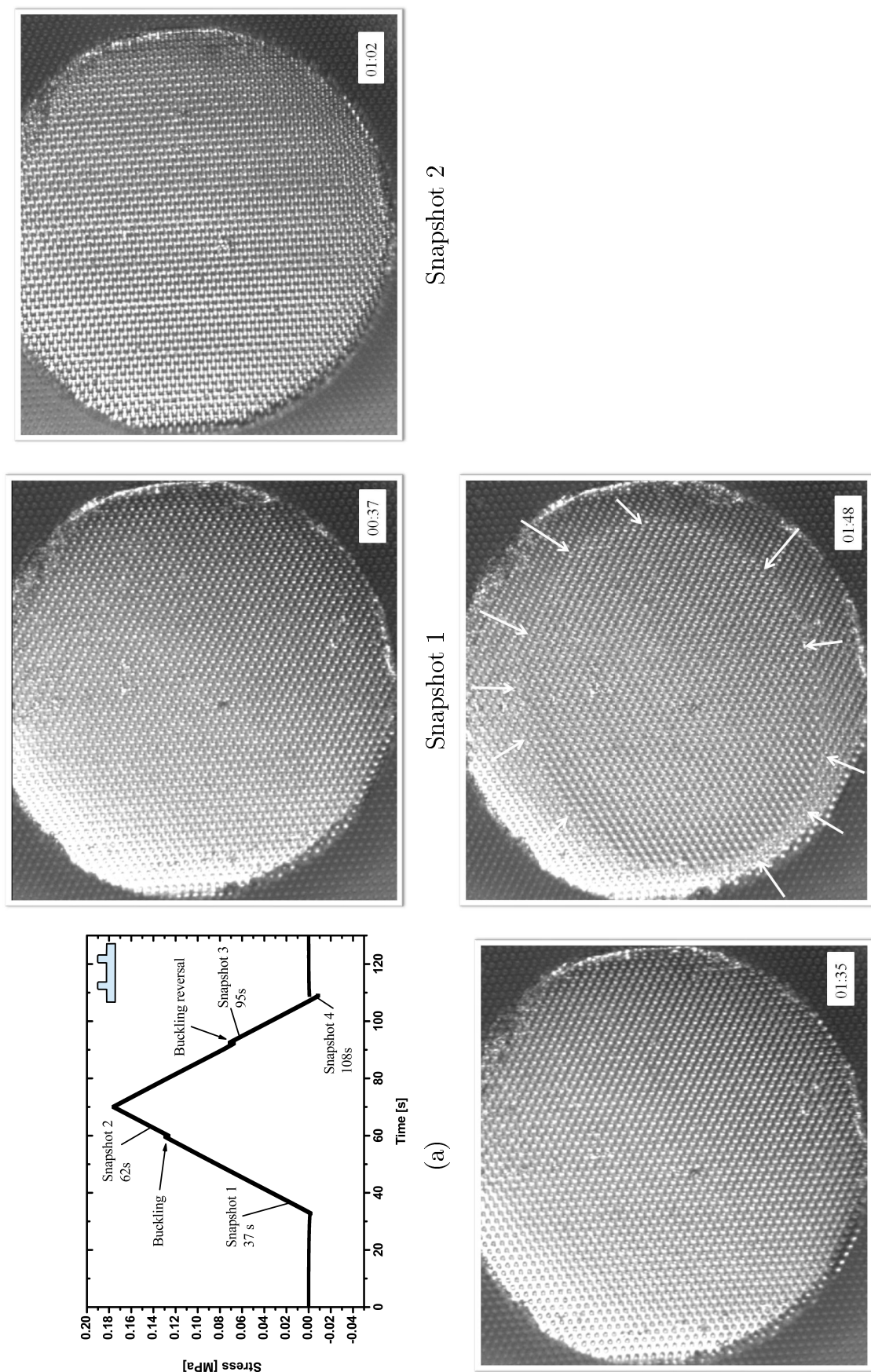


Figure 6.12: Reversible buckling for Type 2, AR 2 adhesives. (a) Stress-time plot with marked points corresponding to video snapshots at given times: Snapshot 1 -fibril tips in full contact. Snapshot 2 -fibrils in side contact after buckling. Snapshot 3 -fibril tips back in tip contact upon buckling reversal. Snapshot 4 -partial detachment before pull-off (arrows mark detachment front).

6.3.4 End-flap orientation

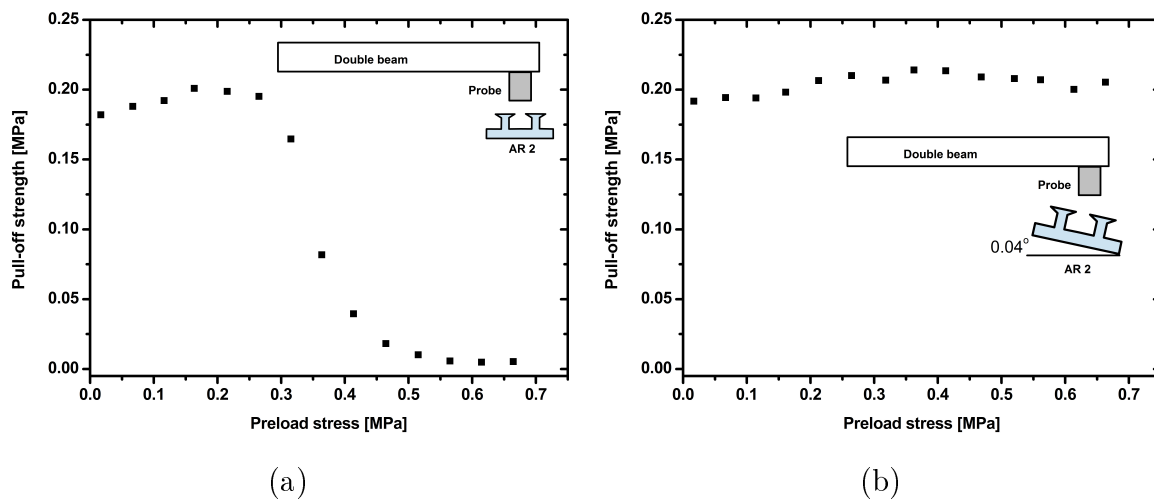


Figure 6.13: Sample alignment affects adhesion in Type 1 adhesives. (a) Adhesion loss and (b) no adhesion loss for the same set of preload stress for AR 2 Type 1 adhesives. Inset: schematic representation of sample in (a) "aligned" state and (b) tilted "away" by 0.04° with respect to probe-double-beam.

Figure 6.13 shows the effect of sample alignment on adhesion for Type 1 AR 2 adhesives. When the sample was tilted with respect to the probe (mounted on double beam spring), *away* from the aligned orientation (6.2.3.2), adhesion response at high preload stresses was different (Figure 6.13 (a) and (b)). The orientation of the fibrils with end-flaps was changed from the aligned state to a tilted state of 0.04° as shown schematically in the inset in Figure 6.13 (a) and (b). The result of no adhesion loss was reproducible everywhere on the sample (see Appendix II, Figure 8.6). However, it was noted that a change in alignment in the opposite direction (towards probe-double-beam) did not show a symmetric change in adhesion. Type 2 adhesives failed to show any drastic changes in the stress at which loss in adhesion occurred when tested for different sample alignments (see Appendix II, Figure 8.7).

6.4 Discussion

At the outset, based on Euler-Bernoulli buckling formulation for a beam, we had anticipated that by changing the aspect ratio of the fibrils the stress at which switching of adhesion occurs may be modified. Results indicate that such an effect was indeed observed as drops in pull-off strengths (adhesion) were measured at preload stresses which were lower for higher aspect ratio samples. However, there are important distinctions between the two types (1 and 2) of adhesives with respect to:

1. The stress at which buckling occurred ($\sigma_{critical}$) for different aspect ratios.
2. The stress at which adhesion loss (σ_{loss}) occurred while keeping AR constant (Table 6.2).
3. Pull-off strength maxima as a function of aspect ratios (Figures 6.7).
4. Dependence of adhesion loss stress (σ_{loss}) on sample alignment (Figure 6.13).

The discussion aims to address these four points.

6.4.0.1 Point 1: Fibril buckling

The measured critical stress per pillar was compared with the calculated critical stress assuming Euler-Bernoulli buckling. The critical force for buckling of a beam according to Euler-Bernoulli theory is given by Equation 6.2 [Timoshenko1961]:

$$F_{crit} = \frac{n^2 \pi^2 EI}{h^2}, \quad (6.1)$$

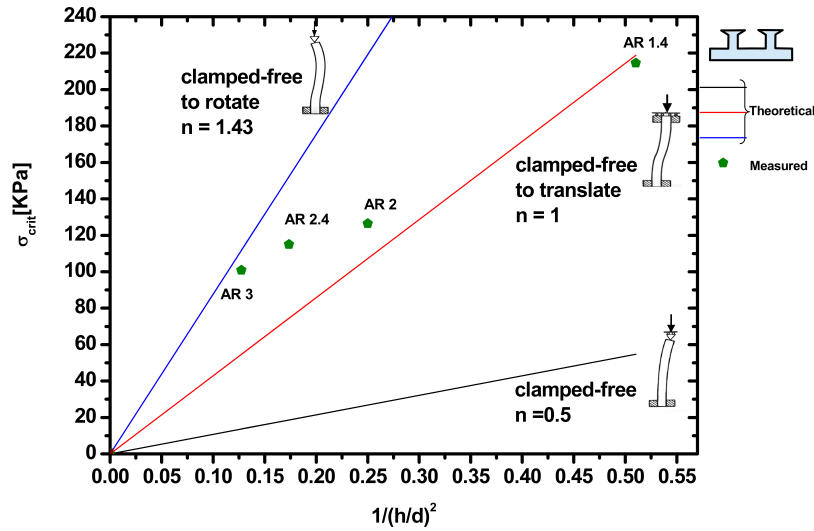
alternatively,

$$\sigma_{crit} = \frac{n^2 \pi^2 E}{16} \frac{1}{(h/d)^2}, \quad (6.2)$$

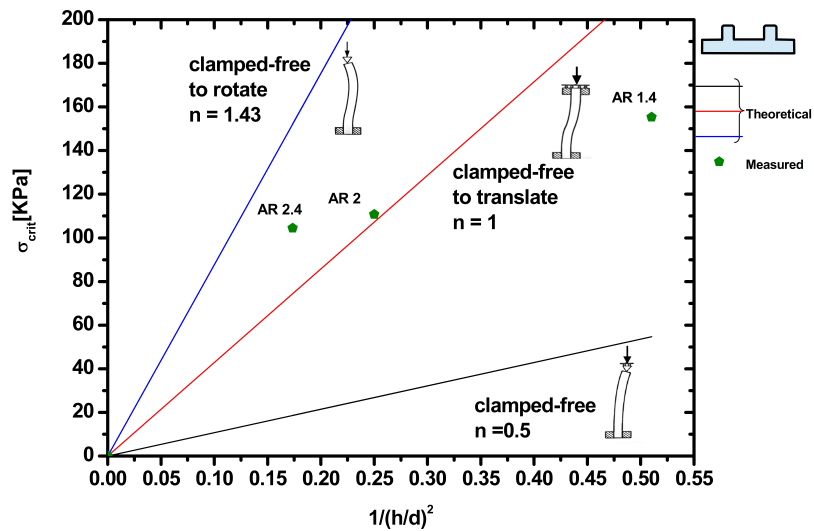
where E is the Young's modulus of the fibril, I is the second moment of area, $I = (d^4/64)$ for a circular cross-section with diameter d , and h is the length of the pillar. The pre-factor, n is the half-wavelength of the buckled shape and takes different values depending on the end constraints on the fibril. The hexagonal packing of the fibrils (area fraction of 22.67%)

was accounted for by modifying the Equation 6.2 in order to estimate the theoretical stress per pillar:

$$\sigma_{crit} = \frac{n^2 \pi^3 E}{128 \sqrt{3}} \frac{1}{(h/d)^2}. \quad (6.3)$$



(a)



(b)

Figure 6.14: Theoretical Euler buckling stress (lines) and measured critical stress (points) per pillar for (a) Type 1 and (b) Type 2 adhesives plotted as a function of $1/(h/d)^2$ following Equation 6.3. The slopes of the lines represent the different end-constraints on the fibril, n schematically depicted in the thumbnail sketches.

Figures 6.14 (a) and (b) show the comparison of the experimental critical stress (points) with those predicted by Euler buckling theory (straight lines) for the two adhesive types². The different lines represent the theoretical buckling stresses for different end-constraints (*i.e.* pre-factor n) on fibrils. In our case one end of the fibril is always clamped *i.e.* fixed at the backing but the other end may be: (1) Free to translate or rotate ($n = 0.5$) or (2) Free to translate but not rotate ($n = 1$) or (3) Free to rotate but not translate ($n = 1.43$). Depending on the nature of the probe (spring-like, stiff etc.) and the adhesion between the fibril and the probe the end-constraint may change between $n = 1$ to $n = 1.43$.

The elastic modulus for the theoretical critical stress, calculated using 6.3 was assumed to be $E \approx 3.4$ MPa based on experiments. The slope of the load-displacement curve helps estimate the total stiffness of the fibrils and the backing (see Chapter 7). Results appear to follow the Euler buckling theory: Higher AR fibrils buckled at lower stress. Measured $\sigma_{critical}$ for all aspect ratios appear to be slightly higher than the theoretical stress for the end constraint of $n = 1$. Prior to buckling, the fibrils are constrained at both ends, at one from the backing and at the other from the adhesion with the probe. Forces applied need to overcome the fibril-probe adhesion before top contact is lost upon buckling. Under these conditions the slightly higher measured critical stress than those predicted by theory under $n = 1$ may be understood. This result is consistent with the theoretical study of Stark, Begley and McMeeking [Stark2012]. It is noted that Euler buckling theory predicts critical loads for long, slender fibrils ($h \gg d$, $AR > 7$) and under no shear forces. In the view of the relatively low AR of fibrils used in this work and the spring like test surface of a flat probe, both of these basic conditions are not strictly followed. Therefore, results may only be qualitatively compared.

Exceptionally high critical stresses were measured for samples with AR 1.4 (see Figures 6.14). The adhesion strength was also notably high compared to other ARs of Type 1 adhesives (see Figure 6.7) which meant that breaking of the tip-probe interface was more difficult. This caused an increase in experimentally measured $\sigma_{critical}$. Compared to other fibrils, the

²For Type 1 adhesive an extra point corresponding to measured critical stress for AR 3 is included. The Type 1 adhesive with AR 3 was studied for mechanical instability induced adhesion switching in Chapter 4.

AR 1.4 fibrils are relatively stubbier and can hardly be considered as beams, which explains the greater disagreement with theory.

For comparable aspect ratios, the round edged fibrils show lower measured critical stress compared to the fibrils with end-flaps. This was consistent with the much lower adhesion of the Type 2 adhesives, implying an easier interface failure due to round edges as defects [McMeeking2008].

6.4.1 Point 2: Stresses for adhesion loss

Comparing $\sigma_{critical}$ with σ_{loss} from Table 6.2 for Type 1 adhesives, it is clear that fibril contact transition need not necessarily result in an adhesion loss as was previously reported [Peressadko2004], [Hui2007]. Type 2 adhesives, in contrast, do not show a significant difference between $\sigma_{critical}$ and σ_{loss} .

Figure 6.15 compares Type 1 and Type 2 adhesives for the buckling stress ($\sigma_{critical}$) and the adhesion loss stress (σ_{loss}) for samples with AR 2. Figure 6.15 (a) shows the difference between the $\sigma_{critical}$ of 0.13 MPa and the σ_{loss} of 0.56 MPa for Type 1 adhesive. All data points beyond 0.13 MPa (shown in blue) are pull-off strengths measured for preload stresses which were greater than $\sigma_{critical}$. These stresses, therefore, each caused *reversible buckling* to occur yet the adhesive responses are not negligible. In contrast, for the Type 2 adhesives $\sigma_{critical}$ (0.11 MPa) and σ_{loss} (0.13 MPa) were very close and the intermediate pull-off strengths were absent. This discrepancy is discussed here exploring the nature of fibril contact transition upon buckling reversal.

6.4.1.1 Stress regime 1

Stress regime 1 is defined by the *preload stress just above buckling stress* ($\sigma_{critical}$) (for preload stress between 0.13 MPa and 0.28 MPa, Figure 6.15 (c)). In this regime Type 1 adhesives retained high pull-off strength, whereas adhesion dropped drastically for Type 2 adhesives. It is postulated on the basis of *in situ* video results that after the fibril contact transition, the end-flap (of Type 1 adhesives) itself folded taking either of the two configurations as

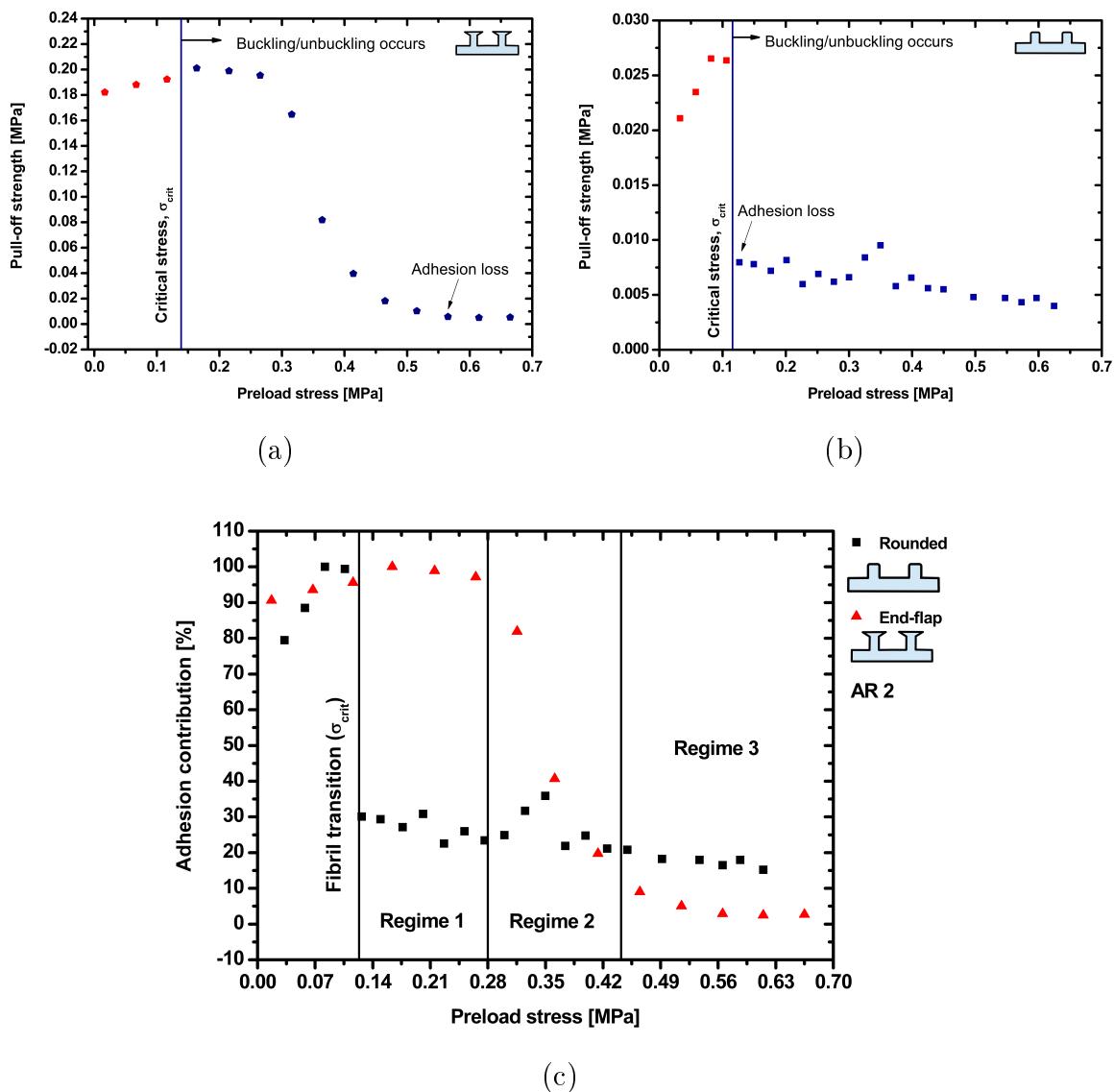


Figure 6.15: Critical stresses ($\sigma_{critical}$), marked by a vertical boundary, and adhesion loss stresses (σ_{loss}) shown for adhesives with AR 2 of (a) Type 1 and (b) Type 2 on the pull-off strength versus preload stress plot. Adhesion loss for Type 1 occurred at much higher stress compared to Type 2, which showed loss concurrent to preload stress exceeding critical stress. (c) Adhesion contribution (percent of the maximum adhesion strength) as a function of preload stress for both adhesive types. Stresses slightly greater than critical are defined by Regime 1, intermediate stresses by Regime 2 and very high preload stress by Regime 3. illustrated in (a) and (b) Figure 6.16.

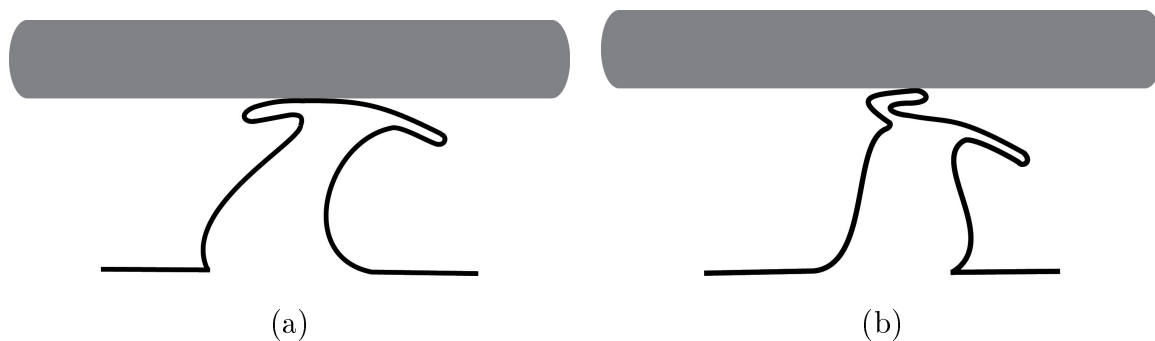


Figure 6.16: Schematic based on video data showing two possible configurations for end-flap folding during the fibril contact transition at loading. Configuration 2 appeared more probable for stresses in regime 1 as the videos of the unloading contact transition showed optical changes in brightness just *after* the fibrils regained vertical shape (Figure 6.11). Unfolding from configuration 2 was thought to cause these visual changes as the shiny surface of the probe was briefly visible as bright spots during the flap unfolding. Bright spots disappeared after the interface was sealed upon completion of unfolding.

When the fibril contact transition during loading was complete, the fibrils lay prone between the test probe above and the backing below. Increasing compressive stress almost always enforced the folded end-flap configuration shown in sequence (b) (confirmed by *in situ* video analyses Figure 6.11). The folded end-flap thus maintained a link between the fibril top and the probe. Such a link is proposed to be crucial for re-establishing a smooth contact during unloading. After the reversal of fibril buckling the end-flap unfolds assisting the fibril contact re-formation. Unfolding was thought to cause the visual changes described in the videos (Figure 6.11) as the shiny surface of the probe was briefly visible (bright spots) before the flap re-sealed the interface. This is in agreement with the a smaller kink or even absence of it altogether in the stress during unloading for the Type 1 adhesives when compared with that of Type 2 (Figure 6.10 (a)). The folding of end-flaps under compression was previously observed by Varenberg and Gorb [Varenberg2008] for similar tip shapes. In their case, the end-flaps were in the form of a more pronounced mushroom like shape than the present case. The folding-unfolding behaviour of the end-flaps, together with their superior contact adaptability [Carbone2011], may explain the high adhesion in spite of the reversible buckling. In contrast, Type 2 adhesive fibrils with round edges lost the top contact entirely when

they buckled. When the buckling reversed during unloading, the round edges acted as circumferential defects which hinder smooth sealing of the interface during the fibril contact re-formation. This led to the observed larger kinks in stress at unbuckling during unloading (Figure 6.10 (b)). Hence, Type 2 adhesives showed adhesion loss for all preload stresses above the buckling stress ($\sigma_{critical}$).

6.4.1.2 Stress regime 3

Stress regime 3 is defined by *very high preload stress* (≥ 0.45 MPa, Figure 6.15 (c)). In this regime the Type 1 adhesives having AR 2 also showed negligible adhesion. Type 2 adhesives continued to show low adhesion as observed earlier for regime 1.

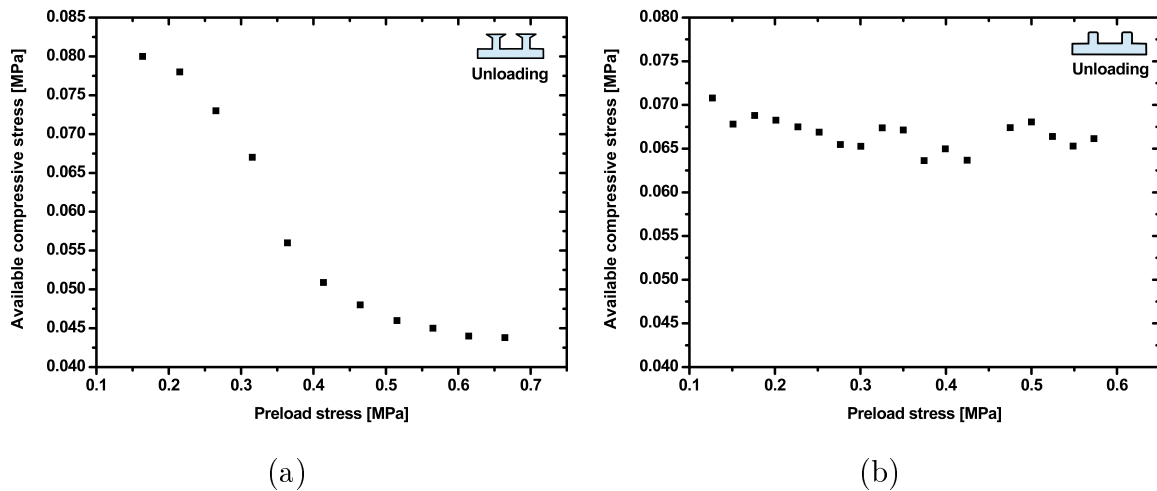


Figure 6.17: Compressive stress available at buckling reversal for (a) Type 1 and (b) Type 2 adhesives for the same range of preload stress. Type 1 adhesives at high preload stress (>0.45 MPa) exhibit buckling reversal at lower compressive stresses.

A systematic lowering of the stress at which buckling reversed during the unloading was noted as a function of the preload stress only for Type 1 adhesives (Figure 6.17 (a)). This in turn meant that the unfolding of the end-flap, which occurs just after unbuckling had much lower compressive stress available for contact re-formation. *In situ* observations confirmed these changes in the form of changes in the series of bright spots after the unbuckling. Compared to the slow localized manner of their appearance and disappearance over a period of 10s for the low preload stress (regime 1, Figure 6.11), a rapid wave swept across the contact area in

just 3 s for the high preload case (see Appendix, Figure 8.4). The unbuckling event showed a characteristic large kink in stress for the preloads in regime 3. Such a kink was indicative of an abrupt fibril contact transition from the prone to the vertical state. Once vertical, the lack of sufficient compressive stress hindered the end-flap's ability to form an intimate contact when it unfolded. The resultant drastic loss in contact area was responsible for the adhesion loss.

For Type 2 adhesives, in contrast, fibril transition stress during unloading did not vary much (Figure 6.17 (b)).

6.4.1.3 Stress regime 2

Stress regime 2 is defined by an intermediate preload stress between regime 1 and 3 (for preload stress between 0.3 and 0.45 MPa, Figure 6.15 (c)). In this regime, adhesion for Type 1 adhesives falls from high to low values, whereas Type 2 adhesives continue to show low adhesion as in the previous cases. The compressive stress available to re-form intimate contact when the end-flap unfolds decreased systematically. This is because the buckling reversal itself occurred at much lower compressive stress as a function of preload stress (Figure 6.17 (a)). When the preload stress was on the lower side (≈ 0.3 MPa), the end-flap unfolding enabled contact re-formation and led to observed adhesion. However, for higher preload stress of around 0.45 MPa, the end-flap unfolding occurred under low compressive stress with not enough time to re-form contact. Thus, a high fraction of fibrils regain intimate probe contact around lower preload stress, which changes to a lower fraction of fibrils able to re-form contact at higher preload stress. The number of fibrils able to re-form contact will be determined by the stochastic manner of end-flap unfolding characteristic of a given preload stress within the regime 2.

6.4.2 Point 3: Adhesion Strengths and aspect ratio

Generally, it is expected that higher AR fibrils, owing to their increased compliance, show higher pull-off strength [Greiner2007]. However, the maxima in the pull-off strengths,

recorded for different aspect ratios of Type 1 adhesives did not follow any general trend. This is attributed to the minor variations in the shapes and sizes of the end-flaps. The end-flap contact shape considerably enhances adhesion [delCampo2007]. A compliant fibril on a soft backing layer can further benefit from additive compliance of an end-flap. A mushroom shape tip was shown to significantly reduce stress concentration at the edges [Spuskanyuk2008]. Thus it was expected that even lower AR fibrils may show higher adhesion. The differences in the dimensions of the end-flaps for different ARs (see Table 6.1) due to the process variability appear to dominate adhesion effects more than the compliance changes by AR variation.

The Type 2 adhesives follow the general trend of higher adhesion for high aspect ratio samples as discussed previously by Greiner *et al.* [Greiner2007] and Glassmaker *et al.* [Glassmaker2004]. The maximum pull-off strength of AR 2 and 2.4 was, however, very similar. Repeated adhesion tests showed that the maximum in adhesion for AR 2.4 was 0.021 ± 0.0013 MPa whereas for AR 2 was 0.02 ± 0.003 MPa. The measured compliance for AR 2.4 (≈ 0.32 m/mN) were around 30% higher than those for AR 2 (≈ 0.25 m/mN) samples. It appears that such a small increase in compliance is insufficient for any significant raise in adhesion for the given defect size of round edges (radius of curvature $1.86 \mu\text{m}$). However, fabrication related differences in the edge rounding cannot be ruled out due to the nature of the surface tension driven rounding. These may explain the variations in the maximum in adhesion strengths between samples of the same AR.

6.4.3 Point 4: Sample alignment

When the alignment of the Type 1 samples was changed from the *aligned* state to *away* from the flat probe-double-beam, no adhesion loss even at very high preloads was observed (Figure 6.13). In the new orientation, smaller kinks in stress were observed during the unloading and the resultant contact re-formation by the end-flaps was similar to that for regime 1. Tilting of the fibrils away from the probe effectively orients the end-flaps such that the contact of the top face may be retained over the entire loading-unloading (see Figure 6.16 (a)). Thus by changing the sample alignment, for the same high preload stress, both low

as well as high adhesion states are achievable. The change of sample alignment *towards* the probe-double-beam did not produce a symmetric response. This can be partly attributed to the unsymmetric nature of the double beam spring (clamped on one side), but is not fully understood (see Appendix II, Figure 8.6 (c) and (d)). Different sample alignments for Type 2 adhesives with round edges failed to show a drastic adhesion response as a function of preload stress (see Appendix II, Figure 8.7). The maxima in pull-off strength was lower in the "misaligned" state, consistent with the previous result [Kroner2011].

6.5 Summary

A visual summary of the contact mechanisms during the processes during the reversible buckling of fibrils for which Type 1 adhesives re-form contact and show high adhesion is presented in Figure 6.18.

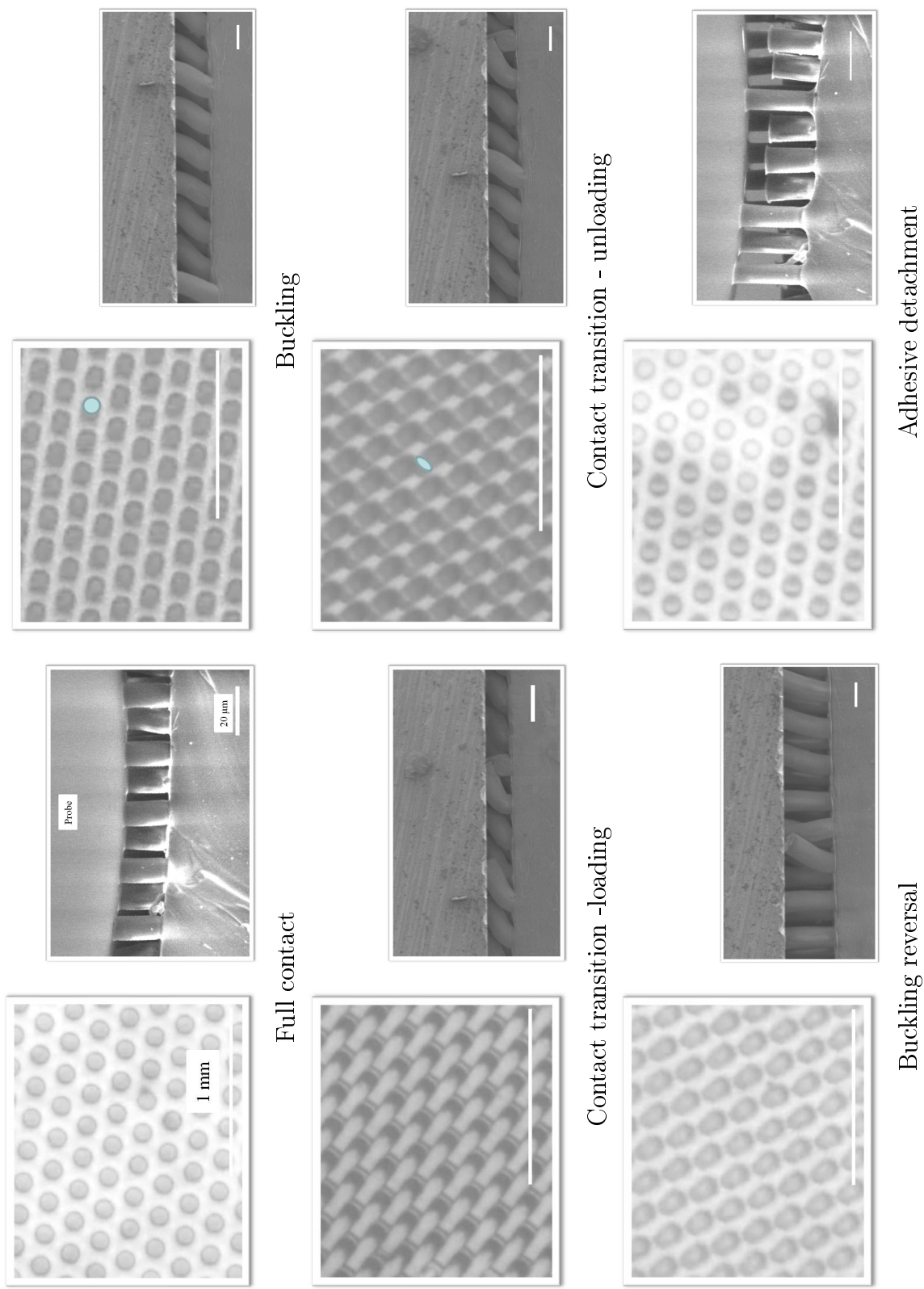


Figure 6.18: Visual summary of contact mechanisms during reversible adhesion. Blue spot drawn to guide the eye to follow the fibril tip.

6.6 Conclusions

Preload responsive adhesion was achieved by inducing buckling and loss of contact between the probe and the fibril tip. The mechanism of adhesion transition was investigated by studying the effect of the fibril's aspect ratio, tip shape and orientation (with respect to the flat test surface):

- Adhesives with higher aspect ratio fibrils showed adhesion loss at lower preload stress. Buckling of fibrils was observed *in situ* at preload stresses which followed Euler buckling theory. However, buckling was recognized to be reversible and it was found that the stress for adhesion loss (σ_{loss}) may not necessarily be the same as buckling stress ($\sigma_{critical}$). Fibril tip shape was responsible for the observed difference.
- Round tip shape acts as a circumferential defect which impaired contact re-formation upon buckling reversal of the fibrils. Hence any stress that caused fibrils of Type 2 to buckle resulted in an adhesion loss for these adhesives.
- Fibrils with end-flaps assist in tip contact recovery by themselves undergoing folding and unfolding during the reversible buckling processes. In addition, at moderate preload stress sufficient compressive stress was available after the buckling reversal to aid the contact re-formation. This led to reversible adhesion, which gradually decreased with increasing preload stress.
- Very high preload stress caused an adhesion loss even in fibrils with end-flaps (Type 1). Unbuckling event showed a characteristic large kink in stress at these preload stresses indicative of an abrupt fibril contact transition. In addition, the end-flaps unfold under insufficient compressive stresses after the buckling reversal. Hence, intimate tip contact re-formation was impaired and the resultant drastic loss in contact area was responsible for the adhesion loss.
- Systematic change in fibril orientation with respect to the probe affects adhesion switching for the fibrils with end-flaps. This was explained on the basis of the orientation dependent folding-unfolding of the end-flaps.

Chapter 7

Buckling of an adhesive micropillar¹

Abstract

Adhesion and buckling of a single micropillar as a function of preload was investigated. Micropillars had diameters of 10, 12, 14 and 20 μm and aspect ratios of 1 to 3.3. Adhesion generally increased with a decrease in the aspect ratio of the micropillar. The fibril stiffness and the edge radius of the tip which acts as a circumferential crack control the adhesion. Dependence of pull-off strength on the preload stress was noted for micropillars which underwent buckling. When buckling was reversible, tip contact recovered upon unbuckling, resulting in only a slight reduction in adhesion. *In situ* studies showed that the fibril's round edge and the adhesion contact hysteresis may cause the slight reduction. Irreversible buckling of the micropillar, influenced by the probe curvature, occurred when the tip contact failed to recover and the fibril side peeled against the probe without an unbuckling event. The lack of tip-contact re-formation resulted in adhesion loss. Fibril buckling was found to be consistent with the predictions of Euler buckling theory.

¹This chapter is in preparation as a full paper with co-authors M. Bartlett, R. McMeeking, A. Crosby and E. Arzt.

7.1 Introduction

Bioinspired adhesive surfaces generally consist of arrays of hundreds or thousands of micropillars on a soft backing as summarized in recent reviews [Kamperman2010], [Boesel2010], [Jagota2011]. These adhesives are tested by compressively loading them against a probe and unloading them in tension till detachment. An inherent multiplicity is the most obvious consequence on contact formation and separation when a surface is patterned with a fibrillar array. Numerous studies have investigated the influence of several different sample characteristics on the adhesion mechanisms *e.g.* the sample compliance [Jagota2002], [Persson2003], the backing layer compliance [Kim2007b], [Long2008], the tip shape of fibrils [delCampo2007], [Gao2004], the fibril radius and aspect ratio [Greiner2007], [Aksak2011], the orientation of the fibrils with respect to probe [Kroner2011] or the roughness of the probe [Persson2003a], [Hui2005], [Vajpayee2010]. The impression these results create is that different factors influence the adhesion mechanisms differently and often their combined influence is quite complex.

Modeling a single fibril [Tang2005], [Spuskanyuk2008] or the interactions among, at best, a few during attachment and detachment [Long2008], [Guidoni2010] provides only a qualitative picture of the intricate, multi-contact phenomena occurring in large arrays of micropillars. The situation is further complicated by the details of how loading and unloading is carried out, for *e.g.* the presence or absence of shearing motion and frictional effects [Autumn2006] or the type of probe (flat/spherical) used [Kroner2011]. In addition, micropillar fabrication leads to variations in their dimensions and to defects on their surfaces. This introduces stochastic effects into the phenomena of contact and adhesion when many fibrils are involved (see Chapter 5).

An important outcome of these observations and those of others ([Glassmaker2004], [Hui2007]) is that the collective interactions of many fibrils provides little insight into phenomena occurring at the single fibril level. Such phenomena include attachment and buckling under compression, fibril tip detachment during buckling, tip re-attachment upon unbuckling during unloading, and full detachment at the adhesion limit, all of which contribute to the

system's adhesive strength. The present study focuses on investigation of these mechanisms for a single polydimethylsiloxane (PDMS) micropillar. Previous experimental studies on single micropillar adhesion [Kroner2011a], [Aksak2011] or buckling [Hui2007] use fibrils with much larger dimensions than the micro-scale of current interest. The present study investigates single micropillars having diameters 10, 12, 14 and 20 μm and heights of 20 and 33 μm . The effects on fibril adhesion and buckling associated with an increase in the applied compressive preload will be studied with the aim of complementing our understanding of adhesion and buckling within arrays of bioinspired adhesives.

7.2 Experimental methods

Single microscale pillars with heights of 20 and 33 μm with diameters equal to 10, 12, 14 and 20 μm in each case were obtained. These PDMS micropillars were fabricated using photolithography and soft molding techniques. Lithography masks were designed such that a single hole within a square centimeter area was obtained by the use of a negative tone SU-8 resist.

7.2.1 Photolithography

SU-8 resists 2010 and 2025 (Micro Resist Technology, Berlin, Germany) were spin-coated on cleaned Si wafers (100 orientation, Crystec Berlin, Germany) to thicknesses of 20 and 33 μm , respectively (spin coater, Suss Microtech). The general photolithography steps for SU-8 resists were followed (Chapter 3). These steps of soft-bake, exposure, post-exposure bake and development were further optimized for obtaining single holes in SU-8, see Table 7.1.

7.2.2 Soft molding of single micropillars

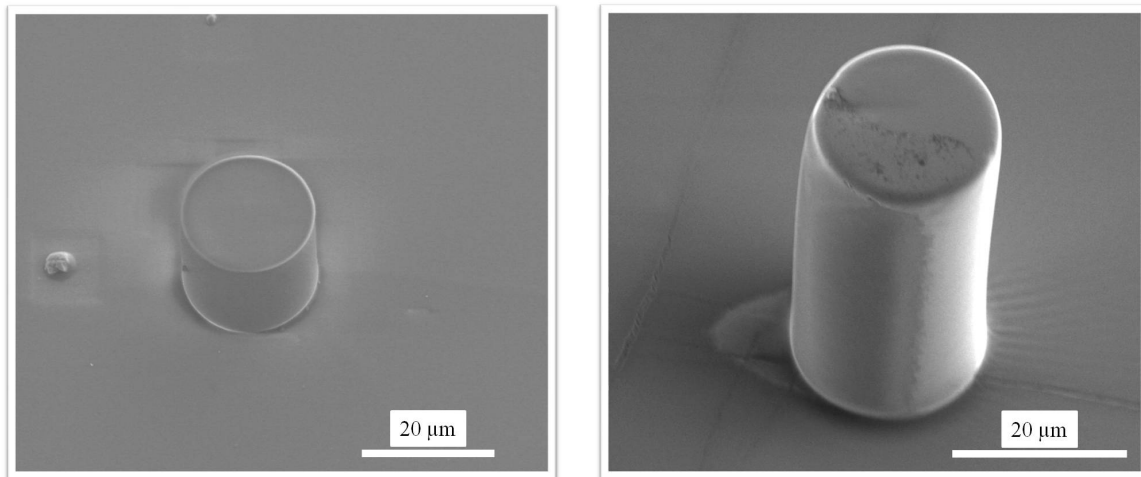
PDMS (10:1, prepolymer to cross-linker) mixture was prepared using the Dow Corning Sylgard 184 kit. The mixture was degassed and poured on silanized SU-8 masters. Upon

Process step	SU-8 2010	SU-8 2025
Soft bake: leveled hot-plate	5 min at 95 °C	5 min at 95 °C
UV exposure: stepper (Suss Microtech, Germany), lamp intensity $\approx 15mW/cm^2$	14.3 s	19.3 s
Post-exposure bake: leveled hot-plate	5.5 min at 95 °C	5.5 min at 95 °C
Developing in mrDev solution (Micro Resist Technology, Germany)	4 min	4.5 min

Table 7.1: Photolithography process details for obtaining single cylindrical holes in SU-8 resists.

curing for at least 14 h the crosslinked PDMS was carefully peeled-off from the SU-8 masters. Single micropillars of two different heights (20 and 33 μm) and diameters equal to 10, 12, 14 and 20 μm in each case were obtained. This led to a range of aspect ratios from 1 to 3.3.

7.2.3 Characterization of single micropillars



(a)

(b)

Figure 7.1: SEM images of low AR single micropillars with $d = 20 \mu\text{m}$ and (a) AR 1, $h = 20 \mu\text{m}$, (b) AR 1.6, $h = 33 \mu\text{m}$.

SEM micrographs of some low and high AR single micropillars are shown in Figures 7.1 and 7.2. Sometimes surface wrinkles in the PDMS backing were observed (Figure 7.2 (a))

and (b)) due to release of stress during molding between the stiff SU-8 and the soft PDMS. Some pillars appeared to be slightly bent in SEM micrographs. Defects like bent pillars are known to occur during the lithography process and may be attributed to the non-uniformity in UV exposure and thickness variations in SU-8 films. Multiple single micropillars of same dimensions resulted from a single mold and so bent pillars could be avoided for adhesion tests.

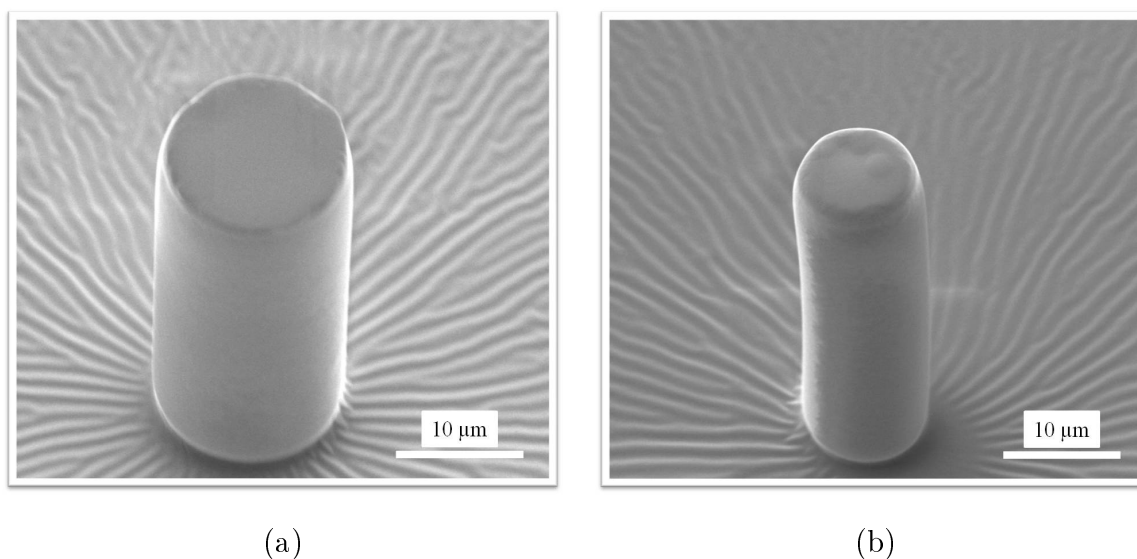


Figure 7.2: SEM images of high AR single micropillars. (a) AR 2.3, $h = 33$ and $d = 14 \mu\text{m}$, (b) AR 3.3, $h = 33$ and $d = 10 \mu\text{m}$.

The heights of the micropillars were confirmed optically by white light interferometry, Figure 7.3.

7.2.4 Adhesion testing

The adhesion experiments were conducted on a custom designed instrument *Contact Adhesion Testing Device* at the University of Massachusetts, Amherst, USA (Figure 3.6). The device consisted of a piezo-controlled linear actuator (Burleigh Inchworm nanopositioner) controlling the travel of the sample, a cantilever based capacitance force transducer, and a fully automated, inverted optical microscope (Zeiss Axiovert 200M) to visualize the contact interface during the test. The total instrument compliance, which was mainly due to the cantilever, was $3925 \mu\text{m}/\text{N}$ (at least 10 times stiffer than the sample). Each component was

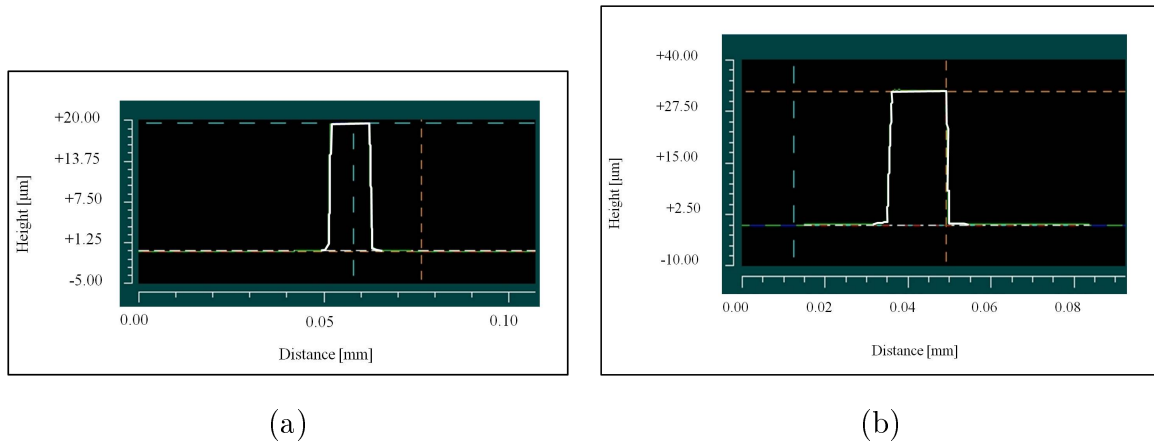


Figure 7.3: White light interferometry images of single micropillar profile. (a) $h = 20 \mu\text{m}$, $d = 10 \mu\text{m}$ and (b) $h = 33 \mu\text{m}$, $d = 14 \mu\text{m}$.

controlled through custom-written software within a National Instruments Labview environment. The test procedure involved attaching the single fibril PDMS sample to the cantilever, which in turn was mounted on the linear actuator.

Adhesion was tested against a glass plano-convex lens (diameter 6 mm and radius of curvature 15 mm, Edmund Optics, USA) and a glass hemisphere (diameter 1 mm) fixed on the stage of the inverted optical microscope. The single fibril was compressed against the glass probe to varying preload stress (maximum compressive load divided by the undeformed pillar cross-section area) and was subsequently retracted until pull-off. Adhesion of the micropillar was recorded as the pull-off strength (maximum tensile load (or pull-off force) divided by the undeformed pillar cross-section area). During contact and separation, the displacement of the sample, the applied force and the contact area were continuously monitored and recorded. All experiments were performed at room temperature, and the displacement rate of the sample was $0.89 \pm 0.04 \mu\text{m/s}$.

7.3 Results

7.3.1 Pull-off strength as a function of preload stress

Figure 7.4 shows the pull-off strength as a function of the preload stress for single micropillars with height $h = 20 \mu\text{m}$ having different aspect ratios. Tests were carried out using a 6 mm diameter plano-convex glass probe. Increasing the preload stress had no significant effect on their pull-off strengths (Figure 7.4 (a)). Some fibrils showed unusually strong adhesion when tested repeatedly (see additional information in Appendix IV, Figure 8.9).

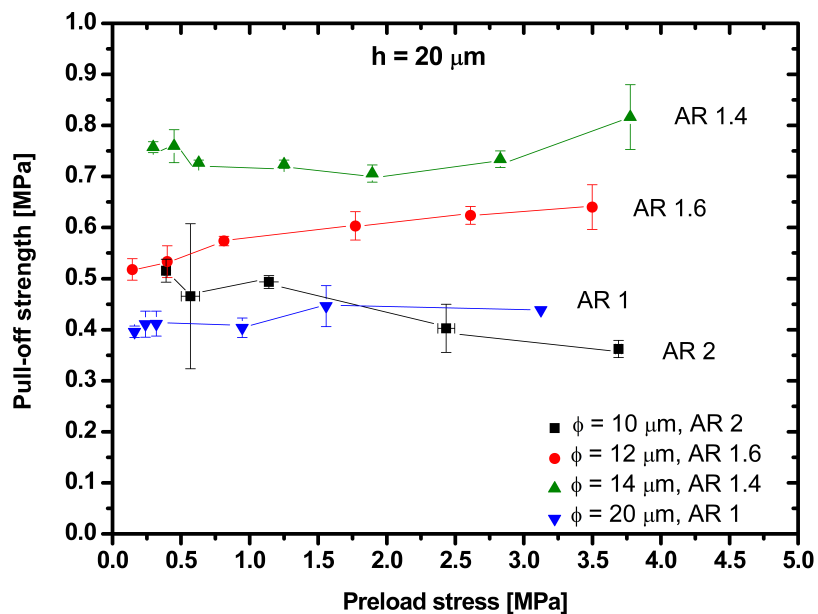
Figure 7.4 (b) shows the adhesive response to applied load for the taller micropillars. Fibrils having $h = 33 \mu\text{m}$ and high AR show pull-off strengths that decrease slightly as a function of preload stress. Adhesion for AR = 1 micropillar remained unchanged. In general, $h = 33 \mu\text{m}$ micropillars showed lower adhesion than the $h = 20 \mu\text{m}$ ones, for a given diameter, *i.e.* the same nominal contact area.

7.3.2 Buckling as a function of preload stress

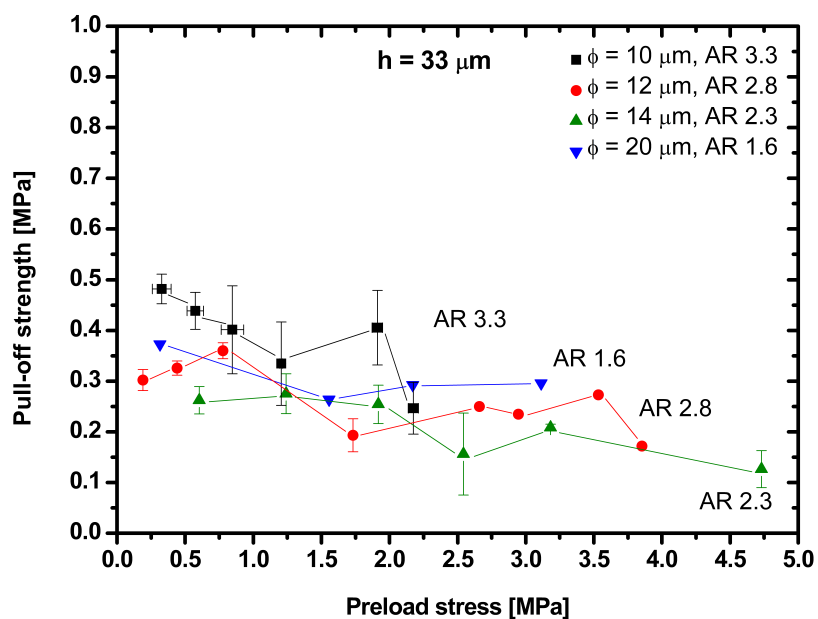
Micropillars of lower height of $20 \mu\text{m}$ did not show any buckling for the range of preload stress used. The taller, $33 \mu\text{m}$ micropillar samples with diameters of 10, 12 and $14 \mu\text{m}$ buckled at higher preload stress (0.8-2 MPa). Buckling corresponded to a slight lowering of adhesion. The contact mechanisms for both the low and high preload cases are presented here. Micropillar with AR 3.3 ($h = 33$ and $d = 10 \mu\text{m}$) is taken as a representative for this purpose.

7.3.2.1 Low preload: No buckling

Low preload stress ($\leq 0.6 \text{ MPa}$) applied using the 6 mm diameter plano-convex glass probe did not cause buckling in the AR 3.3 micropillar (Figure 7.5). Inset snapshots are provided above the plot and show the top view of the pillar-probe interface, revealing the characteristics of the contact. The time at which the snapshot was recorded is given in each inset.



(a)



(b)

Figure 7.4: Pull-off strength as a function of preload stresses for single micropillars with (a) $h = 20 \mu\text{m}$ and (b) $h = 33 \mu\text{m}$ having various aspect ratios. Error bars indicate the variations in the measured stress/strength from at least three test repetitions.

Insets 1 and 5 in Figure 7.5 show the pillar tip not in contact with the probe (light gray circular spot) before and after the adhesion test, respectively. Insets 2 and 3 show the pillar tip in full contact with the micropillar under compression (dark gray circular spot). Inset 4 shows the pillar tip in full contact with the probe prior to detachment with micropillar under tension. The pull-off strength was 0.44 ± 0.04 MPa.

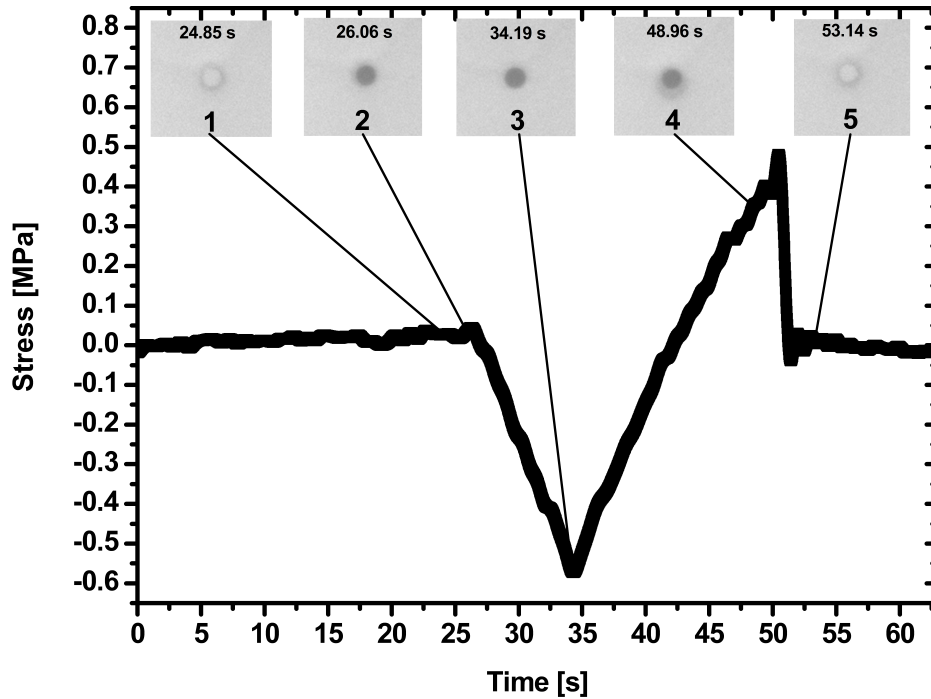


Figure 7.5: **No buckling** case: Evolution of stress in time during an adhesion test for a $10 \mu\text{m}$ diameter, $33 \mu\text{m}$ high (AR 3.3) single micropillar. The fibril is compressed to a relatively low preload stress of 0.6 MPa with the 6 mm plano-convex lens at constant velocity and then retracted at constant velocity. Compressive stress is negative and tensile stress is positive. Insets show the top view of the pillar-probe interface at the time indicated.

7.3.2.2 High preload: Reversible buckling

Figure 7.6 shows that a high preload stress of 1.25 MPa caused reversible buckling for the same micropillar-probe combination as above. Insets in Figure 7.6 and the accompanying side view renditions in Figure 7.7 show the contact mechanisms for the high preload case.

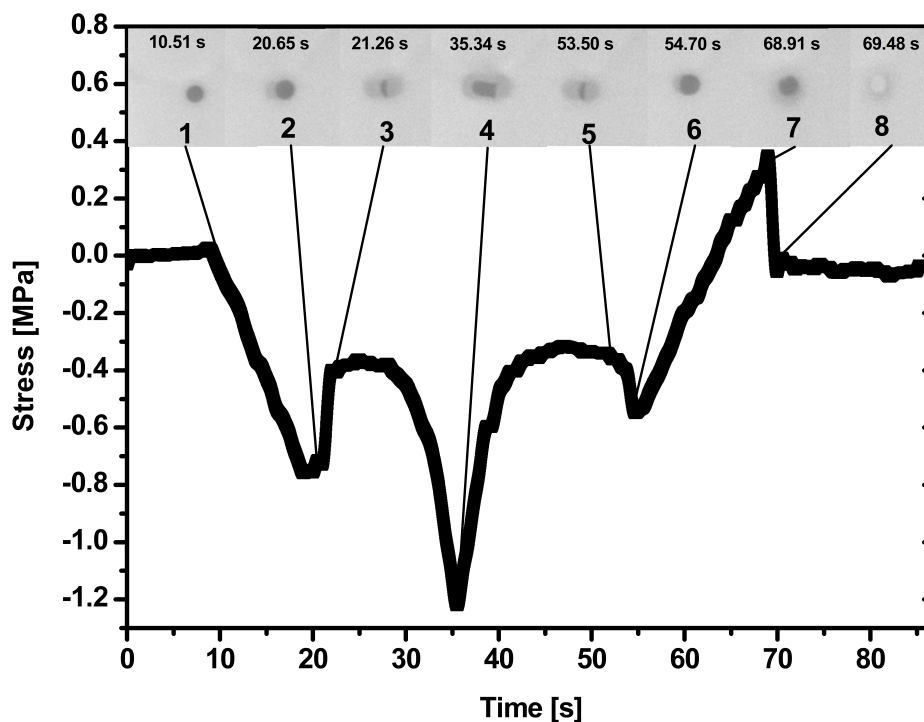


Figure 7.6: Case of **reversible buckling**: Evolution of stress in time during an adhesion test for a $10\ \mu\text{m}$ diameter, $33\ \mu\text{m}$ high (AR 3.3) single micropillar. The fibril is compressed to a relatively high preload stress of $1.25\ \text{MPa}$ with the $6\ \text{mm}$ plano-convex lens at constant velocity and then retracted at constant velocity. Inset pictures show pillar top and probe contact interface development in time.

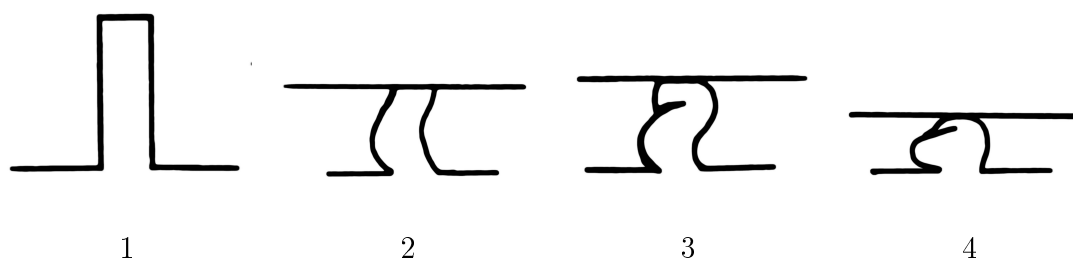


Figure 7.7: Schematic rendition of the side view configurations of a single micropillar corresponding to different stages of increasing preload stress (sketches 1 to 4 represent insets 1 to 4 in Figure 7.6).

During *loading*, the applied compression caused the pillar tip to come in full contact with the probe (inset 1). Insets 2 and 3 show a transition from a complete top face contact (dark gray circular spot, inset 2) to a partial side contact (dark gray moon-shape indicates fibril edge

and top face with lighter gray areas indicates fibril side, inset 3). The micropillar formed a hook shape at the stress of ≈ 0.75 MPa around $t = 20$ s (sketch 3, Figure 7.7). This change from tip to side contact was accompanied by a decrease in compressive stress indicating *buckling*. Inset 4 shows the pillar partially folded onto itself at maximum compressive load. In the side contact state the darker gray region indicates the elastically stretched fibril tip retaining partial contact (sketch 4).

During *unloading* the elastic stretch of the tip reversed (from inset 4 to 5). Further reduction in stress returned the fibril shape to almost exactly the same shape when first buckled (inset 5). Inset 5 and 6 show the fibril straightening from hook-shape back to full tip contact at around $t = 55$ s, indicating *reversal of buckling* or unbuckling. This event was accompanied by an increase in the compressive stress consistent with unbuckling. Inset 6 shows the fibril tip in full contact and the fibril being pulled into tension until detachment. Inset 7 and 8 capture the fibril tip immediately prior to and after detachment, respectively.

The pull-off strength in this case of *reversible buckling* was 0.33 ± 0.08 MPa. Note that without buckling (low preload case) the pull-off strength was higher, 0.44 ± 0.04 MPa. Similar observations were made for other micropillars that showed reversible buckling. For example, pull-off strength dropped from 0.35 MPa to below 0.2 MPa for the $12 \mu\text{m}$ diameter ($h = 33 \mu\text{m}$) micropillar when the preload stress exceeded 1 MPa causing reversible buckling (Figure 7.4 (b)).

7.3.2.3 Micropillar slippage: Irreversible buckling

When a hemispherical glass probe (radius of curvature 0.5 mm) was used instead of the plano-convex lens (radius of curvature 15 mm), the micropillars slipped during the unloading part of the high preload stress. Such slippage occurred only for a buckled pillar and during unloading from preload stress higher than the critical buckling stress.

Figure 7.8 shows the stress versus time plot for AR 3.3 micropillar tested using the 1 mm diameter hemispherical probe. Accompanying inset snapshots depict the pillar-probe interface. During *loading* to high preload stress, inset 1 captures the micropillar in a hook-shape

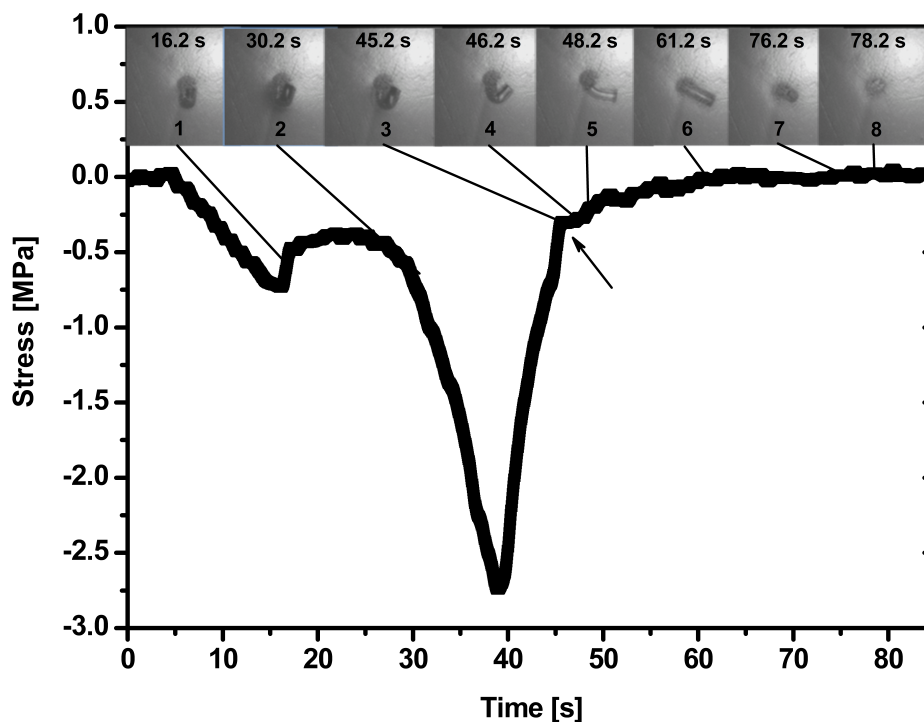


Figure 7.8: **Irreversible buckling** case: Evolution of stress in time during an adhesion test for a $10\ \mu\text{m}$ diameter, $33\ \mu\text{m}$ high (AR 3.3) single micropillar. The fibril is compressed to a relatively high preload stress of 2.8 MPa with the 1 mm diameter glass hemisphere at constant velocity and then retracted at constant velocity. Insets show the top view of the pillar-probe interface at the time indicated.

just after buckling, as in previous case. Further increase in compressive load resulted in slight bias of the hook-shape towards the right, inset 2. This bias may be due to the step-like motion of the piezo controller. At maximum compressive preload, the gap between the probe and the backing layer had closed so that the folded fibril was pinned between the probe and the backing layer.

During *unloading* the exact reversal in fibril configuration was not observed. As the load relaxed, the fibril tip slipped towards the bias direction collapsing sideways (inset 3 and 4). The stress-time plot showed a distinct change of slope around 44 s (arrow, inset 3) coinciding with the fibril collapse. The collapsed fibril adopted a single layer folded V-shape different from the double layer folded hook-shape. The V-shape fibril was pinned under reducing

compressive load between the probe and the backing layer (inset 4). Further reduction in compressive load resulted in fibril straightening out as the probe retracted (inset 6 and 7). The corresponding change in stress was negligible. Finally, the micropillar detached without adhesion (inset 8). Similar behaviour was observed for fibrils which show a buckling instability at high preloads ($d = 10, 12$ and $14 \mu\text{m}$ with $h = 33 \mu\text{m}$), when tested using the hemispherical probe.

7.4 Discussion

7.4.1 Aspect ratio

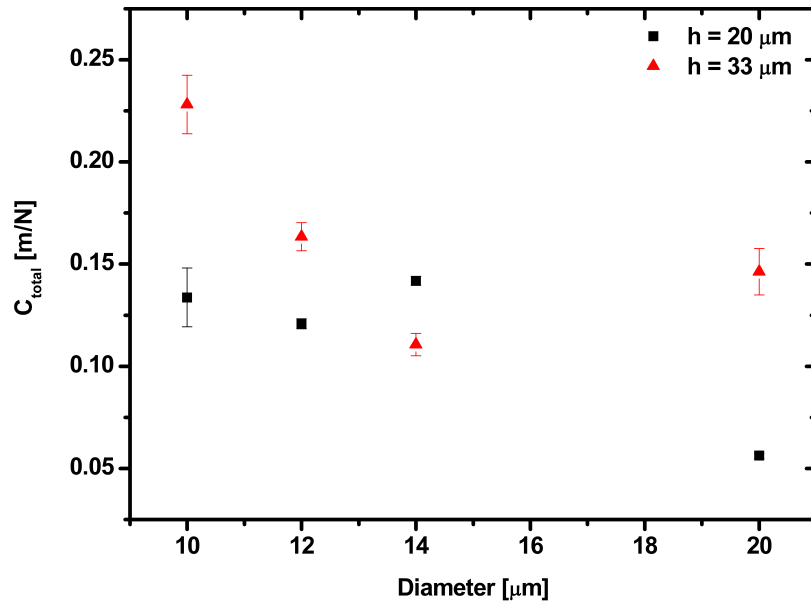
All micropillars having a height of $20 \mu\text{m}$ showed a decrease in pull-off strengths with an increase in fibril aspect ratio (with the exception of AR 1), see Figure 7.4 (a). These results are broadly consistent with the experimental results of Aksak, Hui and Sitti [Aksak2011] for single fibrils attached to a stiff probe over their entire tip-face area. They showed that an increase in the adhesion occurred with a decreasing AR and the *consequent stiffening* for a single fibril [Aksak2011]. To understand the influence of aspect ratio we first determine the fibril stiffness based on the total measured compliance of the single micropillar.

The compliance of the pillar and the backing are considered to be additive such that the effective compliance is $C_{tot} = C_{pillar} + C_{backing}$ [Guidoni2010]. C_{tot} of a single fibril was measured experimentally from the slope of the force-displacement curve in the *uniform tension regime* prior to pull-off, Figure 7.9 (a).

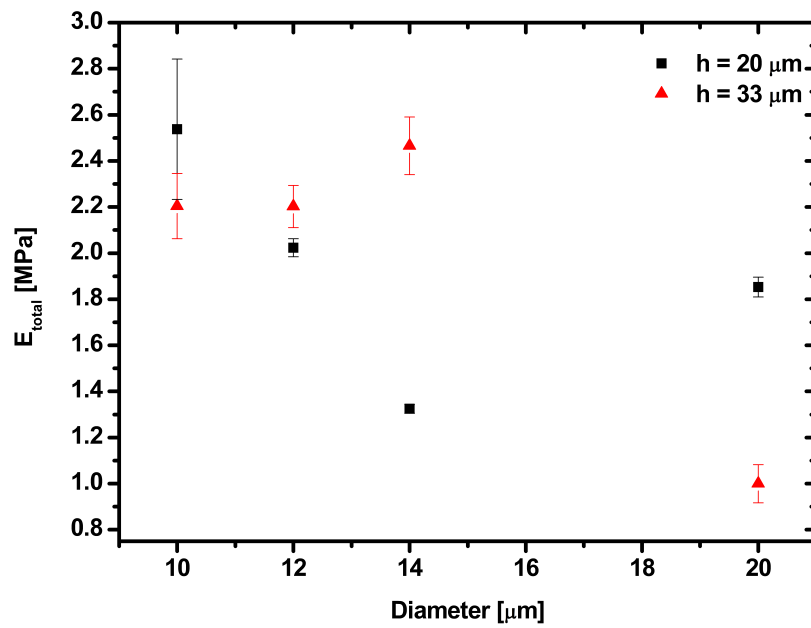
E_{tot} was calculated using the experimentally measured C_{tot} following the procedure by Bennewitz and co-authors [Guidoni2010],

$$E_{tot} = \left(\frac{h}{(1 - \nu^2)r} + \frac{16}{3\pi} \right) \frac{(1 - \nu^2)}{\pi r C_{tot}}, \quad (7.1)$$

where h and r are the fibril length and radius respectively and ν is the Poisson's ratio (≈ 0.5). The calculated E_{tot} based on Equation 7.1 for single micropillars of various diameters is presented in Figure 7.9 (b). Results show that when the pillar diameter was reduced, keeping



(a)



(b)

Figure 7.9: (a) Measured total compliance from the tensile regime of the force-displacement plots for all single micropillars. (b) Calculated total elastic modulus based on Equation 7.1.

the height constant, a general *increase* in E_{tot} was measured (Figure 7.9). Also, when the pillar height was increased keeping the diameter constant, higher C_{tot} was measured (with

the exception of $d = 14 \mu\text{m}$), yet adhesion was lower. Thus increase in adhesion was observed with an increase in stiffness of the micropillar, consistent with the results of Aksak *et al.*.

Aksak *et al.* [Aksak2011] investigated a model in which detachment was controlled by a circumferential crack. They found the pull-off force to be insensitive to an AR greater than unity when they assumed that all fibrils have the same flaw depth. Furthermore, when they used a model without a perimeter crack but having a Dugdale-Barrenblatt (DB) cohesive zone with characteristics approximately consistent with PDMS against glass, their theoretical results were essentially identical to those obtained in the presence of the circumferential flaw.

From the SEM images of single micropillars it appears that the micropillars have round edges (Figure 7.1 and 7.2). It is postulated that the detachment of such micropillars was controlled by the edge radius, with this feature acting as a circumferential crack around the fibril tip perimeter. Based on the above argument by Aksak *et al.* and these SEM images we infer that the pull-off strength displayed in Figure 7.4 (a) are controlled by the fibril tip edge radius acting as a circumferential crack. Additionally, the depth of the flaw in each case depends on the fibril diameter or AR. That is, the AR 1.4 fibril has the smallest circumferential crack whereas the AR = 1 and AR = 2 fibrils have the deepest ones, with the AR = 1.6 fibril being intermediate.

Some limitations of the above calculations for E_{tot} are: (1) The backing layer thickness for all the measured micropillars, although consistently greater than 1 mm was not uniform (thickness $\approx 2\text{-}2.5$ mm). Thickness variation affects the measured C_{tot} and E_{tot} . (2) The E_{tot} is sensitive to the accuracy with which both values of h and r are known. Fabrication processes cause slight variations in fibril dimensions from one sample to the other leading to variations in E_{tot} for the same sample.

7.4.2 Preload

Results in Figure 7.4 (a) are broadly independent of preload stress, and those in Figure 7.4 (b) are only weakly dependent on it. In the latter case, the dependence on preload can be attributed to the buckling of all micropillars with $h = 33 \mu\text{m}$, except AR 1.6, that occurred

at high preloads (Figure 7.4 (b)).

In situ studies showing the fibril-probe interface contact (insets in Figure 7.6) helped to understand the measured adhesion drop. The hook-shape that the fibril took after buckling remained stable throughout the time between buckling and unbuckling. This is because the buckled fibril was severely constrained between the plano-convex probe and the backing layer, with little opportunity to move relative to the probe and reconfigure its shape. In the hook-shape, there was always some fraction of the fibril tip that remained in an adhesive contact with the probe, even if much of the top-face had detached due to buckling. The fact that there is a residual area of the tip that remains in contact with the probe facilitates easy reattachment to the probe when it is retracted and the fibril unbuckles. Thus the use of the probe having a large curvature, the stiffness of the instrumentation, the size and AR of the fibrils, and the availability of compressive stress allowed for an almost complete reattachment of the fibril tip to the probe. Indeed, the images in the insets in Figure 7.6 suggest that the fibril top-face completely reattaches to the probe when the micropillar undergoes unbuckling. However, it is likely that some reconfiguration of the top-face adhesion to the probe occurs due to adhesion hysteresis. Thus, the contact configuration after buckling reversal will be somewhat different from that established after the fibril and probe are first brought into contact. As a consequence, the shape and size of the flaws that control the pull-off force will be somewhat different, leading to a slight reduction in the resulting pull-off force.

7.4.2.1 Slippage of a micropillar

In contrast, when a 1 mm diameter hemisphere was used as the probe, there was additional freedom of motion that the buckled fibril had due to the smaller radius of curvature of the probe. The strain energy of the fibril tends to introduce some irreversibility into the motion of the fibril tip relative to the probe as and when the system seeks paths that reduced its potential energy. As a consequence, the fibril tip was able to rotate and twist from under the apex of the probe to a location where there was a larger gap between the probe and the backing layer. This also involved the complete detachment of the fibril tip from the probe. The buckled fibril, was therefore able to slide relative to the probe, rotate and twist until it

had partially released the stored strain energy and lay prone on its sides. The fibril rotation was also partly induced by some inadvertent back-and-forth sideways motion of the probe when the nano-positioner controls its location.

The side of the fibril, with further retraction of the probe, simply peeled against the probe surface from its prone state. The fibril did not reach a buckled state again. Hence, prior to fibril detachment, when the distance between the probe and the backing layer was approximately equal to the length of the micropillar, most of the side contact between the fibril and the probe had been eliminated by peeling. The small remaining area of the side of the fibril, with no remnant tip contact, peeled-off the probe surface very easily so that negligible tension was needed for detachment. Thus it appears that tip contact re-formation during fibril unbuckling is crucial for any adhesion during final detachment.

7.4.3 Comparison to Euler buckling theory

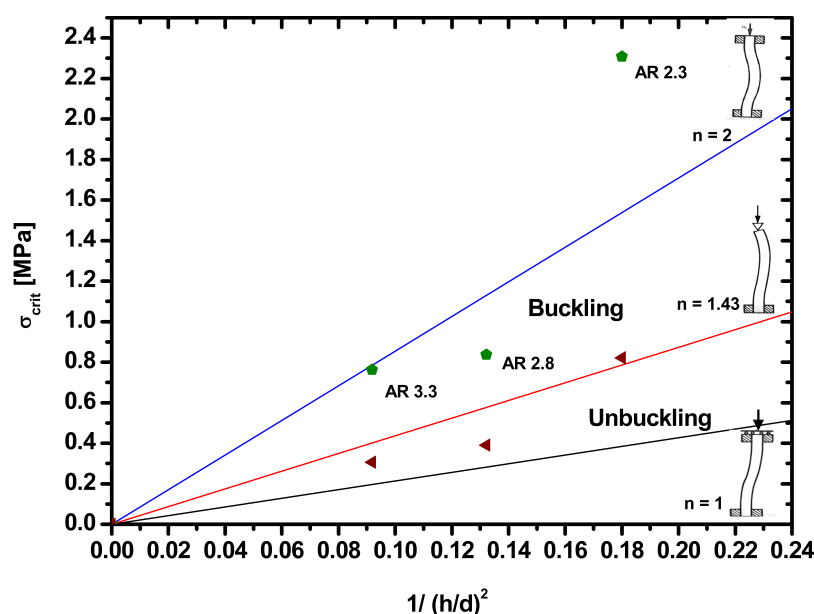


Figure 7.10: Experimental data (points) for the stress at buckling and unbuckling for single micropillars as a function of aspect ratio. Also shown are the theoretical results (lines) for Euler buckling under 3 different combinations of boundary conditions, as illustrated in the thumbnail sketches. A value of $E = 3.4$ MPa was used in the theoretical results.

Figure 7.10 shows the compressive stress on a fibril at buckling and unbuckling; the data points are obtained as averages from several repetitions of the experiments. The stress is plotted as functions of $1/(h/d)^2$ because of the scaling that occurs in the Euler buckling formula as discussed below. As expected, the fibrils with the highest AR buckle at the lowest stress and those with the lowest AR buckle at high stress. The trend is similar in the case of unbuckling. We note that the stress at which unbuckling occurs is considerably less than that at which buckling takes place.

To model the buckling and unbuckling load, we assume that the fibril can be treated as a slender column; such an assumption is not entirely justifiable, as a slender column would have an $AR > 7$, whereas the most slender fibrils in the present work had $AR = 3.3$. Nevertheless, we use the slender column assumption because relevant results for the buckling of a stocky column representative of the fibrils sitting on a backing layer are scarce. The critical stress for buckling was calculated using equation 7.2,

$$\sigma_{crit} = \frac{n^2 \pi^2 E_{tot}}{16} \frac{1}{(h/d)^2}, \quad (7.2)$$

where n is a pre-factor that depends on the end condition/restraint on the buckling pillar, I is the second moment of area of the fibril cross-section and h is the height of the micropillar and E_{tot} is the elastic modulus. The E_{tot} was determined using Equation 7.1 as described above (Section 7.4.1) with the important exception that the measurement of the total compliance was based on the *linear compressive regime* of the load-displacement curve prior to buckling. It was found that E_{tot} for the compressive regime was higher than in the that determined previously from the tensile regime with an overall average of $E_{tot} = 3.46 \pm 0.086$ MPa.

The predictions from Equation 7.2 are plotted in Figure 7.10 using the E_{tot} determined above for the Young's modulus. Since the abscissa of the plot represents $1/(h/d)^2$, the results form straight lines with slopes that depend on the value of n . Plots have been provided for 3 cases, where, for simplicity, the fibril base at the backing layer in all situations was assumed to be constrained against rotation. This assumption is not exactly valid due to a compliant backing.

For the case of $n = 1$, the fibril tip, adhered to the probe, is constrained not to rotate but can translate freely sideways. In another case, the constraint against rotation of the

fibril tip is retained and it is also forbidden to move sideways, giving a value $n = 2$. An intermediate case is also given, where the fibril tip, adhered to the probe, is free to rotate, but is not capable of translating sideways, so that $n = 1.43$ [Timoshenko1961]. The mode of buckling in each case is illustrated by a thumbnail sketch in Figure 7.10. Experimental buckling loads appear to agree more closely with the clamped-clamped ($n = 2$) prediction, though the stockiest fibril ($AR = 2.3$) buckles at a load significantly higher. However, the Euler buckling model based on slender column analysis becomes increasingly suspect as the AR falls, and the discrepancy for $AR = 2.3$ may be attributed to that.

The correlation between the experimental buckling results and the prediction from the clamped-clamped model, and of unbuckling with the clamped-free to rotate ($n = 1.43$) case, is consistent with comments of Hui *et al.* [Hui2007] and with the insights of Stark, Begley and McMeeking [Stark2012]. The latter workers considered the Euler buckling of a fibril clamped at its bottom end and adhering to a platen at its tip. In their case, the platen was free to translate sideways, and thus in the absence of tip detachment behaved like the case of $n = 1$. Stark *et al.* [Stark2012] found that buckling initiated at the load consistent with the critical load for a column fully adhered at its tip, *i.e.* at the level predicted by the case of $n = 1$. Such a response arises because when buckling commences under rising compressive load, the tip adhering to the platen is in compression everywhere at the moment buckling sets in and thus is not free to rotate. In our experiments the probe to which the fibril tip is adhered is not free to translate sideways. We deduce from this that buckling of an adhered fibril under rising compressive load will occur at the critical load consistent with the clamped-clamped case ($n = 2$) illustrated in Figure 7.10. The fibril tip will be in compression everywhere at the instant when buckling commences and will be neither free to rotate nor translate sideways. To the extent that the Euler buckling model used to predict buckling in the clamped-clamped case is relevant to our stocky fibrils, it is thus consistent that the buckling in the experiments correlates most closely with the line for the clamped-clamped case that has $n = 2$.

Stark *et al.* [Stark2012] deduced from their modeling that shortly after buckling occurred under rising compressive load, detachment of the fibril tip from the platen begins due to the

tension that develops on one side of the contact because of the bending of the fibril during buckling. This process continues until only a small fraction of the fibril tip is in contact with the platen, and, simultaneously, the compressive load drops dramatically. When the platen is retracted, the compressive load relaxes and the buckled fibril then sits with its tip only partially adhered to the platen. Because of that condition the fibril tip is relatively free to rotate, so that unbuckling can occur in conditions that are best modeled by the clamped-free to rotate case ($n = 1.43$) illustrated in Figure 7.10. Therefore, in our experiments we can expect that unbuckling occurs at a load close to that predicted by the clamped-free to rotate case ($n = 1.43$). The experimental data for unbuckling agreed fairly well with this prediction.

7.5 Conclusions

Buckling of adhesive single micropillars of PDMS was investigated. This study shows that:

- The adhesion of single micropillars generally increased with a decrease in their aspect ratio and corresponding stiffening. This effect was investigated by systematically changing the fibril AR and taking into account the combined stiffness of the fibril and the backing layer. Round edge of the fibrils further influences the adhesion strength by acting as a circumferential defect.
- Reversible buckling ensured contact re-formation under a probe having a large curvature and the availability of compressive stress. *In situ* studies showed that the contact re-formation was assisted by the residual area of the tip that remains in contact with the probe in the buckled state. The slight drop in adhesion was attributed to adhesion hysteresis.
- Irreversible buckling occurred when the fibril slipped during unloading under a hemispherical probe. *In situ* studies showed that the micropillar simply peeled against the probe in side contact without again reaching a buckled state. Lack of tip contact re-formation was responsible for loss in adhesion observed in this case.

- Buckling of fibrils appears to follow the predictions of Euler buckling theory; higher AR fibrils buckled at lower stress. During buckling the pillar acted as being clamped at the base as well as at the top. During unbuckling the tip was relatively free to rotate. This freedom could only be exercised when the applied stress was enough to overcome the fibril-probe adhesion.

Chapter 8

Summary and Outlook

The present study demonstrated the use of mechanical instability of structures to generate repeatable and switchable adhesion in bioinspired adhesives. The gecko attachment system formed the basis of the design and functionality of these adhesives.

Structuring of PDMS surface was carried out combining the techniques of photolithography and soft molding. SU-8 photoresist was used to fabricate masters with desired patterns such as hexagonally packed arrays of cylindrical holes. PDMS was replica molded from these masters and consisted of different aspect ratio fibrils with heights of 20 to 33 μm and diameters of 10 to 20 μm . Fibril tips had *end-flaps* generated using thermal stress induced cracking in SU-8 films or *round edges* created using surface tension based rounding in the PDMS.

The contact phenomena during an adhesion test were studied by microscopic optical visualization of the top view of the fibril-probe interface. This was complemented by high magnification, *in situ*, side view imaging of the contact interface and the fibril backing in a custom-modified Environmental Scanning Electron Microscope (ESEM).

Mechanical buckling instability in the fibrils was introduced by applying (compressive) preload using a flat probe of known stiffness. Normal compression caused the fibrils to buckle inducing a contact transition from tip to side. When the contact transition of the fibrils occurred under moderate compressive loads, tip contact re-formed upon buckling reversal and

adhesion was reversible. When, however, buckling occurred under large compressive loads drastic change in contact area resulted upon buckling reversal, which led to an adhesion loss. The contact shape of the fibrils controlled the adhesion reversibility along with the preload. Round edged fibrils showed poor contact adaptability and failed at re-establishing an adhesive contact upon buckling reversal. In contrast, fibrils with end-flaps showed superior contact adaptability which was a function of fibril orientation and preload. *In situ* visualization indicated that end-flaps themselves may fold-unfold during buckling-unbuckling depending on the preload and the orientation. The conditional folding-unfolding of end-flaps was used to generate the states of adhesion and non-adhesion reversibly and repeatably.

In summary, by judiciously combining the applied preload, the tip-shape and the orientation of the fibrils with respect to the test probe the desired state of adhesion or non-adhesion may be generated controllably and reversibly.

Buckling studies on a single adhesive micropillar were also carried out in order to isolate the stochastic effects observed in arrays of fibrils. These studies clearly showed that, whenever any link between the fibril top surface and the probe was preserved during fibril buckling, lost adhesion can be recovered. The importance of the backing layer was also highlighted through these studies. The combined stiffness of the single micropillar and the backing showed an increase with the decreasing fibril aspect ratio. A stiffer single fibril showed better adhesion than a more compliant one. The mechanisms of contact re-formation were found to be unique to the fibril's response to reversible and irreversible buckling. These results may help in designing a responsive adhesive system that is based on application of a mechanical instability.

The adhesives developed during this work demonstrated use in simple applications that need pick-and-place of an object. In designing pick-and-place robot systems it is important that the mechanical instability of the fibrils is recognized with respect to the applied load and orientation. The range of loads as well as the orientation at which fibrils hold the load (normal, shear or mixed) should be known to avoid accidental over-compression and loss of an object. End-flap terminated fibrillar adhesives have functioned even when they were not well-aligned to the smooth surfaces. The invariance to alignment, combined with the

possibility of achieving reversible and repeatable adhesion render their use as switchable adhesives practical.

Their capability to lift a smooth glass plate (with / without dead weights) and its easy release by use of pressure or orientation change was demonstrated. The lifting of 500 g weight using a small strip of adhesive (contact area $\approx 1 \text{ cm}^2$) is seen in the video snapshot, Figure 8.1. The strip was brought in contact with a glass plate to which 500 g weight was attached. When both the adhesive and the area of contact on glass are clean, then no external pressure was required to form an adhesive contact. It was possible to lift the glass in normal as well as shear mode (shear stress $\leq 0.5 \text{ MPa}$). Importantly, the adhesive can be easily released

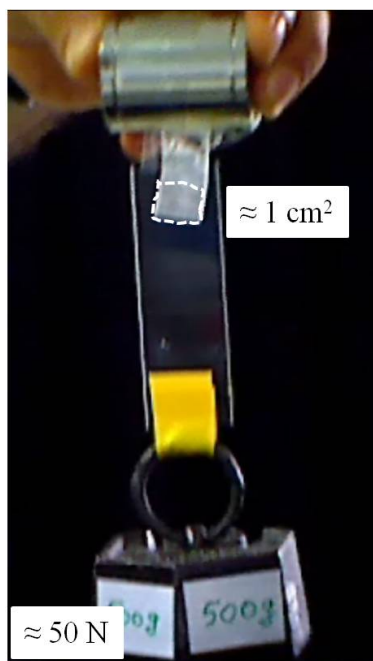


Figure 8.1: Video snapshot of performance of pressure switch. 500 g weight attached to the glass slide lifted by $\approx 1 \text{ cm}^2$ patch of adhesive (<http://www.inm-gmbh.de/en/research/interface-materials/functional-surfaces/>)

from the surface with simple change of orientation or by applied pressure that triggers the mechanical instability in fibrils. In practice, removal of the adhesive was easily achieved by a peeling action or by applying a push on the adhesive against the glass (estimated stresses to release $\leq 0.5 \text{ MPa}$).

In outlook, applications such as joining two hard glass plates may be also be envisaged. One of the challenges to overcome is the present limited upscaling ability of these structures. Presented process capabilities are restricted to producing areas of the order of few centimeter square. Secondly, adaptability is restricted to smooth polished surfaces such as those of glass. Hybrid material systems combining the advantages of high adhesive strengths of some materials with the reversibility inherent to a different set of materials will most likely guide the future development of switchable adhesive systems.

Bibliography

- [Aksak2011] B. Aksak, C. Y. Hui, and M. Sitti, The effect of aspect ratio on adhesion and stiffness for soft elastic fibres., *J. R. Soc.: Interface*, 8:1166–1175, 2011.
- [Arzt2002] E. Arzt, S. Enders, and S. Gorb, Towards a micromechanical understanding of biological surface devices, *Z. Metallk.*, 93(5):345–351, 2002.
- [Arzt2003] E. Arzt, S. Gorb, and R. Spolenak, From micro to nano contacts in biological attachment devices, *Proc. Natl. Acad. Sci.*, 100(19):10603–10606, 2003.
- [Ashby2000] M. F. Ashby, *Materials selection in mechanical design*, Butterworth-Heinemann, Oxford, second edition, pages 384–385, 2000.
- [Autumn2000] K. Autumn, Y. A. Liang, S. T. Hsieh, W. Zesch, W. P. Chan, T. W. Kenny, R. Fearing, and R. J. Full, Adhesive force of a single gecko foot-hair., *Nature*, 405(6787):681–685, 2000.
- [Autumn2002] K. Autumn, M. Sitti, Y. A. Liang, A. M. Peattie, W. R. Hansen, S. Sponberg, T. W. Kenny, R. Fearing, J. N. Israelachvili, and R. J. Full, Evidence for van der Waals adhesion in gecko setae, *Proc. Natl. Acad. Sci.*, 99(19):12252–12256, 2002.
- [Autumn2002b] K. Autumn, Mechanisms of Adhesion in Geckos, *Integr. Comp. Biol.*, 42(6):1081–1090, 2002.
- [Autumn2006] K. Autumn, A. Dittmore, D. Santos, M. Spenko, and M. Cutkosky, Frictional adhesion: a new angle on gecko attachment, *J. Exp. Biol.*, 209(18):3569–3579, 2006.
- [Autumn2006a] K. Autumn, C. Majidi, R. E. Groff, A. Dittmore, and R. Fearing, Effective elastic modulus of isolated gecko setal arrays, *J. Exp. Biol.*, 209(18):3558–3568, 2006.
- [Autumn2008] K. Autumn and N. Gravish, Gecko adhesion: evolutionary nanotechnology, *Phil. Trans. R. Soc. A*, 366(1870):1575–1590, 2008.

-
- [Boesel2010] L. F. Boesel, C. Greiner, E. Arzt, and A. del Campo, Gecko-inspired surfaces: a path to strong and reversible dry adhesives., *Adv. Mater.*, 22(19):2125–37, 2010.
- [Bowden1998] N. Bowden, S. Brittain, A. G. Evans, J. W. Hutchinson, and G. M. Whitesides, Spontaneous formation of ordered structures in thin films of metals supported on an elastomeric polymer, *Nature*, 393(6681):146–149, 1998.
- [Bullock2008] J. M. R. Bullock, P. Drechsler, and W. Federle, Comparison of smooth and hairy attachment pads in insects: friction, adhesion and mechanisms for direction-dependence., *J. Exp. Biol.*, 211(20):3333–3343, 2008.
- [Carbone2011] G. Carbone, E. Pierro, and S. N. Gorb, Origin of the superior adhesive performance of mushroom-shaped microstructured surfaces, *Soft Matter*, 7(12):5545, 2011.
- [Chen2010] B. Chen and H. Gao, An alternative explanation of the effect of humidity in gecko adhesion: stiffness reduction enhances adhesion on a rough surface., *Int. J. Appl. Mech.*, 2:1–9, 2010.
- [Clemente2008] C. J. Clemente and W. Federle, Pushing versus pulling: division of labour between tarsal attachment pads in cockroaches, *Proc. Biol. Sci.*, 275:1329–1336, 2008.
- [Creton2007] C. Creton and S. Gorb, Sticky Feet: From Animals to Materials Overview : Reversible Adhesion, *MRS Bull.*, 32:466–472, 2007.
- [Crosby2005] A. J. Crosby, M. Hageman, and A. Duncan, Controlling Polymer Adhesion with Pancakes, *Langmuir*, 21(25):11738–11743, 2005.
- [Delrio2005] F. W. Delrio, M. P. de Boer, J. A. Knapp, E. David Reedy, P. J. Clews, and M. L. Dunn, The role of van der Waals forces in adhesion of micromachined surfaces., *Nat. Mater.*, 4(8):629–34, 2005.
- [Dirks2011] J. H. Dirks and W. Federle, Fluid-based adhesion in insects principles and challenges, *Soft Matter*, 7:11047–11053, 2011.
- [Federle2000] W. Federle and B. Rohrseitz, K. and Hölldobler, Attachment forces of ants measured with a centrifuge: better ‘wax-runners’ have a poorer attachment to a smooth surface., *J. Exp. Biol.*, 203(3):505–12, 2000.
- [Federle2001a] W. Federle, E. L. Brainerd, T. A. McMahon, and B. Hölldobler, Biomechanics of the movable pretarsal adhesive organ in ants and bees, *Proc. Natl. Acad. Sci.*, 98:6215–6220, 2001.

-
- [Federle2006] W. Federle, Why are so many adhesive pads hairy?, *J. Exp. Biol.*, 209(14):2611–2621, 2006.
- [Fratzl2009] P. Fratzl and F. G. Barth, Biomaterial systems for mechanosensing and actuation, *Nature*, 462(7272):442–448, 2009.
- [Gao2004] H. Gao and H. Yao, Shape insensitive optimal adhesion of nanoscale fibrillar structures, *Proc. Natl. Acad. Sci.*, 101(21):7851–7856, 2004.
- [Gao2005] H. Gao, X. Wang, S. Yao, H. and Gorb, and E. Arzt, Mechanics of hierarchical adhesion structures of geckos, *Mech. Mater.*, 37(2-3):275–285, 2005.
- [Ge2007] L. Ge, S. Sethi, L. Ci, P.M. Ajayan, and A. Dhinojwala, Carbon nanotube-based synthetic gecko tapes, *Proc. Natl. Acad. Sci.*, 104(26):10792, 2007.
- [Glassmaker2004] N. J. Glassmaker, T. Himeno, C. Y. Hui, and J. Kim, Design of biomimetic fibrillar interfaces: 1. Making contact., *J. R. Soc.: Interface*, 1(1):23–33, 2004.
- [Glassmaker2007] N.J. Glassmaker, A. Jagota, C.Y. Hui, W.L. Noderer, and M.K. Chaudhury, Biologically inspired crack trapping for enhanced adhesion, *Proc. Natl. Acad. Sci.*, 104(26):10786, 2007.
- [Gorb2000] S. Gorb and M. Scherge, Biological microtribology: anisotropy in frictional forces of orthopteran attachment pads reflects the ultrastructure of a highly deformable material., *P Roy. Soc. Lond. B Bio.*, 267(1449):1239–44, 2000.
- [Gorb2007] S. Gorb, M. Varenberg, A. Peressadko, and J. Tuma, Biomimetic mushroom-shaped fibrillar adhesive microstructure , *J. R. Soc.: Interface*, 4(13):271–275, 2007.
- [Greiner2007] C Greiner, A del Campo, and E Arzt, Adhesion of bioinspired micropatterned surfaces: Effects of pillar radius, aspect ratio, and preload, *Langmuir*, 23(7):3495–3502, 2007.
- [Greiner2007a] C. Greiner, *Size and Shape Effects in Bioinspired Fibrillar Adhesives*, Phd thesis, University of Stuttgart, pages 72–74, 2007.
- [Guidoni2010] G.M. Guidoni, D. Schillo, U. Hangen, G. Castellanos, E. Arzt, R.M. McMeeking, and R. Bennewitz, Discrete contact mechanics of a fibrillar surface with backing layer interactions, *J. Mech. Phys. Solids*, 58(10):1571–1581, 2010.
- [Hansen2005] W. R. Hansen and K. Autumn, Evidence for self-cleaning in gecko setae, *Proc. Natl. Acad. Sci.*, 102(2):385–389, 2005.
- [Huber2005] G. Huber, H. Mantz, R. Spolenak, K. Mecke, K. Jacobs, S. N. Gorb, and E. Arzt, Evidence for capillarity contributions to gecko adhesion

-
- from single spatula nanomechanical measurements, *Proc. Natl. Acad. Sci.*, 102(45):16293–16296, 2005.
- [Hui2002] C. Y. Hui, A. Jagota, Y. Y. Lin, and E. J. Kramer, Constraints on Microcontact Printing Imposed by Stamp Deformation, *Langmuir*, 18(4):1394–1407, 2002.
- [Hui2003] C. Y. Hui, A. Jagota, S. J. Bennison, and J. D. Londono, Crack blunting and the strength of soft elastic solids, *P. Roy. Soc. Lond. A Mat.*, 459(2034):1489–1516, June 2003.
- [Hui2004] C. Y. Hui, N. J. Glassmaker, T. Tang, and A. Jagota, Design of biomimetic fibrillar interfaces: 2. Mechanics of enhanced adhesion, *J. R. Soc.: Interface*, 1(1):35–48, 2004.
- [Hui2005] C. Y. Hui, N. J. Glassmaker, and A. Jagota, How compliance compensates for surface roughness in fibrillar adhesion, *J. Adhesion*, 81(7-8):699–721, 2005.
- [Hui2007] C. Y. Hui, A. Jagota, L. Shen, A. Rajan, N. Glassmaker, and T. Tang, Design of bio-inspired fibrillar interfaces for contact and adhesion theory and experiments, *J. Adhes. Sci. Tech.*, 21(12):1259–1280, 2007.
- [Jagota2002] A. Jagota and S. Bennison, Mechanics of adhesion through a fibrillar microstructure, *Integr. Comp. Biol.*, 42:1140–1145, 2002.
- [Jagota2007] A. Jagota, C. Y. Hui, N. J. Glassmaker, and T. Tang, Mechanics of bioinspired and biomimetic fibrillar interfaces, *MRS Bull.*, 32(6):492–495, 2007.
- [Jagota2011] A. Jagota and C. Y. Hui, Adhesion, friction, and compliance of bio-mimetic and bio-inspired structured interfaces, *Mat. Sci. Eng. R*, 72(12):253–292, 2011.
- [Jeong2009] H. E. Jeong, J. K. Lee, H. N. Kim, S. H. Moon, and K. Y. Suh, A nontransferring dry adhesive with hierarchical polymer nanohairs., *Proc. Natl. Acad. Sci.*, 106(14):5639–44, 2009.
- [Jeong2010] H. E. Jeong, M. K. Kwak, and K. Y. Suh, Stretchable, adhesion-tunable dry adhesive by surface wrinkling., *Langmuir*, 26(4):2223–6, 2010.
- [Jiao2000] Y. Jiao, S. Gorb, and M. Scherge, Adhesion measured on the attachment pads of *Tettigonia viridissima* (Orthoptera, insecta), *J. Exp. Biol.*, 203(12):1887–1895, 2000.
- [Johnson1971] K L Johnson, K Kendall, and A D Roberts, Surface Energy and the Contact of Elastic Solids, *Proc. R. Soc. A*, 324(1558):301–313, 1971.

-
- [Josse2004] G. Josse, P. Sergot, C. Creton, and M. Dorget, Measuring interfacial adhesion between a soft viscoelastic layer and a rigid surface using a probe method, *J. Adhesion*, 80(1):87–118, 2004.
- [Kamperman2010] M. Kamperman, E. Kroner, A. del Campo, R. M. McMeeking, and E. Arzt, Functional Adhesive Surfaces with Gecko Effect: The Concept of Contact Splitting, *Adv. Eng. Mater.*, 12(5):335–348, May 2010.
- [Kim2006] S. Kim and M. Sitti, Biologically inspired polymer microfibers with spatulate tips as repeatable fibrillar adhesives, *Appl. Phys. Lett.*, 89:261911–261913, 2006.
- [Kim2007b] S. Kim, M. Sitti, C. Y. Hui, R. Long, and A. Jagota, Effect of backing layer thickness on adhesion of single-level elastomer fiber arrays, *Appl. Phys. Lett.*, 91(16):161905–161908, 2007.
- [Kim2009a] S. Kim, E. Cheung, and M. Sitti, Wet self-cleaning of biologically inspired elastomer mushroom shaped microfibrillar adhesives., *Langmuir*, 25(13):7196–9, 2009.
- [Kim2009b] S. Kim, M. Sitti, T. Xie, and X. Xiao, Reversible dry micro-fibrillar adhesives with thermally controllable adhesion, *Soft Matter*, 5(19):3689, 2009.
- [Kroner2011] E. Kroner, D. R. Paretkar, R. M. McMeeking, and E. Arzt, Adhesion of Flat and Structured PDMS Samples to Spherical and Flat Probes: A Comparative Study, *J. Adhesion*, 87(5):447–465, 2011.
- [Kroner2011a] E. Kroner, *Adhesion measurements on patterned elastomeric surfaces*, Phd thesis, University of Saarland, pages 125–127, 2011.
- [Kroner2012] E. Kroner, J. Blau, and E. Arzt, Note: An adhesion measurement setup for bioinspired fibrillar surfaces using flat probes, *Rev. Sci. Instrum.*, 83(1):016101, January 2012.
- [Lee2009] J. Lee, B. Bush, R. Maboudian, and R. S. Fearing, Gecko-inspired combined lamellar and nanofibrillar array for adhesion on nonplanar surface., *Langmuir*, 25(21):12449–53, 2009.
- [Long2008] R. Long, C. Y. Hui, S. Kim, and M. Sitti, Modeling the soft backing layer thickness effect on adhesion of elastic microfiber arrays, *J. Appl. Phys.*, 104(4):044301–9, 2008.
- [Maboudian2004] R. Maboudian and C. Carraro, Surface chemistry and tribology of MEMS., *Annu. Rev. Phys. Chem.*, 55(1):35–54, 2004.

-
- [Madou2002] M. J. Madou, *Fundamentals of microfabrication: the science of miniaturization*, CRC Press, Boca Raton, FL, second edition, pages 118–120, 2002.
- [Majumder2007] A. Majumder, A. Ghatak, and A. Sharma, Microfluidic adhesion induced by subsurface microstructures., *Science*, 318(5848):258–61, 2007.
- [Mark1977] J. E. Mark and J. L. Sullivan, Model networks of end-linked polydimethylsiloxane chains. I. Comparisons between experimental and theoretical values of the elastic modulus and the equilibrium degree of swelling, *J. Chem. Phys.*, 66(3):1006–1011, 1977.
- [McDonald2002] J. C. McDonald and G. M. Whitesides, Poly(dimethylsiloxane) as a material for fabricating microfluidic devices, *Accounts Chem. Res.*, 35(7):491–499, 2002.
- [McMeeking2008] R. M. McMeeking, E. Arzt, and A. G. Evans, Defect Dependent Adhesion of Fibrillar Surfaces, *J. Adhesion*, 84(7):675–681, 2008.
- [Menguc2012] Y. Mengüç, S. Y. Yang, S. Kim, J. Rogers, and M. Sitti, Gecko-Inspired Controllable Adhesive Structures Applied to Micromanipulation, *Adv. Funct. Mater.*, 22(6):1245–1253, 2012.
- [Mora2010] S. Mora, T. Phou, J. M. Fromental, L. M. Pismen, and Y. Pomeau, Capillarity Driven Instability of a Soft Solid, *Phys. Rev. Lett.*, 105(21):214301, 2010.
- [Murphy2009] M. P. Murphy, B. Aksak, and M. Sitti, Gecko-inspired directional and controllable adhesion., *Small*, 5(2):170–5, 2009.
- [Nadermann2010] N. Nadermann, A. Kumar, S. Goyal, and C. Y. Hui, Buckling of sheared and compressed microfibrils., *J. R. Soc.: Interface*, 17(52):1581–9, 2010.
- [Nadermann2010a] Nichole Nadermann, Jing Ning, Anand Jagota, and C-Y Hui, Active switching of adhesion in a film-terminated fibrillar structure., *Langmuir*, 26(19):15464–15471, 2010.
- [Northen2008] M. T. Northen, C. Greiner, E. Arzt, and K. L. Turner, A Gecko-Inspired Reversible Adhesive, *Adv. Mater.*, 20(20):3905–3909, 2008.
- [Paretkar2008] D. R. Paretkar, Thin metal film based stretchable electronic conductors, Master’s thesis, University of Cambridge, UK, pages 63–67, 2008.
- [Paretkar2011] D. Paretkar, M. Kamperman, A. S. Schneider, D. Martina, C. Creton, and E. Arzt, Bioinspired pressure actuated adhesive system, *Mat. Sci. Eng. C-Bio. S.*, 31(6):1152–1159, 2011.

-
- [Paretkar2011a] D. Paretkar, A. S. Schneider, E. Kroner, and E. Arzt, In situ observation of contact mechanisms in bioinspired adhesives at high magnification, *MRS Comm.*, 1:53–56, 2011.
- [Peattie2009] A. M. Peattie, Functional demands of dynamic biological adhesion: an integrative approach., *J. Comp. Physiol. B*, 179(3):231–239, 2009.
- [Peressadko2004] A. Peressadko and S.N. Gorb, When less is more: experimental evidence for tenacity enhancement by division of contact area, *J. Adhesion*, 80(4):247–261, 2004.
- [Persson2003] B. N. J. Persson, On the mechanism of adhesion in biological systems, *J. Chem. Phys.*, 118(16):7614–7621, 2003.
- [Persson2003a] B. N. J. Persson and S. Gorb, The effect of surface roughness on the adhesion of elastic plates with application to biological systems, *J. Phys. Chem.*, 119(21):11437–11444, 2003.
- [Persson2005] B. N. J. Persson, O. Albohr, U. Tartaglino, A. I. Volokitin, and E. Tosatti, On the nature of surface roughness with application to contact mechanics, sealing, rubber friction and adhesion, *J. Phys-Condens. Mat.*, 17(1):R1–R62, 2005.
- [Puthoff2010] J. B. Puthoff, M. S. Prowse, M. Wilkinson, and K. Autumn, Changes in materials properties explain the effects of humidity on gecko adhesion, *J. Exp. Biol.*, 213(21):3699–3704, 2010.
- [Reddy2007] S. Reddy, E. Arzt, and A. del Campo, Bioinspired Surfaces with Switchable Adhesion, *Adv. Mater.*, 19(22):3833–3837, 2007.
- [Santos2005] R. Santos, S. N. Gorb, V. Jamar, and P. Flammang, Adhesion of echinoderm tube feet to rough surfaces., *J. Exp. Biol.*, 208(13):2555–67, 2005.
- [Schneider2008] F. Schneider, T. Fellner, J. Wilde, and U. Wallrabe, Mechanical properties of silicones for MEMS, *J. Micromech. Microeng.*, 18(6):065008, 2008.
- [Schoen2010] I. Schoen, W. Hu, E. Klotzsch, and V. Vogel, Probing cellular traction forces by micropillar arrays: contribution of substrate warping to pillar deflection., *Nano Lett.*, 10(5):1823–30, 2010.
- [Schubert2007] B. Schubert, C. Majidi, R. E. Groff, S. Baek, B. Bush, R. Maboudian, and R. S. Fearing, Towards friction and adhesion from high modulus microfiber arrays, *J. Adhes. Sci. Tech.*, 21:1297–1315, 2007.
- [Sitti2003] M. Sitti and R. S. Fearing, Synthetic gecko foot-hair micro/nano-structures as dry adhesives, *J. Adhes. Sci. Tech.*, 17:1055–1073(19), 2003.

-
- [Spolenak2005] R. Spolenak, S. Gorb, H. Gao, and E. Arzt, Effects of contact shape on the scaling of biological attachments, *P. Roy. Soc. Lond. A Mat.*, 461(2054):305–319, 2005.
- [Spuskanyuk2008] A. V. Spuskanyuk, R. M. McMeeking, V. S. Deshpande, and E. Arzt, The effect of shape on the adhesion of fibrillar surfaces., *Acta Biomater.*, 4(6):1669–76, 2008.
- [Stark2012] S. Stark, M. R. Begley, and R. M. McMeeking, The buckling and post-buckling of fibrils adhering to a rigid surface, *J. Appl. Mech.*, submitted.
- [Tang2005] T. Tang, C. Y. Hui, and N. J. Glassmaker, Can a fibrillar interface be stronger and tougher than a non-fibrillar one?, *J. R. Soc.: Interface*, 2(5):505–16, 2005.
- [Tian2006] Y. Tian, N. Pesika, H. Zeng, K. Rosenberg, B. Zhao, P. McGuiggan, K. Autumn, and J. Israelachvili, Adhesion and friction in gecko toe attachment and detachment., *Proc. Natl. Acad. Sci.*, 103(51):19320–5, 2006.
- [Timoshenko1961] S. P. Timoshenko and J. M. Gere, *Theory of elastic stability*, McGraw-Hill Book Company, Inc., New York and London, second edition, pages 47–50, 1961.
- [Trejore2010] V. L. M. Trejore, Metal-PDMS hybrid systems for switchable adhesion, Masters, Saarland University, 2010.
- [Vajpayee2008] S. Vajpayee, C. Y. Hui, and A. Jagota, Model-independent extraction of adhesion energy from indentation experiments., *Langmuir*, 24(17):9401–9, 2008.
- [Vajpayee2010] S. Vajpayee, A. Jagota, and C.-Y. Hui, Adhesion of a Fibrillar Interface on Wet and Rough Surfaces, *J. Adhesion*, 86(1):39–61, 2010.
- [Varenberg2008] M. Varenberg and S. Gorb, Close-up of mushroom-shaped fibrillar adhesive microstructure: contact element behaviour., *J. R. Soc.: Interface*, 5(24):785–9, 2008.
- [Varenberg2008a] M. Varenberg and S. Gorb, A beetle-inspired solution for underwater adhesion, *J. R. Soc.: Interface*, 5(20):383–385, 2008.
- [Wang2009a] G. F. Wang and X. Q. Feng, Timoshenko beam model for buckling and vibration of nanowires with surface effects, *J. Phys. D: Appl. Phys.*, 42(15):155411, 2009.
- [Wang2010] R. Wang and T. Xie, Shape memory- and hydrogen bonding-based strong reversible adhesive system., *Langmuir*, 26(5):2999–3002, 2010.

-
- [Wang2011] Z. Wang, Polydimethylsiloxane Mechanical Properties Measured By Macroscopic Compression And Nanoindentation Techniques, Masters, University of South Florida, pages 16–18, 2011.
- [Xie2008] T. Xie and X. Xiao, Self-Peeling Reversible Dry Adhesive System, *Chem. Mater.*, 20(9):2866–2868, 2008.
- [Yamaguchi2009] T. Yamaguchi, N. Gravish, K. Autumn, and C. Creton, Microscopic Modeling of the Dynamics of Frictional Adhesion in the Gecko Attachment System, *J. Phys. Chem. B*, 113(12):3622–3628, 2009.
- [Zhao2008] B. Zhao, N. Pesika, K. Rosenberg, Y. Tian, H. Zeng, P. McGuiggan, K. Autumn, and J. Israelachvili, Adhesion and friction force coupling of gecko setal arrays: implications for structured adhesive surfaces., *Langmuir*, 24(4):1517–24, 2008.
- [Zhao2009] B. Zhao, N. Pesika, H. Zeng, Z. Wei, Y. Chen, K. Autumn, K. Turner, and J. Israelachvili, Role of Tilted Adhesion Fibrils (Setae) in the Adhesion and Locomotion of Gecko-like Systems, *J. Phy. Chem. B*, 113(12):3615–3621, 2009.
- [delCampo2007] A. del Campo, C. Greiner, and E. Arzt, Contact shape controls adhesion of bioinspired fibrillar surfaces, *Langmuir*, 23(20):10235–10243, 2007.
- [delCampo2007a] A. del Campo and C. Greiner, SU-8: a photoresist for high-aspect-ratio and 3D submicron lithography, *J. Micromech. Microeng.*, 17(6):R81–R95, 2007.
- [delCampo2007b] A. del Campo, C. Greiner, I. Alvarez, and E. Arzt, Patterned Surfaces with Pillars with Controlled 3D Tip Geometry Mimicking Bioattachment Devices, *Adv. Mater.*, 19(15):1973–1977, 2007.

Appendices

Appendix I: Supplementary information to Chapter 3

Polyurethane shape memory polymer (SMP) Tecoflex™ 72 D was structured using replica molding. Tecoflex was dissolved in chloroform to obtain different solutions (2.5 to 20 % by weight) and cast on SU-8 masters patterned with holes. Thinner films resulted from more dilute solutions as the solvent (chloroform) evaporated from the mold over a period of 6-7 hours. The thickness of Tecoflex films varied from 0.03 to 3 mm. The solvent evaporation additionally resulted in hollow fibrils. When the SU-8 films contained thermal stress induced cracks (Chapter 6, Section 6.2.1), mushroom shaped tips on hollow Tecoflex fibrils were obtained (Figure 3.9 (c)).

The SMP has the lower glass transition temperature (T_g) around 51°C [Reddy2007]. Heating the structured tecoflex to $\approx 70^\circ\text{C}$ ($T > T_g$) resulted in softening of the polymer. In the soft state, mechanical shear was induced to tilt the vertical fibrils. Retaining the shear while cooling to room temperature generated tilted fibrils. Excessive mechanical shear, induced manually, caused the fibrils to lay permanently prone on the backing (Figure 3.10 (b)). Also, solvent based inking, which results in selective dissolution of Tecoflex, can be used to modify fibril orientations and tip shapes. For this purpose chloroform was gently brushed over the vertical fibrillar array resulting in selective dissolution of fibril tips (Figure 3.10 (c)). Brushing with solvent several times resulted in greater amount of tecoflex removal, which was used to modify fibril shape and tilt.

Appendix II: Supplementary information to Chapter 4

The sample alignment with respect to the flat probe ($d = 1$ mm, glass cylinder) fixed on double-beam spring was optimized as follows: Pull-off forces were measured at a constant preload as a function of the sample's tilt along the U and V axes (Figure 8.2). The preload was carefully chosen to lie well below the critical preload at which fibrils become mechanically unstable. Additionally, the chosen preload required that the fibrils established a good contact with the entire probe area. Tilting of the sample in both directions, perpendicular (V axis) and parallel (U axis) to the probe-double-beam axis was achieved by changing the sample tilt in steps of 0.01° . As the sample tilt approached the parallel sample-probe configuration, higher displacements were required to reach the predefined preload. An accompanying increase in the pull-off strengths was also observed. The tilt (combination of the V and U axes tilts, Figure 3.4) that required the longest sample displacement to reach the predefined preload stress and which also showed a high pull-off strength, was chosen as

the "aligned state". In Figure 8.2 the aligned state was reached for the sample tilt of $U = -0.1^\circ$ and $V = -0.6^\circ$.

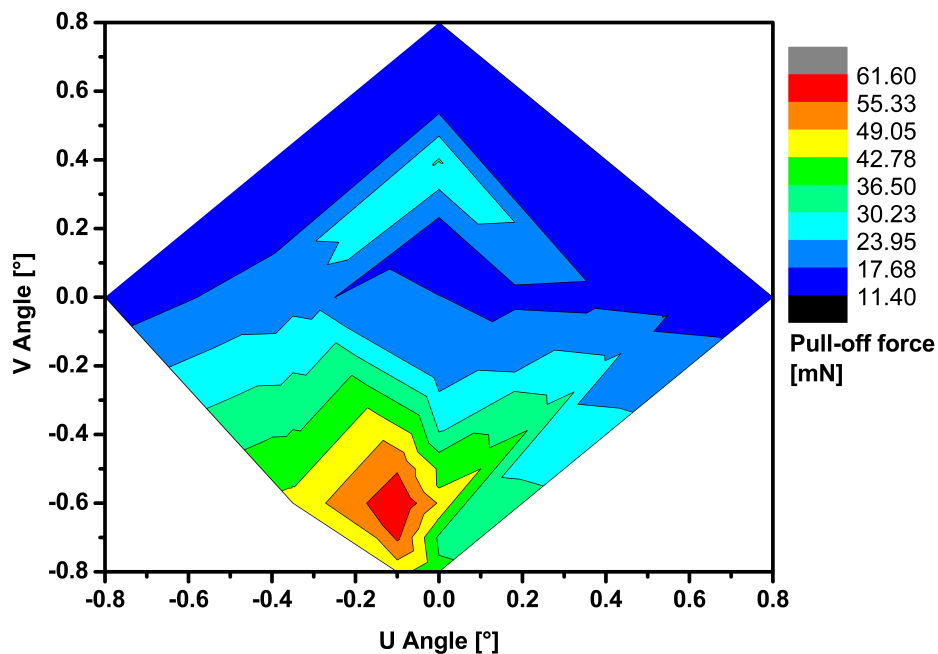


Figure 8.2: Map of measured pull-off forces as a function of systematic change in sample orientation along U and V axes at a constant preload stress. The *aligned* position is defined by $U = -0.1^\circ$ and $V = -0.6^\circ$.

Appendix III: Supplementary information to Chapter 6

SEM images of end-flaps

Figure 8.3 shows the tip-shapes of Type 1 adhesives (end-flaps) with various aspect ratios.

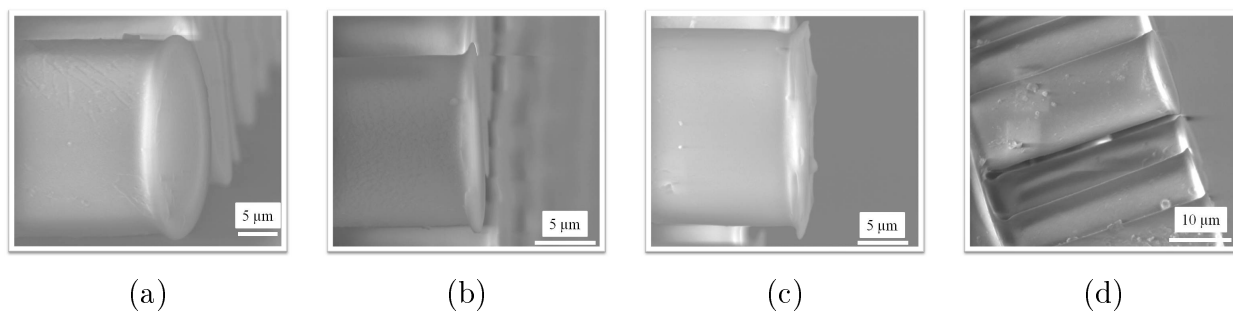


Figure 8.3: End-flaps at high magnification for different AR Type 1 adhesives.

Video results for adhesion loss

Adhesion loss for Type 1 and Type 2 adhesives occurred at high preload stress (e.g. preload stress > 0.45 MPa for AR 2). Figure 8.4 and Figure 8.5 show video snapshots for Type 1 and Type 2 AR 2 adhesives, respectively, for high preload stress (≈ 0.5 - 0.6 MPa).

For Type 1 adhesives during *unloading* from high preload stress, the end-flap unfolding occurred under lower compressive stress. A rapid wave that swept across the contact area over a much smaller period of around 3 s was indicative of the lack of time (and compressive stress) available to re-form contact (Snapshot 4, Figure 8.4 (a)).

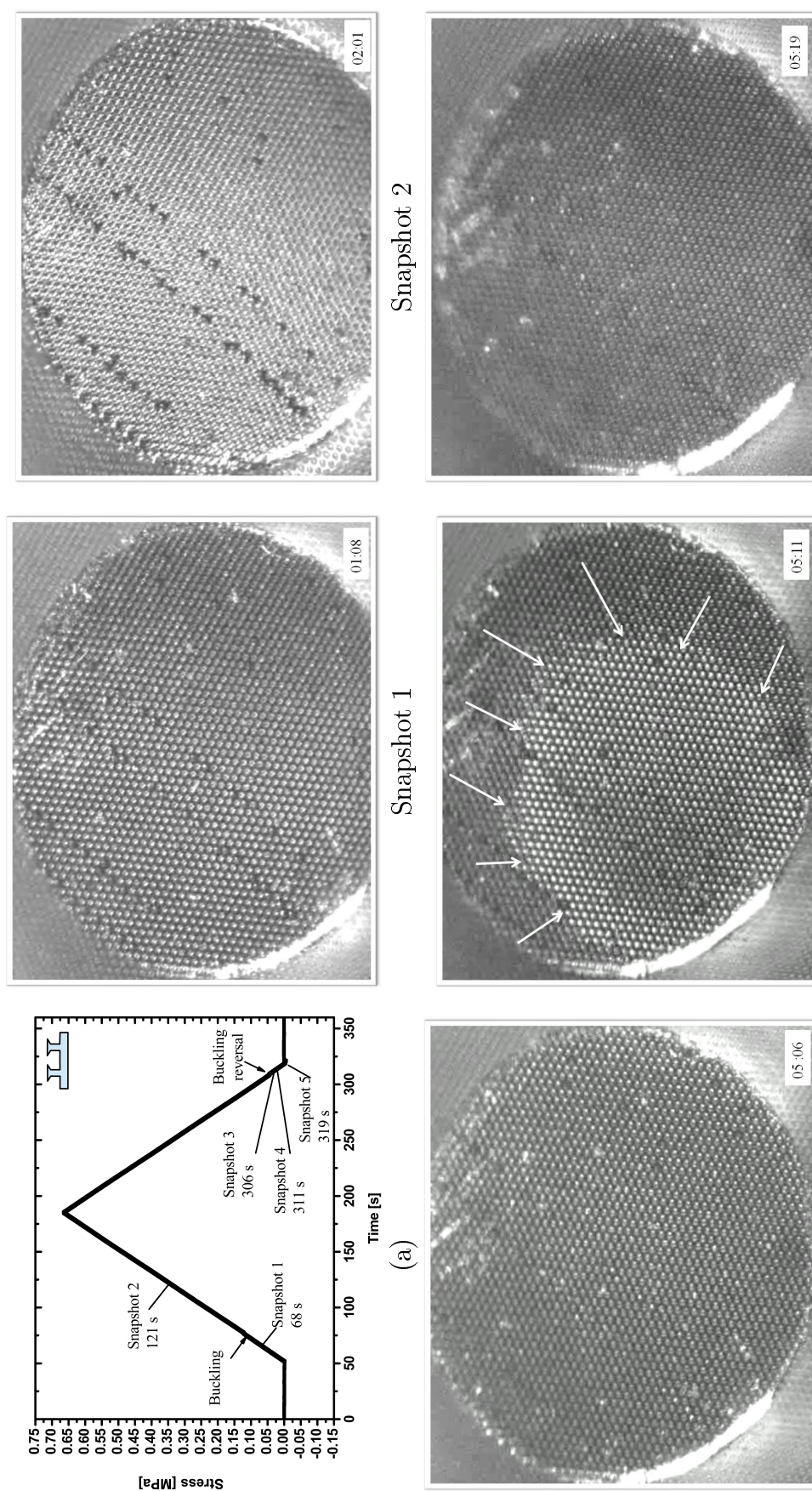


Figure 8.4: Adhesion loss for Type 1 AR 2 adhesive. (a) Stress-time plot with marked points corresponding to video snapshots at given times: Snapshot 1 -fibril tips in full contact. Snapshot 2 -fibrils in side contact after buckling. Snapshot 3 -fibril tips back in contact upon buckling reversal. Snapshot 4 -wave of bright spots. Snapshot 5 -detachment without pull-off. Black spots are defects on probe surface.

Type 2 adhesives showed a significant adhesion loss at all preloads above the preload stress that caused buckling (Figure 8.5). Video snapshots capture the various stages of fibril-probe contact interface prior to buckling (snapshot 1), immediately after buckling (snapshot 2), at maximum preload stress (snapshot 3) and prior to buckling reversal (snapshot 4). The detachment wave again travels rapidly across the sample (around 3-4 s) indicative of non-smooth sealing of the interface due to the round tips as circumferential cracks (snapshot 5).

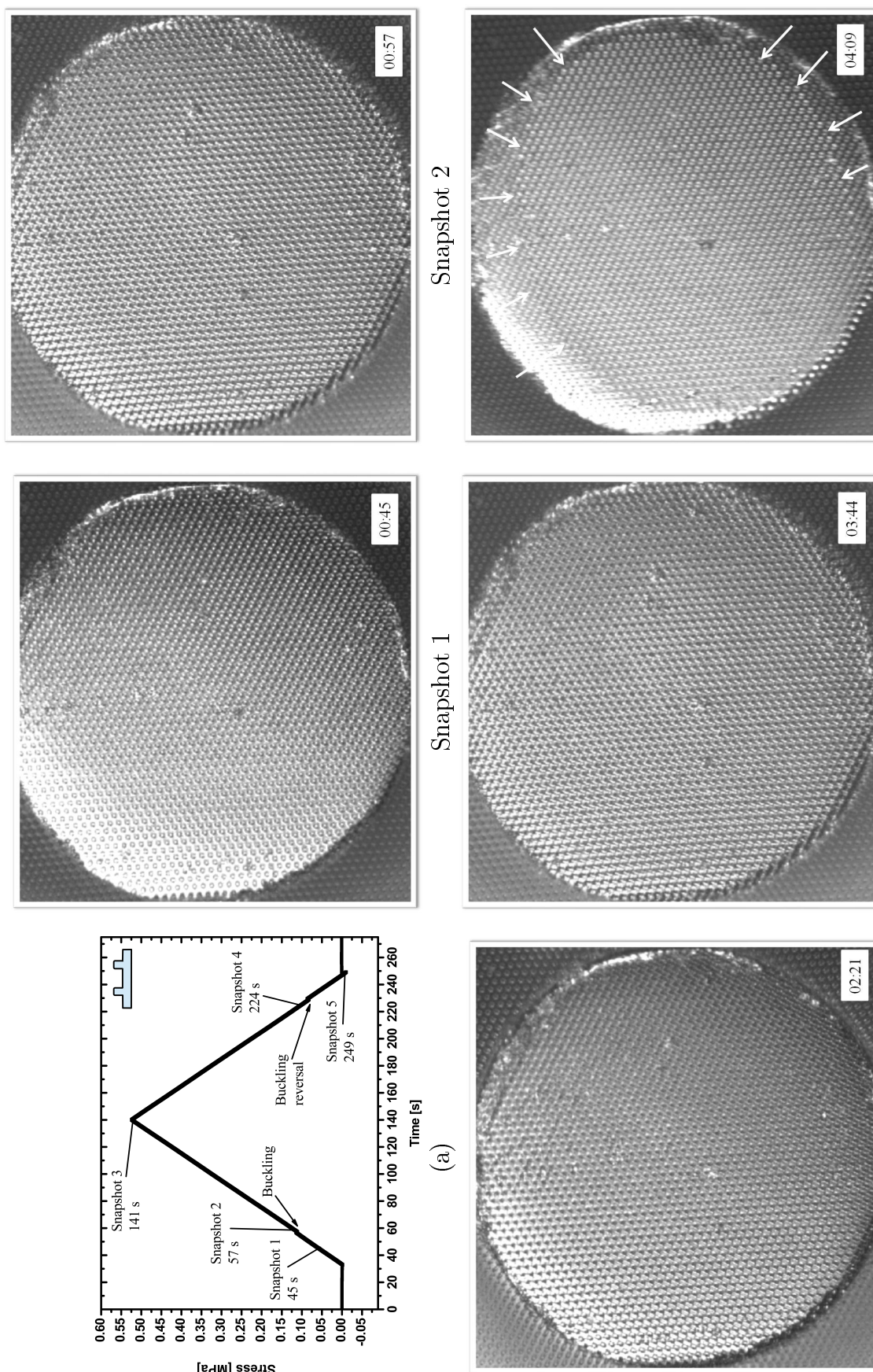


Figure 8.5: Adhesion loss for Type 2 AR 2 adhesive. (a) Stress-time plot with marked points corresponding to video snapshots at given times: Snapshot 1 -fibril tips in full contact. Snapshot 2 -fibrils in side contact just after buckling. Snapshot 3 -fibrils prone at preload stress maximum. Snapshot 4 -fibrils in side contact prior to buckling reversal. Snapshot 5 -partial detachment before low pull-off (arrows mark detachment front).

Fibril orientation change

Results in Figure 8.6 show influence of the change in the end-flap orientation on the pull-off strengths at a constant high preload stress. The exact sample orientation with respect to

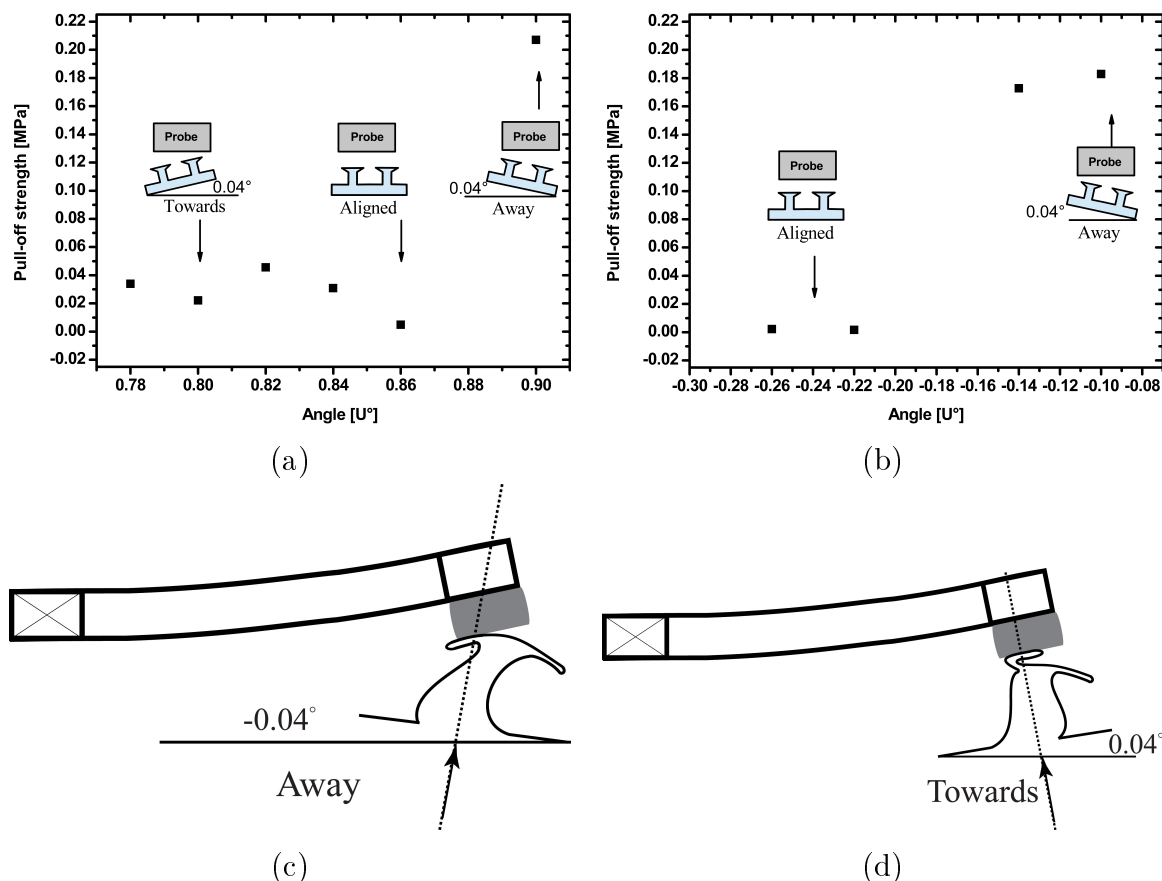


Figure 8.6: Dependence of stress for adhesion loss (σ_{loss}) on the sample alignment at a constant high preload stress. Sample orientations away from the probe with respect to the aligned state (see inset) result in high pull-off strengths even at high applied preload stress (>0.5 MPa). (a) and (b) pull-off strengths (at a constant high preload stress) as a function of sample alignment for two different locations on AR 2 sample. Schematic showing the probe-double-beam shape (exaggerated) at the maximum in compression for a very high preload stress for fibril orientation (c) away and (d) towards with respect to the probe. Arrow indicates the direction of fibril (sample) motion. Drawing not to the scale.

the probe that yields aligned state depended on the test location within a given sample. Hence repeatability of the response of sample alignment on adhesion at a high preload stress was tested for several adjacent locations. Plots in Figure 8.6(a) and (b) represent tests on adjacent locations. Similar changes in pull-off strengths were observed as a function of alignment change at a constant preload (≥ 0.5 MPa) in both cases. Whereas the *aligned*

state showed low pull-off strengths, a change in the sample's tilt *away* by 0.04° produced high pull-off strengths for the same high preload stress (Figure 8.6).

The unsymmetric nature adhesion response to the change in orientation of the sample "towards" and "away" from the probe-double-beam may be attributed to the fact that the double beam is not symmetrically clamped but is fixed at a single point. Double beam spring is clamped at one end and free to move only at the probe end, which possibly influences the end-flap fold-unfold as a function of its orientation see Figure 8.6 (c) and (d).

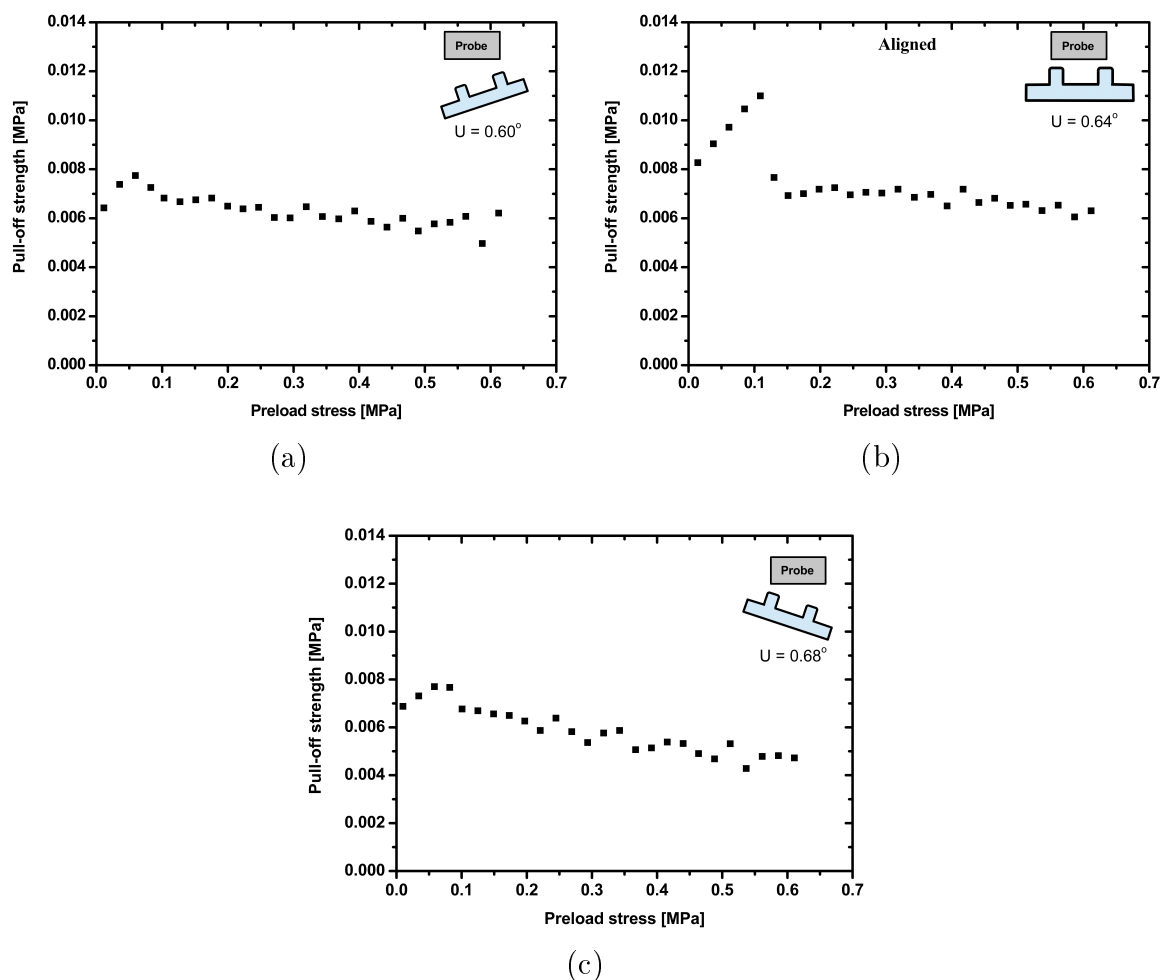


Figure 8.7: Negligible effect on the stress at adhesion loss with change in sample alignment for Type 2 adhesives. Fibril orientations (a) towards and (c) away from the probe with respect to the (b) aligned state.

The alignment change from the normal alignment, however, led to a loss in absolute adhesion strength of the samples as seen for Type 2 AR 2 sample (Figure 8.7). Type 2 adhesives with round tip-shapes failed to show orientation dependent change in the stress at which adhesion loss occurred, unlike the Type 1 adhesives. When different fibril orientations of the sample

with respect to the probe were tested by systematically changing sample alignment, the drop in adhesion appeared to always occur around the buckling stress (Figure 8.7).

Adhesion measurements on *Microtack*

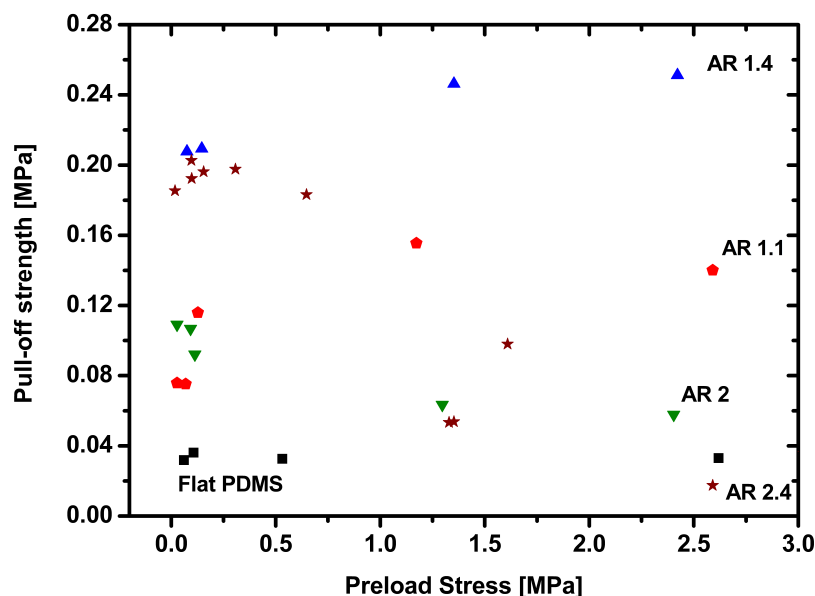


Figure 8.8: Type 1 adhesives having different ARs tested with the *Microtack* adhesion testing device

The adhesion tests on different AR samples were additionally repeated at the *Microtack* test device at the ESPCI ParisTech, Paris, to gain *in situ* visualization with an optical microscope. The force measurement in this case was done using a rigid extensometer (see Chapter 3, Section 3.2.1). Figure 8.8 shows the pull-off strengths of Type 1 adhesives as a function of preload stress. These results were comparable to those obtained by the *Macroscopic Adhesion testing Device* in house. Fibrils with higher AR showed loss in adhesion at a lower stress and their pull-off strengths were controlled mainly by their tip-shapes (and preloads) rather than compliance (or aspect ratio).

Appendix IV: Supplementary information to Chapter 7

Statistical nature of contact detachment was observed in terms of exceptionally high adhesion strengths shown by some single micropillars. Repeated tests on the same sample showed more than a two-fold increase in their adhesion tests for the same set of preload stresses and experimental conditions, e.g. for single micropillar with $d = 10 \mu\text{m}$ and $h = 20 \mu\text{m}$, Figure

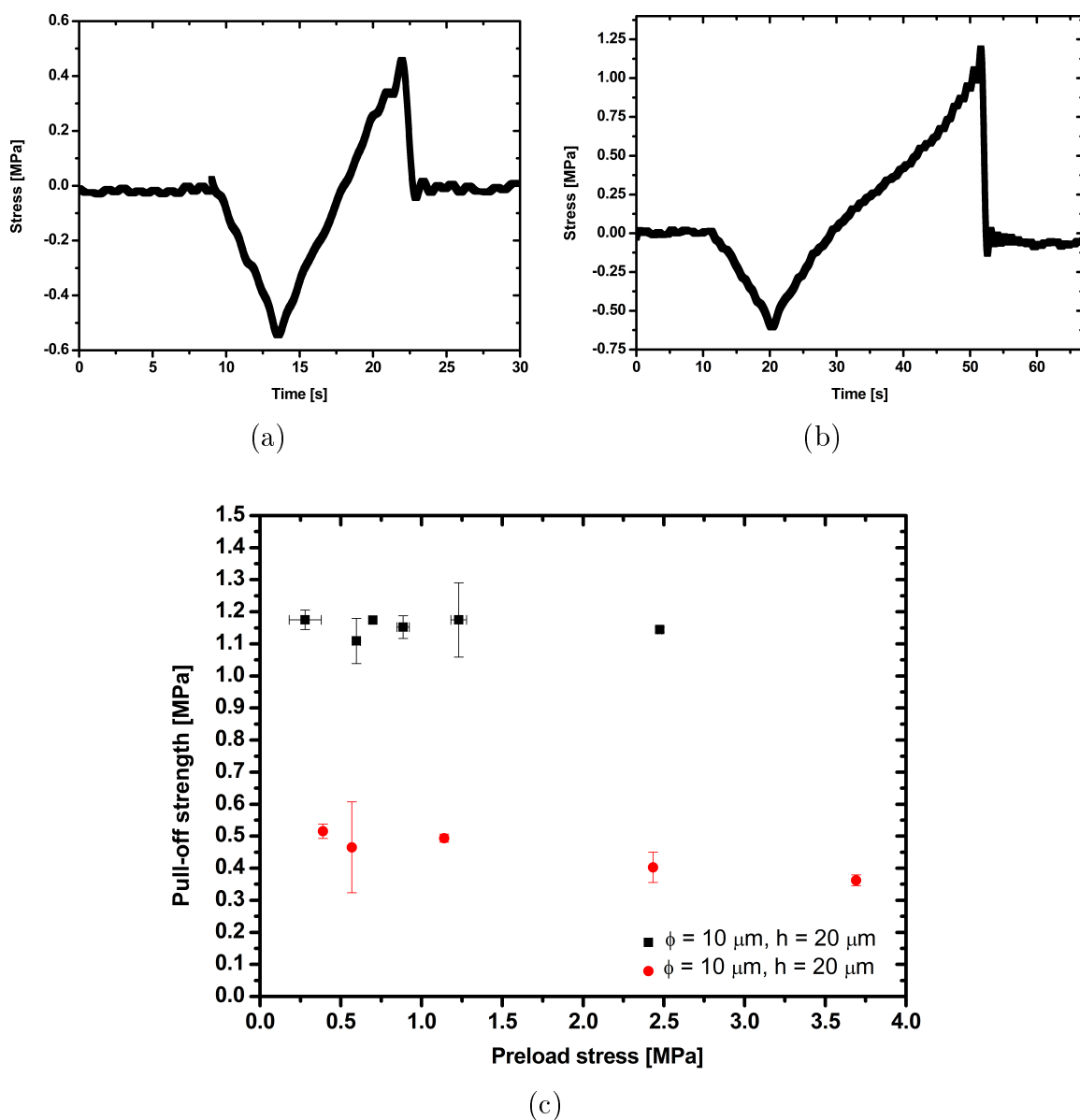


Figure 8.9: Stress vs. time curves for similar preload on single micropillar ($h = 20 \mu\text{m}$ and $d = 10 \mu\text{m}$) during different test runs, showing different pull-offs with (a) linear and (b) non-linear stress development during unloading. (c) Extraordinarily high pull-off strengths for the same single micropillar.

8.9. This is believed to originate from the stretching of the adhesive micropillar beyond Hookean elastic regime into the neo-Hookean regime (Figure 8.9 (b)) during the unloading to pull-off [Hui2003]. The exact shape of fibril contact is known the influence adhesion [delCampo2007]. Fabrication induced variations in the tip shapes may, therefore, explain the observed anomaly.